

LOW ENERGY NUCLEAR RECOIL RESPONSE IN XENON GAS FOR LOW  
MASS DARK MATTER WIMP SEARCH

A Dissertation

by

CLEMENT JAMES SOFKA

Submitted to the Office of Graduate and Professional Studies of  
Texas A&M University  
in partial fulfillment of the requirements for the degree of  
DOCTOR OF PHILOSOPHY

Chair of Committee,	Robert C. Webb
Committee Members,	Leslie A. Braby
	Bhaskar Dutta
	Teruki Kamon
Head of Department,	George R. Welch

May 2014

Major Subject: Physics

Copyright 2014 Clement James Sofka

## ABSTRACT

Over 80 years of astrophysical observations suggest that the observable luminous matter makes up  $\lesssim 5\%$  of the total energy density in the Universe. The remaining  $\sim 95\%$  comes from matter and energy that has not been observed directly. Discovering these “dark” sources of matter/energy is the single most important concern in the modern quest for understanding Nature. We live in an epoch that is almost certainly characterized by a flat, expanding Universe. Coupling this with the wealth of astrophysical surveys, we are able to probe the vastness of space, and develop theories of space-time evolution, going back in time several billions of years. The evidence suggests that the Universe began in a Big Bang, underwent a brief moment of Inflation, then cooled and began forming the structures (atoms, molecules, stars, galaxies, etc.) we observe plainly today. An integral part of this consistent story of the Universe’s birth and cosmic evolution is the existence of cold dark matter in the form of Weakly Interacting Massive Particles (WIMPs) and dark energy. Initial cosmological considerations suggested that WIMPs were some type of Standard Model (SM) particle, but even the best-case estimates lead to matter energy densities that come up well short without a significant modification of the underlying theory of gravity. The best proposed WIMP candidate has surfaced from efforts motivated by particle physics. A new type of WIMP arises out of Supersymmetry (SUSY). The Lightest Supersymmetric Particle (LSP), a neutralino, seems to fit perfectly into both particle physics and cosmology. First estimates from a Minimal Supersymmetric Standard Model (MSSM) placed the WIMP in the mass range of  $\mathcal{O}(10) - \mathcal{O}(10^3)$  GeV/ $c^2$ . However, there is mounting evidence in recent years that suggests the existence of a low mass WIMP as a suitable dark matter candidate. Some of the most sensitive detectors to



low mass WIMPs employ noble liquids as a target medium. Groups using noble liquid detectors are currently limited to the detection of relatively higher mass WIMPs because of detector threshold limits, background effects, or a lack of fundamental understanding of very low energy nuclear recoils ( $< 3$  keV<sub>nr</sub>). This work is aimed at studying these very low nuclear recoil energies in xenon to improve noble element detector sensitivities and develop a fundamental understanding of nuclear stopping power theories originally studied by Lindhard *et al.* in the 1960's. We present the nuclear recoil results from measurements using a nearly mono-energetic beam of neutrons aimed at high-pressure gaseous xenon (HPXe) in a time projection chamber (TPC). This work demonstrates the viability of future low mass dark matter WIMP and other rare event searches (*e.g.* Neutrinoless Double Beta Decay,  $0\nu\beta\beta$ ) using high pressure noble gases.

## DEDICATION

for James

## ACKNOWLEDGEMENTS

This work is more than just a demonstration of my “ability to perform independent research”, as stated in the Graduate Catalog of my beloved Texas A&M University. This work is the manifestation of years of love and support by so many folks around me, to whom I am truly grateful.

First and foremost, I would like to thank Dr. James White, to whom this work is dedicated. His level of integrity and brand of character are so rare on Earth that they are usually confined to the pages of a fiction novelist. His enthusiasm for science and outrageously gifted incite were unparalleled, and he was gracious enough to share those with me every day of our four-and-a-half years together. His terminal diagnosis came two days before we officially proposed the work recorded in this document. He was in and out of treatment in the coming months and, thus, was not present for all the fun, as he would have put it. He passed away exactly two months before this data was taken, but his guidance carried me through to its completion. In life, he gave me the exciting opportunity to face a blank canvas every day. In death, he gave me the courage to paint it with my own ideas. I am evermore grateful for his mentorship and our friendship.

Second, I would like to thank Dr. Robert “Bob” Webb and the rest of my advisory committee. Dr. Webb took the lead and stepped in to support me financially, in the absence of Dr. White, and Dr. Teruki Kamon graciously stepped in to fill the open position in my committee, so that I could continue my work. Without the constant advice and encouragement of my entire committee, I would have remained in no-mans-land with respect to completing my degree. I am very thankful for their faith and support.

Third, I would like to thank all of the people I have worked with at Texas A&M. Specifically, I want to thank my fellow Aggie lab mates Jianting Gao, Ty Stiegler, Rachel Mannino, Paul Terman and Zach Marquez. All of them contributed to my success in the lab, in the classroom or both. Sometimes, they simply helped to push me along, amidst my strong opinions and occasional bad attitude.

Fourth, I would like to thank my friends and colleagues with whom I worked on the NEXT project in Spain. Specifically, I want to thank Dr. Juan José “J.J.” Gómez-Cadenas, Dr. Igor Liubarsky, Sara Cárcel, Francesc Monrabal, Paola Ferrario and Justo Martín-Albo. They constantly reminded me that science is born of a unique human curiosity that is to be cherished and explored with excitement and passion. Their constant encouragement and faith in my abilities gave me the additional boost in confidence needed to proceed in my research efforts.

I would also like to thank my extended family and friends. They provided me with a lifetime of love and support that always strengthened my character and confidence. I truly appreciate their efforts to make me who I am today and I can only hope that they are proud of what I have accomplished so far and the trajectory of my future.

Finally, I would like to thank my loving wife Carrie and our four beautiful daughters Kylie, Brianna, Alaina and Mary. Those five incredible women hoist me up on their shoulders and carry me into Heaven every day. I know I am very heavy at times, but they never let me fall. They pull me through the rough patches, as well as the good times, and smile through it all. I am so lucky. Thank you.

# TABLE OF CONTENTS

	Page
ABSTRACT . . . . .	ii
DEDICATION . . . . .	iv
ACKNOWLEDGEMENTS . . . . .	v
TABLE OF CONTENTS . . . . .	vii
LIST OF FIGURES . . . . .	ix
LIST OF TABLES . . . . .	xxii
1. INTRODUCTION . . . . .	1
1.1 Astrophysical Evidence for Dark Matter . . . . .	1
1.1.1 Early cluster redshift measurements . . . . .	1
1.1.2 Spiral, elliptical and lenticular galaxy dynamics . . . . .	3
1.1.3 Dwarf galaxies . . . . .	8
1.2 Cosmological Evidence for Dark Matter . . . . .	11
1.2.1 Building a modern cosmology . . . . .	12
1.2.2 Modified gravity . . . . .	16
1.2.3 Gravitational lensing and cluster collisions . . . . .	18
1.2.4 Cosmic microwave background . . . . .	23
1.2.5 Big bang nucleosynthesis . . . . .	29
1.3 Dark Matter Candidates . . . . .	35
1.3.1 Baryonic dark matter . . . . .	35
1.3.2 Non-baryonic dark matter: Standard model . . . . .	37
1.3.3 Non-baryonic dark matter: Beyond the standard model . . . . .	39
1.4 Indirect Detection of WIMPs . . . . .	48
1.5 Direct Detection of WIMPs . . . . .	51
1.5.1 WIMP scattering kinematics . . . . .	52
1.5.2 Direct detection schemes . . . . .	54
1.5.3 Signal hints and the case for low mass WIMPs . . . . .	59
2. LOW ENERGY NUCLEAR RECOILS . . . . .	65
2.1 Setting the “True” Energy Scale . . . . .	65
2.2 Lindhard Theory . . . . .	69
2.2.1 The Lindhard factor . . . . .	71
2.2.2 Ionization yield in xenon . . . . .	73

3. EXPERIMENTAL SETUP . . . . .	76
3.1 Detector Construction . . . . .	76
3.1.1 Physical layout of the TPC . . . . .	77
3.1.2 Cleaning protocol . . . . .	78
3.1.3 Gas handling and purification . . . . .	80
3.1.4 Photosensors . . . . .	81
3.1.5 Electronics and signals . . . . .	83
3.2 Proton Beam at Texas A&M . . . . .	84
3.3 Proton Beam Energy Calibration . . . . .	86
3.4 Nuclear Recoil Scattering Setup . . . . .	90
4. SIMULATIONS . . . . .	92
4.1 Neutron Beam . . . . .	92
4.2 The Kinematic Edge . . . . .	96
4.3 Electroluminescent (EL) Gain . . . . .	100
4.4 Light Simulation . . . . .	106
4.4.1 Material optical properties . . . . .	106
4.4.2 S1 light collection efficiency . . . . .	107
4.4.3 S2 light collection efficiency . . . . .	107
5. RESULTS . . . . .	115
5.1 Event Selection . . . . .	115
5.1.1 S1 trigger . . . . .	115
5.1.2 S2 trigger . . . . .	116
5.2 Nuclear Recoil Measurements . . . . .	119
5.3 Error Propagation . . . . .	137
6. CONCLUSIONS . . . . .	139
6.1 Low Energy Nuclear Recoils in HPXe . . . . .	139
6.2 Electron Fraction . . . . .	139
6.3 Future Prospects for HPXe in Other Rare Event Searches . . . . .	142
BIBLIOGRAPHY . . . . .	144

# LIST OF FIGURES

FIGURE		Page
1.1	Rotational velocities in M31 as a function of distance from the galactic center. The <i>solid curve</i> is a 5 <sup>th</sup> order polynomial fit of the Rubin and Ford data for $R \leq 12'$ and a 4 <sup>th</sup> order polynomial fit for $R > 12'$ . The <i>dashed curve</i> illustrates a second rotation curve with a higher minimum near $R = 10'$ . Figure taken from [4]. . . . .	3
1.2	(a) shows the total integrated mass inside a given disk radius $r$ , as a function of $r$ for 11 spiral galaxies of varying morphology, showing approximate linear behavior. These are determined from rotational velocity data, extending out to the last measured velocity. The vertical scale corresponds to a disk model. Applying a spherical model implies a 40% increase in mass on this scale. The steeper slopes generally correspond to early type galaxies. Figure taken from [12]. (b) shows the rotational velocities ( <i>dots with error bars</i> ) in NGC 3198 as a function of distance from the galactic center. The two labeled curves show the individual contributions from the exponential disk and the dark matter halo. The upper curve is the sum of the two individual curves, with parameters $a$ and $\gamma$ adjusted in the halo density (see Eq. 1.4) for proper fit to the data points. Figure taken from [14]. . . . .	6
1.3	Map of satellite galaxies within the Milky Way's virial radius of $\sim 250$ kpc. These galaxies are loosely arranged in a plane nearly perpendicular to the galactic plane and is centered on the <i>dotted curve</i> with arbitrarily chosen $\pm 15^\circ$ band ( <i>solid curves</i> ). Figure from [19]. . . . .	9
1.4	Total mass integrated within 300 pc ( $M_{300}$ ) from each dSph center in units of solar masses ( $M_\odot$ ) vs total luminosity ( $L_\odot$ ). The brightest dSph galaxies were discovered prior to the SDSS and are shown in the right portion of the plot ( <i>blue squares</i> ) and the fainter dSph's found in the SDSS era are in the left portion ( <i>red circles</i> ). Error bars indicate the points where the likelihood function falls off to 60.6% of its peak value. Figure from [23]. . . . .	10
1.5	Summary plot showing the Hubble constant from several datasets as labelled. Figure from [32]. . . . .	17

1.6	Example schematic diagram of a source (galaxy, quasar, etc.) of photons being gravitationally lensed by an object in the image plane and the path followed to an observer on Earth. . . . .	19
1.7	Optical image of Abell 370 in the foreground acting as a strong lens for galaxies in the background field. Multiple images of systems are numbered. The <i>white contour</i> corresponds to the critical lines of the lens (at $z = 1.2$ ). The <i>red contour</i> outlines the region for multiple images of high redshift (here $z = 6$ ) object. Figure from [37]. . . . .	20
1.8	(a) shows the Bullet Cluster X-ray data from Chandra in <i>false color</i> . (b) shows the Bullet cluster, with X-ray data (baryonic hot plasma) offset from the dark matter content profiled by the <i>white contours</i> from strong+weak lensing data. (c) and (d) show the X-ray data from hot gases ( <i>pink</i> ) spatially offset from the dark matter ( <i>blue</i> ). . . . .	22
1.9	(a) shows a 2D slice from a 3D map of the local galaxy distribution out to $z = 0.15$ from SDSS-III. The Earth is at the center and each dot represents a galaxy color coded by the age of each galaxies star content ( <i>red</i> indicates older stars). The missing wedges are not included because the data there is obscured by dust from the Milky Way. (b) shows the low frequency (30 Hz) full sky map of the CMB from Planck. (c) is the less resolved CMB from WMAP. . . . .	25
1.10	Temperature angular power spectrum as a function of angular separation and multipole moment from Planck 2013 CMB data, where $\mathcal{D}_\ell = \ell(\ell + 1)C_\ell/2\pi$ . The <i>dark green curve</i> is a best-fit $\Lambda$ CDM model with errors bars and <i>light green shaded region</i> including error and cosmic variance. Figure from [51]. . . . .	28
1.11	Artistic representation of the evolution of the Universe with numbers derived from Planck 2013 CMB data. Figure from [52]. . . . .	28
1.12	Abundances of $^4\text{He}$ , D, $^3\text{He}$ , Li from Standard BBN predictions as a function of baryon-to-photon ratio, with 95% CL bands shown in color. The colored boxes are measured values. The two vertical bands show the baryon density from CMB ( <i>narrow</i> ) and the BBN concordance range ( <i>wide</i> ). Figure from [53]. . . . .	32



1.13	Cosmological constraints on $\Omega_\Lambda$ and $\Omega_m$ from Cosmic Microwave Background (CMB), Supernovae (SNe) and Baryon Acoustic Oscillation (BAO) data showing 68.3%, 95.4% and 99.7% confidence contours. The <i>grey</i> contours illustrate the combination from all three sources assuming a vacuum energy dominated equation of state ( $w = -1 \Rightarrow p = -\rho \Rightarrow \rho \propto \text{const.}$ ). The line labeled “Flat” indicates the trend for a flat Universe ( $k = 1$ ). Figure from [58]. . . . .	33
1.14	Matter energy content of the Universe using cosmological parameters from the most recent Planck results summarized in Table 1.1. . . . .	34
1.15	Summary of SM particles. Figure from [76]. . . . .	40
1.16	WIMP number density $Y_\chi \rightarrow Y$ per co-moving volume for WIMP mass $m_\chi = 100$ GeV and the resulting relic density, $\Omega_\chi$ , as a function of cosmological time, $t$ , and photon temperature, $T$ . The <i>solid grey contour</i> corresponds to the cross section (and freeze-out time) that leads to the “correct” relic density. The shaded regions indicate parameter space covered by cross sections that differ from the correct one by factors of 10 ( <i>yellow</i> ), $10^2$ ( <i>green</i> ) and $10^3$ ( <i>blue</i> ) from the correct one. The <i>dotted grey contour</i> shows the result of a WIMP that never freezes out and remains in thermal equilibrium. Figure from [79].	46
1.17	Summary of positron fraction measurements vs. electron-positron energy from the PAMELA, FermiLAT, and AMS latest results. Figure from [114]. . . . .	50
1.18	(a) shows the maximum nuclear recoil energy $E_{R,max}$ from a WIMP-nucleus elastic scatter as a function of target nucleus mass for WIMP masses of 100 ( <i>magenta</i> ), 50 ( <i>green</i> ), 25 ( <i>red</i> ) and 10 GeV/c <sup>2</sup> ( <i>blue</i> ). (b) shows $E_{R,max}$ for a 10 GeV/c <sup>2</sup> WIMP ( <i>solid curve</i> ) with the commonly used target nuclei labeled. . . . .	55
1.19	(a) shows differential event rates ( $dR/dE_R$ ) as a function of nuclear recoil energy ( $E_R$ ) for common target nuclei using input parameters from the recent LUX result [120] and a WIMP mass $M_\chi = 30$ . GeV/c <sup>2</sup> . (b) is a similar plot, but with $M_\chi = 100$ GeV/c <sup>2</sup> . . . . .	56
1.20	Approximate muon flux as a function of depth in underground labs used for low-background experiments. Figure from [121]. . . . .	57
1.21	Graphical summary of several named collaborations in the direct search for dark matter and detection scheme employed. The energies labeled indicate an approximate low energy threshold for the associated energy deposition channel. . . . .	58

1.22	Low energy signal in DAMA/NaI and DAMA/LIBRA showing annual modulation during several years of running. Figure from [124]. . . . .	59
1.23	Low energy spectrum from CoGeNT ( <i>left</i> ) with projected exponentially rising signal due to a 7 GeV/c <sup>2</sup> and 10 GeV/c <sup>2</sup> WIMP overlaid ( <i>left inset</i> ). Arrows above the peaks indicate possible cosmogenic peaks and peaks with no arrows are L-shell EC peaks of <sup>65</sup> Zn and <sup>68</sup> Ge. (See [126] for original plot and full details). CRESST-II data ( <i>right</i> ) from one detector module (Ch20) showing light yield vs. energy. The orange highlighted portion is the WIMP acceptance region, showing 6 events in this channel. The other colored bands indicate expected $\alpha$ backgrounds and the nuclear recoil regions of interest for the oxygen (O) and tungsten (W). (See [128] for original plot and full details). . . . .	61
1.24	Ionization yield vs. recoil energy for CDMS-II silicon detectors before ( <i>top</i> ) and after ( <i>bottom</i> ) phonon timing cuts. The bottom plot shows the 3 dark matter candidate events in lower left-hand portion of the acceptance region outlined by the <i>black curves</i> . (See [130] for original plot and full details). . . . .	62
1.25	Summary plot of the limits on SI elastic WIMP-nucleon cross-section $\sigma_{SI}$ as a function of $M_\chi$ . The areas above the curves have been ruled out by the corresponding experiments. The colored contours indicate the phase space favored by the labeled groups, with the ( <i>grey</i> ) and ( <i>light grey</i> ) representing phase space favored by Constrained MSSM. (See [132] for original plot and full details). . . . .	63
1.26	Summary plot of the SI elastic WIMP-nucleon cross-section $\sigma_{SI}$ as a function of $M_\chi$ with most recent LUX 90% C.L. ( <i>blue curve</i> ) $\pm 1\sigma$ . Also shown are limits from Edelweiss II ( <i>dark yellow curve</i> ), CDMS II ( <i>green curve</i> ), ZEPLIN-III ( <i>magenta curve</i> ) and XENON100 100 live-day ( <i>orange curve</i> ), and 225 live-day ( <i>red curve</i> ) results. The inset (same axis units) focuses on low WIMP masses and includes the regions favored by CoGeNT ( <i>light red contour</i> ), CDMS II 95% allowed region ( <i>green contour</i> ) with centroid ( <i>green X</i> ), CDMS II low threshold analysis ( <i>upper green curve</i> ), 90% allowed region from CRESST II ( <i>yellow contour</i> ) and DAMA/LIBRA allowed region ( <i>grey contour</i> ). (See [120] and references therein for original plot and full details regarding individual results and interpretations). . . . .	64
2.1	Illustration of a neutron or WIMP elastically scattering off a nucleus ( <i>left</i> ) and a gamma, beta or alpha interacting with the electrons ( <i>right</i> ). . . . .	69

2.2	Block diagram representation of the energy dissipation channels in xenon and the resulting measurable signals in the form of heat, primary scintillation and ionization. . . . .	72
3.1	Photographs showing the TPC internal components. The <i>upper left</i> shows the EL grids with both (gate and anode) 88% open area meshes in place. The <i>lower left</i> shows a view looking into the drift region toward the cathode with the cathode, field rings, PMTs and reflective PTFE holders in place. The <i>right</i> photo shows a view of the fully assembled internals with all resistor chain and internal electronics and wiring in place. . . . .	78
3.2	Cross-sectional schematic of the TPC and pressure vessel used in this work. . . . .	79
3.3	Picture of the complete experimental setup with the TPC surrounded by lead for background characterization. The electronics and DAQ are out of view to the left. . . . .	80
3.4	R7378A PMT base schematic for grounded photocathode operation with +HV on the PMT anode. . . . .	82
3.5	Block diagram of the electronics and signal chain. Channels 1-5 are $\times 10$ amplified analog signals from the cathode and side PMTs. Channel 6 is a $\times 10$ amplified analog signal from the anode PMT and Channel 7 is the un-amplified analog anode PMT signal. The discriminator's threshold was set to trigger on single photoelectrons. Any channel above threshold produced a 150 ns square wave and was sent to the summing circuit. The summed square waves were sent to the DAQ's external trigger input for S1 coincidence triggers. S2 triggers came from the Channel 6 raw $\times 10$ signal. . . . .	83
3.6	Block diagram of the Pelletron accelerator and major beam line components at the Texas A&M Nuclear Science Center. . . . .	85
3.7	(a) and (b) show the Pelletron accelerator tank (opened for maintenance) and the internal structures respectively. The entire charging system was re-built prior to the actual nuclear recoil measurements. .	86
3.8	( a) shows proton beam spot hitting the quartz window with no LiF target in place. ( b) shows the LiF coated Ta metal strip mounted on the beam window inside the evacuated beam pipe. . . . .	87

3.9	Scattering setup showing the beam pipe, quartz window, LiF target, pressure vessel and active volume of HPXe. A removable 1"×2"×3" lead block (not shown) was placed between the beam window and pressure vessel and used to characterize the gamma background from the LiF target. The lead was oriented such that it was centered on the beam window with the 1" thickness in the path of the beam. . . .	91
4.1	Neutron energies as a function of lab emission angle. . . . .	94
4.2	Proton energy loss in the 75 nm thick LiF target (keV) as a function of incident proton energy (MeV). The plot ranges from the threshold energy of 1.882 MeV ( <i>red dot</i> ) for the ${}^7\text{Li}(p,n){}^7\text{Be}$ reaction to the highest proton energy used in the final data set (2.734 MeV). All proton stopping powers were taken from the NIST Pstar database [156].	95
4.3	(a) shows the neutron energy band (keV) ( <i>red shaded</i> ) as a function of emission angle (degrees) in the lab frame for the thin LiF target corresponding to a maximum incident proton kinetic energy of 2.734 MeV. (b) shows the same spectrum, but only including the energies falling inside the geometric acceptance cone of the active xenon in the TPC during the neutron data runs. . . . .	96
4.4	(a) and (b) show the scattering setup and detector construction used in the <i>Geant4</i> simulation. Only the quartz beam pipe window ( <i>blue</i> ), the SS chamber, flanges and end caps ( <i>light blue</i> ), PMTs ( <i>yellow</i> ) and active xenon volume ( <i>red</i> ) are shown for clarity. All the internal HDPE and PTFE was modeled, but not shown here. (c) and (d) show example neutron tracks ( <i>green</i> ) as the neutrons scatter off the detector components. . . . .	98
4.5	(a) shows all neutron energies ( <i>blue</i> ) entering the active xenon volume in the MC study for the highest energy in this work $E_p = 2.734$ MeV. The ( <i>red</i> ) portion is shown for illustration and corresponds to the neutrons contributing to the $E_{nr} > 28$ keVnr. (b) shows the xenon recoil spectrum in the TPC at 6 bar pressure for the same neutron energies in (4.5a). (c) shows the neutron energy distribution simulated at the LiF target. (d) shows the energy spread of the neutrons at the LiF target that cause recoils $E_r > 28$ keVnr. . . . .	99

4.6	Cross-section of the center of the TPC ( <i>left</i> ) with the cathode, gate and anode planes shown with voltages labeled, as well as the PMT faces nearest the cathode and anode. The <i>middle</i> figure shows the 3d image of the unit cell of the crossed-wire mesh used to calculate the E-fields in <i>COMSOL</i> . The <i>right</i> figure shows where the majority of field lines ( <i>red</i> ) originating in the drift region end up on the anode. .	102
4.7	Reduced electric fields in the TPC as a function of z-position along the axis of the drift field. The vertical scale corresponds to $(E/p - 0.83)$ so that any value above zero produces EL light. The enhancement just to the right of the anode is due to the difference in relative permittivities of the xenon and quartz PMT face. . . . .	103
4.8	2d geometry used in the <i>Garfield</i> simulation. . . . .	104
4.9	(a) and (b) show the electric fields $ \vec{E} $ as a function of z-position from the 3d “real” geometry from <i>COMSOL</i> and the 2d scaled model from <i>Garfield</i> respectively. The vertical axis on both plots is in kV/cm. The horizontal axes are in local model coordinates in units of cm. . .	109
4.10	Typical electron paths from the drift region (below the plotted area) into the EL gap. The gate wire grid plane is located at $y=1.27$ cm and the anode plane is at $y=1.57$ cm. . . . .	110
4.11	(a) shows the hit pattern of the electrons on the anode ( $y = 1.57$ cm) or PMT face ( $y = 1.67$ cm). (b) shows the EL gain per electron from the <i>Garfield</i> simulation. . . . .	110
4.12	Composite showing the EL gain as a function of $y$ -position near an anode wire ( <i>top left</i> ) and a similar plot, zoomed out to include the anode and PMT face ( <i>bottom</i> ). The remaining plot ( <i>top right</i> ) shows the total histogram of the EL gains, with the corresponding gains highlighted. . . . .	111
4.13	Plots showing the S1 LCE as a function of simulated z position ( <i>upper left</i> ), x (or y) position ( <i>lower left</i> ), radius from the center in the x-y plane ( <i>upper right</i> ) and the total LCE histogram. . . . .	112
4.14	Plots showing the S2 LCE as a function of simulated x (or y) position ( <i>upper left</i> ), fraction of the total light captured by the anode PMT ( <i>lower left</i> ), simulated radius from the center in the x-y plane ( <i>upper right</i> ) and the total LCE histogram. The <i>blue curve</i> in the <i>lower left</i> plot is a Gaussian fit of the S2 LCE with mean $\bar{\epsilon}_{S2} = 0.104$ and no selection cuts applied. . . . .	113

- 4.15 Plots showing the S2 LCE as a function of reconstructed x (or y) position (*upper left*), reconstructed x-y position (*lower left*), reconstructed radius from the center in the x-y plane (*upper right*). The *red* points show all events for all simulated positions. The *blue* points show the reconstructed points after selecting only events with a high fraction of light ( $a_{\text{anodePMT}}/a_{\text{total}} > 0.55$ ) in the anode PMT. The *blue curve* in the *lower right* plot is a Gaussian fit of the total S2 LCE with mean  $\bar{\epsilon}_{S2} = 0.104$  after the anode PMT fractional light cut. . . . . 114
- 5.1 Typical PMT signal waveforms for a 29.7 keV x-ray (a) and a  $\sim 28$  keVnr nuclear recoil (b) from the S1-triggered data. The S1 is barely or not at all visible on these full scale images. A total of 7 channels are shown. The bottom channel is the un-amplified ( $\times 1$ ) anode PMT signal. The six channels above it are the amplified ( $\times 10$ ) signals from the cathode PMT (*second from bottom*), the side PMTs and the ( $\times 10$ ) anode PMT (*top*). . . . . 117
- 5.2 Typical PMT signal waveforms for a 29.7 keV x-ray (a) and a  $\sim 1.2$  keVnr nuclear recoil (b) from the S2-triggered data. The S1 is barely or not at all visible on the full scale image in (a). The S1 of 4 photoelectrons is seen on the  $\times 10$  image in (b) along with an S2 of 233 photoelectrons. A total of 7 channels are shown. The bottom channel is the un-amplified ( $\times 1$ ) anode PMT signal. The six channels above it are the amplified ( $\times 10$ ) signals from the cathode PMT (*second from bottom*), the side PMTs and the ( $\times 10$ ) anode PMT (*top*). . . . . 118
- 5.3 Summary plots for 31.55 keVnr. The *top left* plot shows the energy spectrum of the neutrons that enter the active xenon volume according to the MC simulation, with a Gaussian fit (*red curve*). The *top right* is the single scatter, un-smeared nuclear recoil energy (keVnr) from the MC simulation. The *middle left* plot is the energy spectrum of the data from the S1 light only, where the conversion of 2.29 pes/keV was used. The *middle right* is the raw S2 energy spectrum of the data in electron equivalent energy (keVee) after all software cuts. The *lower left* is the low energy region of the S2 pe spectrum (*red* is data, *blue* is the scaled, smeared MC) with the average background from the data indicated by the *black line* and the  $3\sigma$  level above the background indicated by the *green line*. The *lower right* shows the number of counted electrons (*red* is data, *blue* is the scaled, smeared MC). . . . 123

- 5.4 Summary plots for 27.93 keVnr. The *top left* plot shows the energy spectrum of the neutrons that enter the active xenon volume according to the MC simulation, with a Gaussian fit (*red curve*). The *top right* is the single scatter, un-smeared nuclear recoil energy (keVnr) from the MC simulation. The *middle left* plot is the energy spectrum of the data from the S1 light only, where the conversion of 2.29 pes/keV was used. The *middle right* is the raw S2 energy spectrum of the data in electron equivalent energy (keVee) after all software cuts. The *lower left* is the low energy region of the S2 pe spectrum (*red* is data, *blue* is the scaled, smeared MC) with the average background from the data indicated by the *black line* and the  $3\sigma$  level above the background indicated by the *green line*. The *lower right* shows the number of counted electrons (*red* is data, *blue* is the scaled, smeared MC). . . . 124
- 5.5 Summary plots for 25.93 keVnr. The *top left* plot shows the energy spectrum of the neutrons that enter the active xenon volume according to the MC simulation, with a Gaussian fit (*red curve*). The *top right* is the single scatter, un-smeared nuclear recoil energy (keVnr) from the MC simulation. The *middle left* plot is the energy spectrum of the data from the S1 light only, where the conversion of 2.29 pes/keV was used. The *middle right* is the raw S2 energy spectrum of the data in electron equivalent energy (keVee) after all software cuts. The *lower left* is the low energy region of the S2 pe spectrum (*red* is data, *blue* is the scaled, smeared MC) with the average background from the data indicated by the *black line* and the  $3\sigma$  level above the background indicated by the *green line*. The *lower right* shows the number of counted electrons (*red* is data, *blue* is the scaled, smeared MC). . . . 125
- 5.6 Summary plots for 21.93 keVnr. The *top left* plot shows the energy spectrum of the neutrons that enter the active xenon volume according to the MC simulation, with a Gaussian fit (*red curve*). The *top right* is the single scatter, un-smeared nuclear recoil energy (keVnr) from the MC simulation. The *middle left* plot is the energy spectrum of the data from the S1 light only, where the conversion of 2.29 pes/keV was used. The *middle right* is the raw S2 energy spectrum of the data in electron equivalent energy (keVee) after all software cuts. The *lower left* is the low energy region of the S2 pe spectrum (*red* is data, *blue* is the scaled, smeared MC) with the average background from the data indicated by the *black line* and the  $3\sigma$  level above the background indicated by the *green line*. The *lower right* shows the number of counted electrons (*red* is data, *blue* is the scaled, smeared MC). . . . 126

- 5.7 Summary plots for 15.94 keVnr. The *top left* plot shows the energy spectrum of the neutrons that enter the active xenon volume according to the MC simulation, with a Gaussian fit (*red curve*). The *top right* is the single scatter, un-smeared nuclear recoil energy (keVnr) from the MC simulation. The *middle left* plot is the energy spectrum of the data from the S1 light only, where the conversion of 2.29 pes/keV was used. The *middle right* is the raw S2 energy spectrum of the data in electron equivalent energy (keVee) after all software cuts. The *lower left* is the low energy region of the S2 pe spectrum (*red* is data, *blue* is the scaled, smeared MC) with the average background from the data indicated by the *black line* and the  $3\sigma$  level above the background indicated by the *green line*. The *lower right* shows the number of counted electrons (*red* is data, *blue* is the scaled, smeared MC). . . . 127
- 5.8 Summary plots for 14.68 keVnr. The *top left* plot shows the energy spectrum of the neutrons that enter the active xenon volume according to the MC simulation, with a Gaussian fit (*red curve*). The *top right* is the single scatter, un-smeared nuclear recoil energy (keVnr) from the MC simulation. The *middle left* plot is the energy spectrum of the data from the S1 light only, where the conversion of 2.29 pes/keV was used. The *middle right* is the raw S2 energy spectrum of the data in electron equivalent energy (keVee) after all software cuts. The *lower left* is the low energy region of the S2 pe spectrum (*red* is data, *blue* is the scaled, smeared MC) with the average background from the data indicated by the *black line* and the  $3\sigma$  level above the background indicated by the *green line*. The *lower right* shows the number of counted electrons (*red* is data, *blue* is the scaled, smeared MC). . . . 128
- 5.9 Summary plots for 11.91 keVnr. The *top left* plot shows the energy spectrum of the neutrons that enter the active xenon volume according to the MC simulation, with a Gaussian fit (*red curve*). The *top right* is the single scatter, un-smeared nuclear recoil energy (keVnr) from the MC simulation. The *middle left* plot is the energy spectrum of the data from the S1 light only, where the conversion of 2.29 pes/keV was used. The *middle right* is the raw S2 energy spectrum of the data in electron equivalent energy (keVee) after all software cuts. The *lower left* is the low energy region of the S2 pe spectrum (*red* is data, *blue* is the scaled, smeared MC) with the average background from the data indicated by the *black line* and the  $3\sigma$  level above the background indicated by the *green line*. The *lower right* shows the number of counted electrons (*red* is data, *blue* is the scaled, smeared MC). . . . 129



- 5.10 Summary plots for 7.44 keVnr. The *top left* plot shows the energy spectrum of the neutrons that enter the active xenon volume according to the MC simulation, with a Gaussian fit (*red curve*). The *top right* is the single scatter, un-smeared nuclear recoil energy (keVnr) from the MC simulation. The *middle left* plot is the energy spectrum of the data from the S1 light only, where the conversion of 2.29 pes/keV was used. The *middle right* is the raw S2 energy spectrum of the data in electron equivalent energy (keVee) after all software cuts. The *lower left* is the low energy region of the S2 pe spectrum (*red* is data, *blue* is the scaled, smeared MC) with the average background from the data indicated by the *black line* and the  $3\sigma$  level above the background indicated by the *green line*. The *lower right* shows the number of counted electrons (*red* is data, *blue* is the scaled, smeared MC). . . . 130
- 5.11 Summary plots for 4.29 keVnr. The *top left* plot shows the energy spectrum of the neutrons that enter the active xenon volume according to the MC simulation, with a Gaussian fit (*red curve*). The *top right* is the single scatter, un-smeared nuclear recoil energy (keVnr) from the MC simulation. The *middle left* plot is the energy spectrum of the data from the S1 light only, where the conversion of 2.29 pes/keV was used. The *middle right* is the raw S2 energy spectrum of the data in electron equivalent energy (keVee) after all software cuts. The *lower left* is the low energy region of the S2 pe spectrum (*red* is data, *blue* is the scaled, smeared MC) with the average background from the data indicated by the *black line* and the  $3\sigma$  level above the background indicated by the *green line*. The *lower right* shows the number of counted electrons (*red* is data, *blue* is the scaled, smeared MC). . . . 131
- 5.12 Summary plots for 2.76 keVnr. The *top left* plot shows the energy spectrum of the neutrons that enter the active xenon volume according to the MC simulation, with a Gaussian fit (*red curve*). The *top right* is the single scatter, un-smeared nuclear recoil energy (keVnr) from the MC simulation. The *middle left* plot is the energy spectrum of the data from the S1 light only, where the conversion of 2.29 pes/keV was used. The *middle right* is the raw S2 energy spectrum of the data in electron equivalent energy (keVee) after all software cuts. The *lower left* is the low energy region of the S2 pe spectrum (*red* is data, *blue* is the scaled, smeared MC) with the average background from the data indicated by the *black line* and the  $3\sigma$  level above the background indicated by the *green line*. The *lower right* shows the number of counted electrons (*red* is data, *blue* is the scaled, smeared MC). . . . 132

- 5.13 Summary plots for 2.75 keVnr. The *top left* plot shows the energy spectrum of the neutrons that enter the active xenon volume according to the MC simulation, with a Gaussian fit (*red curve*). The *top right* is the single scatter, un-smeared nuclear recoil energy (keVnr) from the MC simulation. The *middle left* plot is the energy spectrum of the data from the S1 light only, where the conversion of 2.29 pes/keV was used. The *middle right* is the raw S2 energy spectrum of the data in electron equivalent energy (keVee) after all software cuts. The *lower left* is the low energy region of the S2 pe spectrum (*red* is data, *blue* is the scaled, smeared MC) with the average background from the data indicated by the *black line* and the  $3\sigma$  level above the background indicated by the *green line*. The *lower right* shows the number of counted electrons (*red* is data, *blue* is the scaled, smeared MC). . . . 133
- 5.14 Summary plots for 1.56 keVnr. The *top left* plot shows the energy spectrum of the neutrons that enter the active xenon volume according to the MC simulation, with a Gaussian fit (*red curve*). The *top right* is the single scatter, un-smeared nuclear recoil energy (keVnr) from the MC simulation. The *middle left* plot is the energy spectrum of the data from the S1 light only, where the conversion of 2.29 pes/keV was used. The *middle right* is the raw S2 energy spectrum of the data in electron equivalent energy (keVee) after all software cuts. The *lower left* is the low energy region of the S2 pe spectrum (*red* is data, *blue* is the scaled, smeared MC) with the average background from the data indicated by the *black line* and the  $3\sigma$  level above the background indicated by the *green line*. The *lower right* shows the number of counted electrons (*red* is data, *blue* is the scaled, smeared MC). . . . 134
- 5.15 Results from all nuclear recoil data runs plotted as a function of  $E_r$  at a drift field of  $E_{drift} = 400$  V/cm. Error bars correspond to  $\pm 1\sigma$ . The statistical error in  $E_r$  is smaller than the width of the dots. The *top left* shows the total number of electrons, the *top right* shows the specific charge yield, the *bottom left* shows the electron equivalent energy and the *bottom right* shows the nuclear ionization quenching factor. The *green curve* indicates the expected electron equivalent energy (total energy given to electrons,  $\eta$ ) using the Lindhard nuclear quenching. The *blue curve* indicates the total nuclear quenching ( $f_n = kg/[1+kg]$ ) from Lindhard. . . . 135

5.16	Results from the only S2-triggered nuclear recoil data runs plotted as a function of $E_r$ at a drift field of $E_{drift} = 400$ V/cm. Error bars correspond to $\pm 1\sigma$ . The statistical error in $E_r$ is smaller than the width of the dots. The <i>top left</i> shows the total number of electrons, the <i>top right</i> shows the specific charge yield, the <i>bottom left</i> shows the electron equivalent energy and the <i>bottom right</i> shows the nuclear ionization quenching factor. The <i>green curve</i> indicates the expected electron equivalent energy (total energy given to electrons, $\eta$ ) using the Lindhard nuclear quenching. The <i>blue curve</i> indicates the total nuclear quenching ( $f_n = kg/[1 + kg]$ ) from Lindhard. . . . .	136
6.1	Integrated event rates for spin-independent WIMP-nucleus elastic scattering in xenon for a common set of cosmological parameters. The bottom horizontal scale is the nuclear recoil energy (keVnr) and the partial scale shown on top is the $\sim$ linear electron response region measured in this work. . . . .	140

## LIST OF TABLES

TABLE		Page
1.1	Summary of dark matter cosmological parameters. The table is reproduced from [32], where the most recent results from Planck were combined with the other astrophysical data listed in parallel. . . . .	35
3.1	Summary of the TPC electrodes and the resulting optical transparency to normally incident light. . . . .	79
4.1	Summary of parameters used in the 2d <i>Garfield</i> model. See Fig. 4.8 for corresponding geometry. . . . .	104
5.1	Summary of results for all nuclear recoil data runs. The $1\sigma$ statistical error is given for all derived quantities. The statistical error in the recoil energies ranges from 0.03 to 0.08 keVnr. . . . .	122

## 1. INTRODUCTION

We are on an exciting journey through space and time; collectively and relentlessly pioneering together on the wavefront of reality. As we stream forward in time, we look around in wonder, intoxicated by the Universe we see and feel. Some of the Universe’s beauty is clearly visible to us, either with our eyes from our backyards or with a giant telescope on a desert hilltop. Sometimes the Universe collides with one of our cleverly engineered sensors deep underground or orbiting in space and we are left tracing its signature like cosmic forensic investigators. We piece together these clues in our clumsy effort to complete the cosmic puzzle and finally uncover the true identity of what or who the Universe really is. At best, our work results in a simple carnival caricature of reality. Just as we think we have gathered enough evidence to truly identify Nature, a peculiar puzzle piece amasses and opens the door to everything and nothing at the same time. We look harder, like good investigators, and find that these new clues can be neither seen nor touched nor sensed by us directly in any way. But like every other effect without an apparent cause, we embark on another quest of discovery until the cosmic wavefront breaks on the beach of forever. This is the story of Nature’s “dark” secrets. This is the story of Dark Matter and Dark Energy. Not everyone is involved in the quest, but all are along for the journey.

### 1.1 Astrophysical Evidence for Dark Matter

#### *1.1.1 Early cluster redshift measurements*

In 1933, Fritz Zwicky published a study of nine extragalactic nebular clusters, confirming the relationship, previously shown by Hubble [1], between an object’s recessional velocity (*i.e.* redshift,  $z$ ) and its distance from Earth at the megaparsec scale [2]. In addition, Zwicky was perhaps most excited about the new ability to

resolve individual objects within the “fuzzy” clusters and measure their apparent velocities with the new 100-inch telescope that sat atop Mount Wilson in Southern California. The data revealed a large dispersion of velocities ( $\sigma_v \sim 1000$  km/s) in the Coma cluster, which did not match calculations. For example, if all the matter content in the Coma cluster is assumed to be entirely comprised of luminous matter, having  $N$  components in a mechanically bound, stationary state, then, according to the Virial Theorem, the time average kinetic energy,  $\overline{E}_k$ , of the system is equal in magnitude to one half of the total potential energy,  $\overline{E}_p$ , where each member of the system has mass  $M_i$  and velocity  $v_i$ :

$$\overline{E}_k = -\frac{1}{2}\overline{E}_p = \sum_{i=1}^N M_i \overline{v_i^2} \quad (1.1)$$

However, using the best estimates for the mass at the time, these assumptions yielded a velocity dispersion that was off by a factor of  $\sim 13$ . One can attempt to justify this by assuming that the system’s kinetic and potential energy are equal or that the cluster itself is not bound together, but the calculation only improves by a factor of  $\sqrt{2}$  or still requires a total mass  $\sim 10\times$  the visible mass. At the time there was no solid explanation for the velocity dispersions that was also consistent with the redshift data and a flat, expanding universe. As a result, Zwicky emphasized the urgent need for science to explain the inconsistency. He went further to suggest the possibility that it could be resolved within the current theoretical framework (via Newton and Einstein) by allowing for a large fraction of the mass to be in the form of some unseen matter that neither emits nor absorbs light, or “dark (cold) matter”, as he put it. This was not the first time that dark matter was being blamed for mysterious phenomena [3], but it signaled the start of the race to uncover the nature of dark matter on a large astronomical scale, and, as technology improved,

perhaps look for signs of it elsewhere.

### 1.1.2 *Spiral, elliptical and lenticular galaxy dynamics*

For decades, the scientific community was fairly quiet on the subject of dark matter. Only a handful of publications mentioned large, optically invisible masses, unexpected velocity dispersions or rising rotation curves, however, data eventually accumulated. Some of it came from within the Milky Way galaxy, but the catalyst for renewed focus on dark matter came, in 1970, from the spiral galaxy Andromeda (M31), the largest member of our own cluster. Rubin and Ford [4] measured the rotational velocity of M31 out to a radius of  $\sim 24$  kpc from its center. The measurements were made using HII emissions for  $R > 3$  kpc, and a narrow NII line for  $R < 3$  kpc.

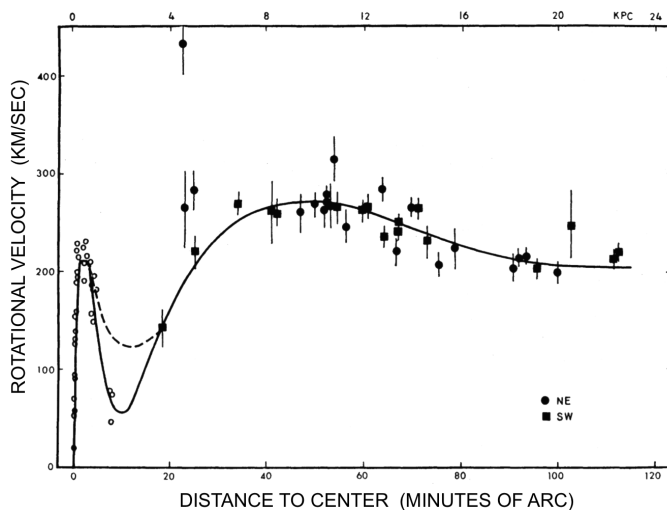


Figure 1.1: Rotational velocities in M31 as a function of distance from the galactic center. The *solid curve* is a  $5^{th}$  order polynomial fit of the Rubin and Ford data for  $R \leq 12'$  and a  $4^{th}$  order polynomial fit for  $R > 12'$ . The *dashed curve* illustrates a second rotation curve with a higher minimum near  $R=10'$ . Figure taken from [4].

The curves in Fig. 1.1 show a rapidly rotating nucleus, followed by significant flattening out of the velocity profile at larger radii. The data ( $R > 3$  kpc) was cross-checked with radio data from Roberts and Rots [5], who used the 21-cm HI emission line to make similar measurements on M31. The optical and radio data agreed substantially<sup>1</sup>. Rubin and Ford also looked for deviations from circular orbits and found no evidence of non-circular movements in the majority of the galaxy. Thus, the dynamics of M31 should be simple. Using Newton's second law applied to circular orbits, one can easily establish the trend of an object's rotational velocity,  $v_{rot}$ , as a function of the distance from the gravitational center of mass:

$$\frac{GMm}{r^2} = \frac{mv_{rot}^2}{r} \quad (1.2)$$

where  $G$  is the gravitational constant,  $M$  is the total mass contained within the radius  $r$ , and  $m$  is an object's mass at that radius. Therefore, the velocity of the object is proportional to the inverse square root of the radius from the galactic center:

$$v_{rot}(r) = \sqrt{\frac{GM(r)}{r}} \quad (1.3)$$

where  $M$  is shown explicitly as a function of the radius. If it were merely the case where all the mass was contained in luminous objects, then the velocities at larger radii within the disk would fall much faster than the data suggest, and would follow a trend similar to the exponential falloff of light intensity. Therefore, some mass was not accounted for and was considered to be missing. In order to get a feel for just

---

<sup>1</sup>It is important to note that HI emission lines offer the ability to measure rotational velocities well beyond the visible disks, however the measurement often suffers from large instrument errors at small radii, where resolution is poor. For example, a similar data set taken from the Virgo cluster around the same time did not show the same agreement as for M31. Comparisons were made later using improved synthesis telescopes and further improved using high-resolution images of CO emissions, and the majority of spiral galaxies showed optical and radio agreement similar to the M31 data. See [6] and [7] references therein.



how much mass was missing, Rubin and Ford computed precise mass-to-light ratios ( $M/L$ ) using optical data and masses obtained from fitted rotational velocity curves. The results were clear. The objects emitting light simply lacked enough mass to produce the curves. It was even shown that a significant amount of mass probably lies beyond the optically visible disks, leading to very high  $M/L$  ratios, possibly  $\mathcal{O}(10)$  or more, at large disk radii. This is especially true for elliptical (E) and lenticular (S0) galaxies. The dynamics and density profile of these galaxies can be quite complex, depending on the extent of visible matter and presence of substructure (*e.g.* central supermassive black hole, bright core and/or a bar). One can follow a similar virial line of reasoning that was described for galaxy clusters in Section 1.1.1 to determine velocity dispersions and total mass, but large inaccuracies result [8]. Another approach is to apply stellar hydrodynamics to the galaxy's nucleus only, assuming a Gaussian velocity distribution and constant velocity dispersion throughout the nucleus [9]. This method yields accurate results for the very central regions, but has to be applied separately in regions outside the nucleus [10, 11] in order to obtain results for the entire galaxy. Even when corrections are added to account for ellipticity, anisotropic velocity dispersions and angular projection onto the celestial sphere, or, when possible, direct velocity observations are made (*e.g.* rotating gas in E galaxies and individual stars in S0 types), there is still a considerable amount of mass that seems to be missing. Typical  $M/L$  ratios for spiral, E and S0 galaxies are reported within the Holmberg radius and are generally  $\mathcal{O}(10)$  [8]. However, these ratios can be  $\sim 100$  in extreme outer regions of these galaxies, indicating that the total mass continues to increase well beyond the visible matter. For spiral galaxies, it has been shown that the total mass increases approximately linearly with radius,  $M(r) \propto r$ , even at distances of several 10's of kpc from the galactic center [12]. Some examples are shown in Fig. 1.2a.

In conjunction with the initial  $M/L$  measurements, Freeman [13] demonstrated that a self-gravitating exponential disk required more than just mass located within the plane of the disk to produce the observed kinematics. He suggested that the disk must be embedded in a sort of halo of dark matter that was perhaps spherical and isotropic in nature and extended beyond the disk plane. This led to more detailed assumptions of a galaxy's density profile and entirely reshaped the philosophy of disk galaxy dynamics. For example, in 1985, van Albada *et al.* [14] applied the disk + halo model and successfully fit the rotation curve of NGC 3198. The curves shown

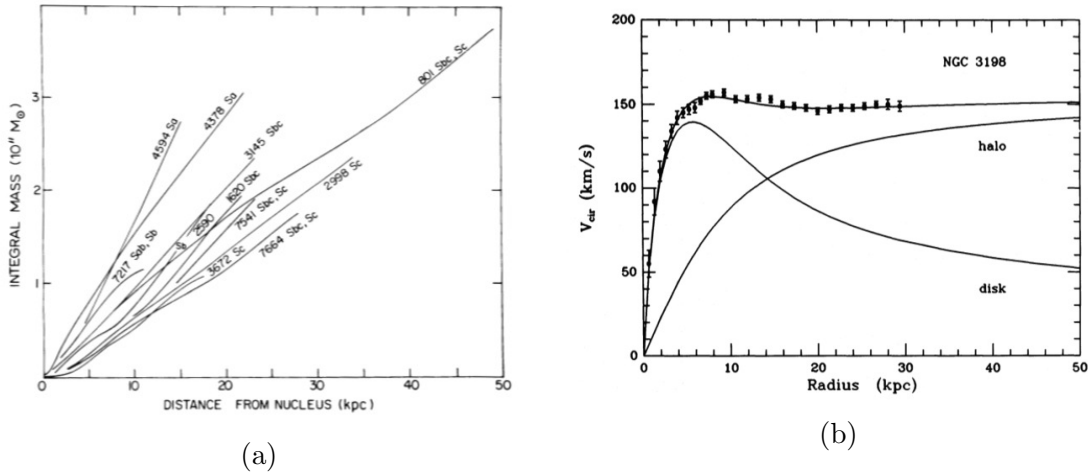


Figure 1.2: (a) shows the total integrated mass inside a given disk radius  $r$ , as a function of  $r$  for 11 spiral galaxies of varying morphology, showing approximate linear behavior. These are determined from rotational velocity data, extending out to the last measured velocity. The vertical scale corresponds to a disk model. Applying a spherical model implies a 40% increase in mass on this scale. The steeper slopes generally correspond to early type galaxies. Figure taken from [12]. (b) shows the rotational velocities (*dots with error bars*) in NGC 3198 as a function of distance from the galactic center. The two labeled curves show the individual contributions from the exponential disk and the dark matter halo. The upper curve is the sum of the two individual curves, with parameters  $a$  and  $\gamma$  adjusted in the halo density (see Eq. 1.4) for proper fit to the data points. Figure taken from [14].

in Fig. 1.2b, are calculated assuming a “maximum mass” exponential disk and de Vaucouleurs spheroidal bulge component plus a dark matter halo with density:

$$\rho_{halo}(R) = \rho_{halo}(0) \left[ 1 + \left( \frac{R}{a} \right)^\gamma \right]^{-1} \quad (1.4)$$

where  $R$  is the radius,  $\rho_{halo}(0)$  is the density at  $R = 0$ ,  $\gamma$  is a free parameter, and  $a$  sets the disk scale length related to the half-light radius,  $R_h$ .

Various other assumptions can be made about the actual mass density profile, however, a simple and fairly accurate approximation is obtained for the mass contained within a given radius,  $R$ , assuming that a galaxy’s mass density,  $\rho$ , is equal to a constant density term divided by the square of the radius (  $\rho = \rho_0/r^2$  ):

$$M(R) = \int_0^R 4\pi r^2 \rho(R) dr \approx \int_0^R 4\pi r^2 \frac{\rho_0}{r^2} dr = 4\pi \rho_0 R \quad (1.5)$$

Substituting this result into Eq. 1.3, the following approximation is obtained for rotational velocity that is independent of radius:

$$v_{rot} \approx \sqrt{\frac{G(4\pi\rho_0 R)}{R}} = \sqrt{4\pi G\rho_0} \quad (1.6)$$

This simple relationship is a special case of an Einasto profile ( $\rho \propto r^{-N}$ ) with  $N = 2$ . Data taken out to several half-light radii show that  $v_{rot}$  curves seem to asymptotically approach this value at distances well beyond the visible disks, where  $\rho_0 \approx \rho_{halo}$  [15]. At the present time, some of the most popular density profiles are of the form:

$$\rho(r) = \rho_0 \exp \left[ - \left( \frac{r}{a} \right)^{1/n} \right] \quad (1.7)$$

where  $n$  is the Einasto index, and  $\rho_0$  and  $a$  are the central density and scale length

defined below with  $\rho_{-2}$  and  $r_{-2}$  being the density and radius where  $\rho \propto r^{-2}$ .

$$\rho_0 = \rho_{-2} e^{2n} \quad (1.8)$$

$$a = \frac{r_{-2}}{(2n)^n} \quad (1.9)$$

More recent parameterizations of a universal dark matter profile used in N-body simulations is [16]:

$$\rho(r) = \frac{\rho_0}{\left(\frac{r}{R}\right)^\gamma \left[1 + \left(\frac{r}{R}\right)^\alpha\right]^{(\beta-\gamma)/\alpha}} \quad (1.10)$$

where  $R$  is a scale length set by physical system type and parameterization technique.

Thus, by the late 1970's, the scientific community had strongly motivated reasons to believe in dark matter on the kilo- and mega-parsec scales and the search for more astrophysical evidence was really heating up. There remained much to explore on both the extremely large cosmic scale of the entire universe and on the relatively small, sub-kpc scale. It turns out that the case for dark matter remains compelling on all of these scales as we will see in the remaining sections of this chapter.

### 1.1.3 Dwarf galaxies

Stellar clusters on the sub-kpc scale are very dim, but tracking down and examining these dim collections has unveiled a valuable source of evidence for dark matter. Many of these systems are located in our own galaxy's backyard, but prior to the 1900's, only two Milky Way satellite galaxies were known to exist. They were discovered in 1519 by Magellan and appropriately named the Large Magellanic Cloud (LMC) and Small Magellanic Cloud (SMC). Up until the early 21st century, only the brightest of the Milky Way satellites could be visually identified. This changed in 2005 with the Sloan Digital Sky Survey (SDSS) [17] and the 6dF project [18],

where modern, fiber-optically fed imaging techniques enabled highly resolved detection of ultra-faint stellar over-densities above the cosmic background that previously went unnoticed. Fig. 1.3 shows a map of Milky Way satellite galaxies and their approximate relative locations in the sky.

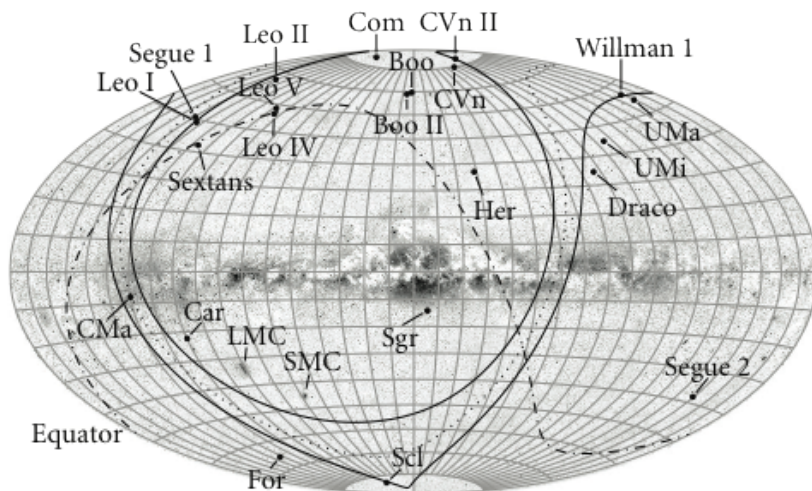


Figure 1.3: Map of satellite galaxies within the Milky Way’s virial radius of  $\sim 250$  kpc. These galaxies are loosely arranged in a plane nearly perpendicular to the galactic plane and is centered on the *dotted curve* with arbitrarily chosen  $\pm 15^\circ$  band (*solid curves*). Figure from [19].

The objects being catalogued are located within  $\sim 420$  kpc or so from Earth and fall into the categories of globular clusters (GC) and dwarf galaxies. GC’s tend to be metal-rich stellar systems with relatively low half light radii of  $\lesssim 10$  pc, compared to the metal-poor dwarf galaxies with half light radii in the range  $\sim 20$ –500 pc [20, 21, 22]. The dwarf galaxies are fairly spherical with little to no overall rotation, and so are referred to, with the exception of the LMC and SMC, as dwarf spheroidal (dSph) galaxies. Fig. 1.4 shows a summary of Milky Way dSph’s and

the curious and unique trend of their approximately constant integrated mass within  $\sim 300$  pc from their center as a function of total luminosity [23].

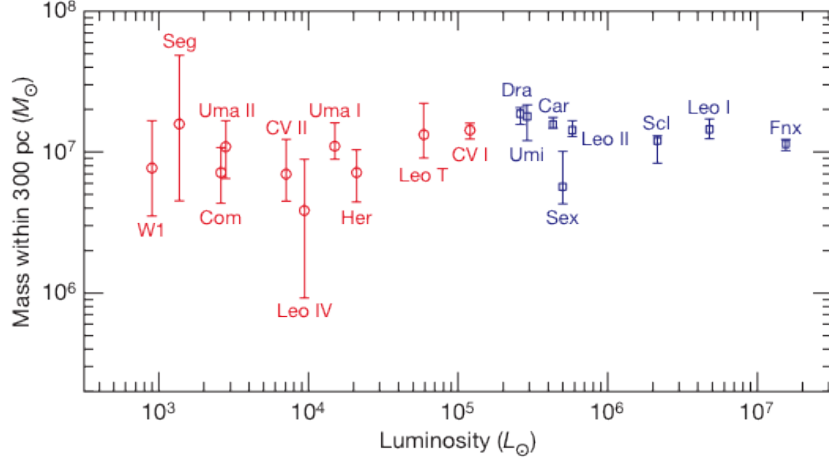


Figure 1.4: Total mass integrated within 300 pc ( $M_{300}$ ) from each dSph center in units of solar masses ( $M_{\odot}$ ) vs total luminosity ( $L_{\odot}$ ). The brightest dSph galaxies were discovered prior to the SDSS and are shown in the right portion of the plot (*blue squares*) and the fainter dSph's found in the SDSS era are in the left portion (*red circles*). Error bars indicate the points where the likelihood function falls off to 60.6% of its peak value. Figure from [23].

The lack of rotation of both GC's and dSph's makes it impossible to derive properties from  $v_{rot}$  curves as in the case of the disk type galaxies discussed in Section 1.1.2 [22]. However, the total mass and  $M/L$  ratios can still be determined from direct photometric observation and from dynamical masses derived from line-of-sight velocity dispersions, using, for example, the Jean's equations [20, 21, 24], coupled with N-body simulations [25, 26]. Additionally, one has to carefully account for tidal and other dynamical effects due to the influence of external gravitational fields (*e.g.* from the Milky Way and M31), but these effects are subdominant by a

factor of  $\sim 100$  or so below the local gravitational fields [22]. For the most part, external gravitational fields have already stripped away any matter lying outside a dwarf galaxy’s tidal radius. Most of the Milky Way’s dSph galaxies and many GC’s have been studied in depth, with 1000’s of line-of-sight velocities now recorded [27, 28]. The analysis shows that GC’s have  $M/L \sim 1$ , suggesting that they are dominated by stellar matter, with very low dark matter density. This is not at all the case for dSph galaxies, with typical  $M/L \sim 100$  or so. The accumulated statistics are now good enough to conclusively rule out conventional “mass-follows-light” models for dSph’s [22]. More information will soon be available with the recent launch of the GAIA satellite, which aims to provide more accurate measurements of positions and velocities affecting about a billion stars in our galaxy, including the GC’s and dSph’s [29].

So far, the dSph galaxies are thought to be the most common type of galaxy in the universe, and may have the highest dark matter density of any other stellar objects [30, 31]. Their proximity to host galaxies also gives more clues to the larger galaxy’s compositions and reveals intrinsic details about galactic, and, in turn, cosmological evolution. The dSph’s are vital to understanding our universe and the pivotal role played by dark matter.

## 1.2 Cosmological Evidence for Dark Matter

The astrophysical evidence discussed in the previous sections provides part of the historical motivation for developing “local cosmologies” that require the presence of dark matter (*i.e.* up to the scale of galaxy clusters). Examining the evidence on larger scales requires a brief mention of modern cosmology and dark matter’s central role in its formulation. An overview is given in Sec. 1.2.1 and the remaining subsections present cosmological evidence within this standard framework.

### 1.2.1 Building a modern cosmology

Einstein's general theory of relativity results in a homogeneous and isotropic space. In other words, when the Universe is viewed as a whole, all points and all directions in it are equivalent; a result known as the cosmological principle. There is, so far, no evidence to the contrary, so any cosmological model must include this principle as a fundamental building block. It must also explain the flatness and expansion of space, primordial nucleosynthesis and the tiny fluctuations in the Cosmic Microwave Background (CMB), while remaining consistent with the evidence discussed in Section 1.1. This has led to a standard cosmological model that generally includes five evolutionary stages of the Universe: 1) Inflation 2) Reheating 3) Radiation dominated stage 4) Matter dominated stage 5) Modern stage of accelerated expansion. Space-time in this scenario is quantified by the Friedmann-Lemaître-Robertson-Walker (FLRW) metric, according to which a line segment is defined (in hyper-spherical coordinates and true cosmological time) as:

$$ds^2 = dt^2 - a^2 \left( \frac{dr^2}{1 - kr^2} + r^2 d\theta^2 + r^2 \sin^2 \theta d\phi^2 \right) \quad (1.11)$$

where  $t, r, \theta$  and  $\phi$  are co-moving coordinates,  $k = \{-1, 0, +1\}$  defines the curvature of space as being open, flat or closed, respectively, and  $a$  is the scale factor describing how the physical distance between points scales as space expands or contracts. It is important to note that  $a$  can only be a function of time,  $a \rightarrow a(t)$ , otherwise, various points in space would scale differently causing the cosmological principle to break down.

Now consider the Einstein equations in their most general form:

$$R_{\mu\nu} - \frac{1}{2} \mathcal{R} g_{\mu\nu} = 8\pi G T_{\mu\nu} + \Lambda g_{\mu\nu} \quad (1.12)$$



where  $R_{\mu\nu}$  is the Ricci tensor,  $\mathcal{R}$  is the Ricci scalar,  $g_{\mu\nu} = \text{diag}(-1, a^2, a^2, a^2)$ ,  $G$  is Newton's gravitational constant,  $T_{\mu\nu}$  is the stress-energy tensor for all fields present and  $\Lambda$  is the cosmological constant. To begin solving these equations, we make simple assumptions about the *rhs* of Eq. 1.12. First of all, since the FLRW metric is symmetric and diagonal, then  $T_{\mu\nu}$  must assume the same form. Second, isotropic space requires equality of all spatial components,  $T_{ij}$ . Lastly, we neglect any shear stress and assume that the Universe is a perfect fluid with time-dependent energy density  $\rho(t)$  and pressure  $p(t)$ , which leads to  $T^\mu{}_\nu = \text{diag}(-\rho, p, p, p)$ . (We must utilize the transformation  $T_{\mu\nu} = g_{\sigma\mu}T^\sigma{}_\nu$  in order to remain consistent with the chosen sign convention and keep track of the additional scale factor terms that appear in the steps below.) From here, we apply the conservation of stress-energy ( $T^{\mu\nu}{}_{;\nu} = 0$ ) to derive the 1st law of thermodynamics in terms of parameters given above:

$$d(\rho a^3) = -pd(a^3) \quad (1.13)$$

The *lhs* of Eq. 1.13 is the change in energy within a co-moving volume element  $a^3$ , which is equal to minus the pressure times the change in volume. In this form, we can build an equation of state,  $p = w\rho$ , where  $w$  is independent of time, and the energy density evolves as  $\rho \propto a^{-3(1+w)}$ . Thus, the value of  $w$  essentially determines the evolutionary stages of the Universe:

$$\begin{aligned} \text{Radiation Dominated Stage : } p &= \frac{1}{3}\rho \Rightarrow \rho \propto a^{-4} \\ \text{Matter Dominated Stage : } p &= 0 \Rightarrow \rho \propto a^{-3} \\ \text{Vacuum Energy Dominated Stage : } p &= -\rho \Rightarrow \rho \propto \text{const.} \end{aligned} \quad (1.14)$$

This simple model aligns with stages 3 thru 5 mentioned above. Stages 1 and 2 can be understood as a very brief, extreme vacuum energy dominated stage (Inflation)

followed by the decay of the vacuum energy into matter (Reheating). With this interpretation in mind, we solve for the  $0 - 0$  and  $i - i$  components of Einstein's equations:

$$\frac{\dot{a}^2}{a^2} + \frac{k}{a^2} - \frac{\Lambda}{3} = \frac{8\pi G}{3}\rho \quad (1.15)$$

$$2\frac{\ddot{a}}{a} + \frac{\dot{a}^2}{a^2} + \frac{k}{a^2} - \Lambda = -8\pi Gp \quad (1.16)$$

where Eq. 1.15 is referred to as the 1st Friedmann equation with the additional cosmological constant included. Now subtracting Eq. 1.15 from Eq. 1.16, we obtain an equation describing the acceleration of the scale factor over time:

$$\frac{\ddot{a}}{a} = -\frac{4\pi G}{3}(\rho + 3p) + \frac{\Lambda}{3} \quad (1.17)$$

Qualitatively, Eq. 1.17 shows that matter and radiation slow down the expansion of the Universe, indicated by the minus sign on the *rhs*, whereas the expansion is accelerated by the vacuum energy. We make a few more substitutions to extract measurable quantities and to frame the solution explicitly in the context of matter-energy densities. Define the Hubble rate as  $H \equiv \dot{a}/a$ , which measures how quickly the scale factor changes with time. Eq. 1.15 can now be written in terms of  $H$ :

$$H^2 = \frac{8\pi G}{3}\rho - \frac{k}{a^2} + \frac{\Lambda}{3} \quad (1.18)$$

Rearranging to solve for density yields:

$$\rho = \frac{3H^2}{8\pi G} + \frac{3k}{8\pi Ga^2} - \frac{\Lambda}{8\pi G} \quad (1.19)$$

We are now interested in identifying the so-called critical density  $\rho_c$  that makes the above solution consistent with a flat ( $k = 0$ ), expanding Universe. We can neglect the

cosmological constant for now. The Universe in this particular scenario (Einstein-de Sitter) would expand forever at a slower rate over time. This gives  $\rho_c$  in terms of the present value of the Hubble rate  $H_0 \equiv \dot{a}_0/a_0$ , where usually  $a_0 = 1$ :

$$\rho_c \equiv \frac{3H_0^2}{8\pi G} \quad (1.20)$$

Finally, dividing Eq. 1.18 by  $H_0^2$  and recalling that the energy density can be scaled from any arbitrary time to the present by  $\rho_0 = (a^3/a_0^3)\rho$  leads to the most useful form of the 1st Friedmann equation:

$$\left(\frac{H}{H_0}\right)^2 = \Omega_m \left(\frac{a_0}{a}\right)^3 + \Omega_k \left(\frac{a_0}{a}\right)^2 + \Omega_\Lambda \quad (1.21)$$

Thus, the dynamics of the most simple cosmology are defined in terms of three basic parameters:

$$\Omega_m = \frac{\rho_0}{\rho_c} \quad (1.22a)$$

$$\Omega_k = -\frac{k}{a_0^2 H_0^2} \quad (1.22b)$$

$$\Omega_\Lambda = \frac{\Lambda}{3H_0^2} \quad (1.22c)$$

where  $\rho_0$  is the present matter energy density and  $\Omega_m$ ,  $\Omega_k$  and  $\Omega_\Lambda$  define the matter, curvature and vacuum energy densities, respectively, as measured relative to the critical density. It is trivial to see that these three parameters can be related to each other by setting time in Eq. 1.21 equal to the present time ( $a \rightarrow a_0$  and  $H \rightarrow H_0$ ), which yields:

$$\Omega_m + \Omega_k + \Omega_\Lambda = 1 \quad (1.23)$$

Thus, we have arrived at an elementary result describing the Universe's total

energy budget that is testable using data in the present epoch. Recent results indicate the flatness of space with incredible precision [32], and so we can more confidently assume that  $\Omega_k \approx 0$ , which leaves only the matter and vacuum energy terms to realistically consider. The vacuum energy is now more commonly known as “dark energy” and appears to consume a hefty portion of the energy budget at  $\Omega_\Lambda = 0.686 \pm 0.020$ . The remaining  $\Omega_m$  can be broken up into two parts;  $\Omega_b = 0.048583 \pm 0.000168$  describing the fraction of matter energy from baryonic matter and  $\Omega_c = 0.26328 \pm 0.00158$  describing the contribution from cold dark matter (CDM). These results are the most recent findings from [32], assuming a Hubble constant  $H_0 = 67.3 \pm 1.2 \text{ km s}^{-1} \text{ Mpc}^{-1}$  and likelihood fits with a standard  $\Lambda$ CDM cosmology, also from [32]. It is interesting to note that these numbers have fluctuated some over the past several years. The value for  $H_0$  is the lowest reported yet (see summary plot in Fig. 1.5), which coincides with a decrease in  $\Omega_\Lambda$ , and a subsequent increase in  $\Omega_m$  from previous results. For example, using Hubble’s law with data obtained from Cepheids and Type Ia Supernovae, higher values of  $H_0 \approx 74 \text{ km s}^{-1} \text{ Mpc}^{-1}$  are obtained [33], while previous CMB experiments put the value around  $H_0 \approx 71 \text{ km s}^{-1} \text{ Mpc}^{-1}$  [34]. This is only a small set of constraints on the energy densities and is merely a starting point to build more sophisticated cosmologies. The most successful so far ( $\Lambda$ CDM) results in CDM comprising around 26% of all matter and energy, making dark matter a central player in the evolution of the Universe. In fact, from the results above, over 95% of all matter and energy is invisible!

### 1.2.2 Modified gravity

Clearly the above result depends heavily on our choice to work exclusively in the framework of Einstein’s theory of gravity. Modified theories of gravity have been proposed that do not require dark matter [35]. MOdified Newtonian Dynamics

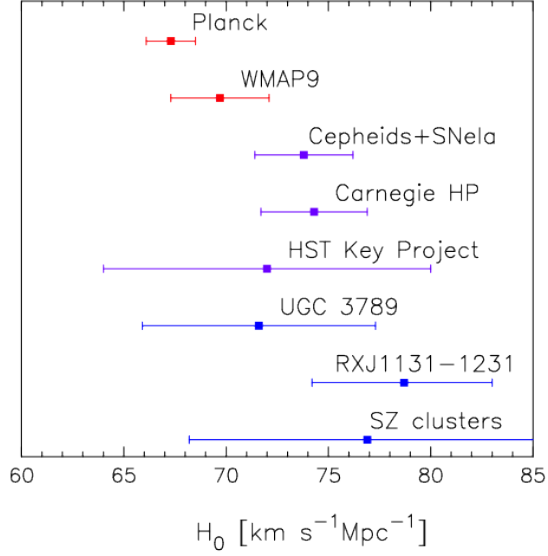


Figure 1.5: Summary plot showing the Hubble constant from several datasets as labelled. Figure from [32].

(MOND) is perhaps the most successful so far at explaining several astrophysical phenomena with little to no dark matter and no fine-tuning of parameters [35]. Essentially, in the MOND framework, the Newtonian acceleration is scaled by a new constant  $a_0$ , whose average value  $\bar{a}_0$  is related to the speed of light  $c$  and the Hubble constant by  $\bar{a}_0 \approx cH_0$ . In fact, the value of this new constant  $a_0 = (1.20 \pm 0.25) \times 10^{-8} \text{ cm s}^{-2}$  appears to be “coincidentally” related to estimates of  $\Lambda$  via  $\bar{a}_0 \approx c(\Lambda/3)^{1/2}$ . MOND is also very appealing from an aesthetic standpoint, because it does not require a detailed knowledge (or any knowledge) of a system’s history to accurately describe the dynamics on scales  $\lesssim$  galaxy clusters.

The remaining challenges for MOND are to explain large scale structure formation and the details of the CMB. A promising attempt is being made with a relativistic extension of MOND known as Tensor-Vector-Scalar (TeVeS) theory, but much more work needs to be done to fully explore its implications and validate it on the cosmic

scale [36].

Neither MOND nor TeVeS fully rule out the existence of dark matter. At a minimum, when compared to  $\Lambda$ CDM, they suggest that dark matter’s role in the evolution of galaxies and clusters is diminished. So even a total paradigm switch to a modified gravity theory does not spell the end for dark matter necessarily. For now, though, general relativity remains the most robust and thoroughly vetted gravitational theory, so we will stick to the formulation outlined above in this framework and not consider modified theories any further. The next few sections will explore other areas of cosmology that generate tighter constraints on the mass energy densities within the  $\Lambda$ CDM model.

### *1.2.3 Gravitational lensing and cluster collisions*

The evidence addressed so far has been dynamical in nature, based on movements of objects within the gravitational potential by which they are bound. Another way to probe these immense gravitational fields and assess their profile, independent of a local dynamical model, is by observing the interaction of photons passing by. Although massless, photons must still follow a geodesic path through space. This path is very accurately predicted by general relativity, independent of what “type” of matter is gravitating and causing the curvature. Thus, retracing a photon’s steps on its path to Earth offers a great deal of insight into the mass profiles with which it came into contact along the way.

#### *1.2.3.1 Strong gravitational lensing*

A simple 2D example geometry is shown in Fig. 1.6. This effect is known as strong gravitational lensing, where an object with high mass density in the image plane (foreground) acts as a lens by magnifying and distorting the image of the source (background) as viewed by the observer. In practice, the distances  $D_{LS}$  and

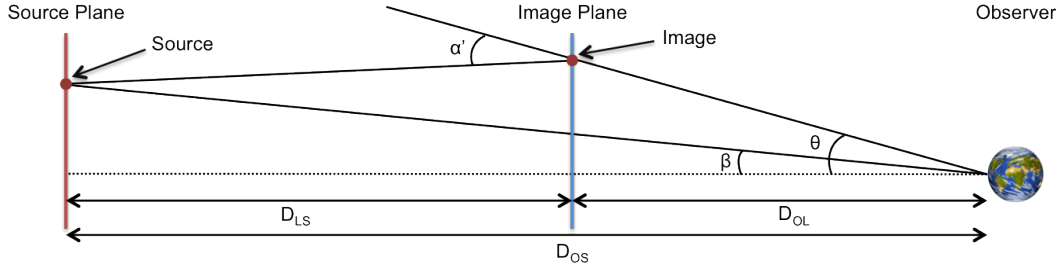


Figure 1.6: Example schematic diagram of a source (galaxy, quasar, etc.) of photons being gravitationally lensed by an object in the image plane and the path followed to an observer on Earth.

$D_{OL}$  are found by measuring the sources' redshifts and applying Hubble's law. The signs of strong lensing are fairly easy to observe, manifesting arcs, rings or multiple images of the source object. Strong lenses are commonly galaxies, clusters or super clusters of galaxies. One of the first extreme cases was seen in the cluster Abell 370, shown in Fig. 1.7, where multiple images of systems and giant arcs are seen through the lens of two main mass distributions. The mass of an extremely strong lens can be approximated by  $M(\theta < \theta_{ring}) = \pi \theta_{ring}^2 D_{OL}^2 \Sigma_{crit}$ , where  $\Sigma_{crit} = \frac{c^2}{4\pi G} \frac{D_{OS}}{D_{OL} D_{LS}}$  is the critical surface mass density.  $\Sigma_{crit}$  can be described as the uniform surface mass density spread out and projected onto the image plane corresponding to infinite image magnification. For an arbitrary mass distribution, multiple images will be formed as long as  $\Sigma > \Sigma_{crit}$ . For a given redshift,  $\Sigma_{crit} \approx \text{const.}$ , therefore the locations of arcs and rings lead to calculation of the total mass enclosed by the critical lines. Using the simple approximation above, and confirmed by more sophisticated techniques,  $M/L \sim 300$  were found for Abell 370 [38]. Many more strong lensing measurements have been made and, regardless of the type of mass reconstruction technique,  $M/L$  ratios of galaxies and clusters of galaxies range from  $\sim 10$  to over 100, suggesting that these systems are dominated by dark matter [39]. Further, the data shows that the

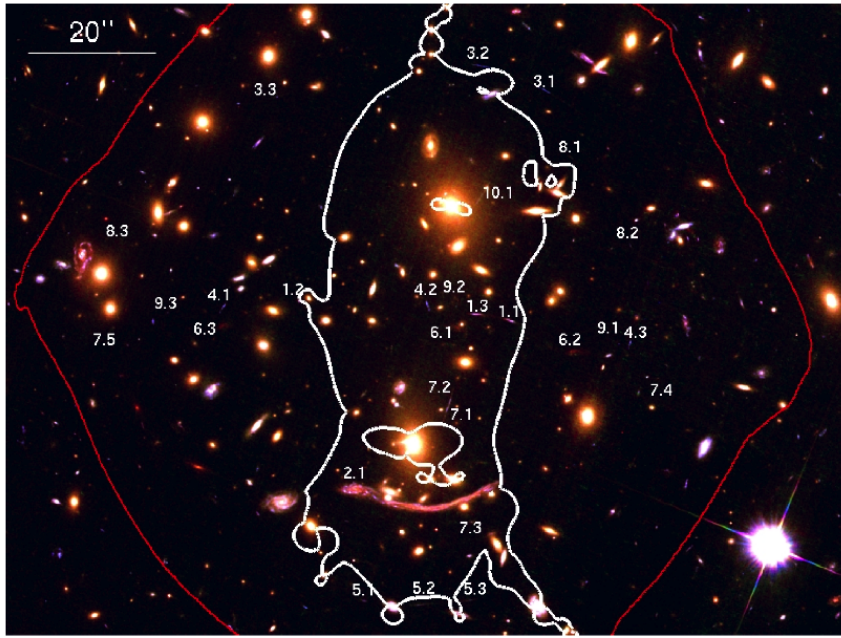


Figure 1.7: Optical image of Abell 370 in the foreground acting as a strong lens for galaxies in the background field. Multiple images of systems are numbered. The *white contour* corresponds to the critical lines of the lens (at  $z = 1.2$ ). The *red contour* outlines the region for multiple images of high redshift (here  $z = 6$ ) object. Figure from [37].



$M/L$  ratios scale with total mass and with radius from the system's center, as well as being approximately aligned with the luminous matter distribution (although a counter-example is claimed in [40] using multiple images of quasars and early elliptical and lenticular galaxies as lenses).

#### 1.2.3.2 *Weak gravitational lensing*

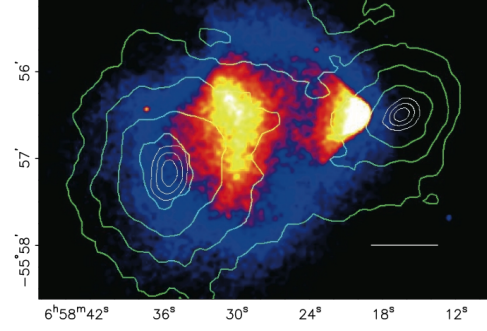
Any further conclusions regarding the mass of a lens must be combined with the more subtle weak lensing effect, which is seen as the distortion (formally characterized by ellipticity) of a background object by the gravitational shear as the photons pass by the lens. The effect is so weak that it is nearly impossible to observe in a single image of a lensed galaxy. Rather, many ellipticity measurements are taken from as many objects as possible from a single lens. This results in a statistical measurement of the gravitational shear, and combined with strong lensing provides a powerful tool for more accurately predicting the total mass, as well as the precise distribution. This technique even led to the discovery of a previously unknown system approximately aligned with, but in the background of a clearly visible lens [41].

#### 1.2.3.3 *Cluster collisions*

The crowning achievement thus far for strong+weak lensing data is seen in galaxy and cluster collisions. Two of the most famous examples, 1E0657-56 (*Bullet Cluster*) and MACS J0025.4-1222, are shown in Fig. 1.8, along with the recently discovered DLSC J0916.2+2951 (*Musket Ball Cluster*).



(a) 1E 0657-558 “Bullet Cluster”. Image from [42].



(b) 1E 0657-558 “Bullet Cluster”. Image from [43].



(c) DLSCl J0916.2+2951 “Musket Ball Cluster”. Image from [44].



(d) MACS J0025.4-1222. Image from [45].

Figure 1.8: (a) shows the Bullet Cluster X-ray data from Chandra in *false color*. (b) shows the Bullet cluster, with X-ray data (baryonic hot plasma) offset from the dark matter content profiled by the *white contours* from strong+weak lensing data. (c) and (d) show the X-ray data from hot gases (*pink*) spatially offset from the dark matter (*blue*).

The Bullet Cluster image in Fig. 1.8b shows the baryonic matter content in false color from X-ray data being spatially offset from the dark matter whose profile is indicated by the white contours as reconstructed from strong+weak lensing [43]. This single example was particularly interesting because it showed not only that galaxy

clusters are dominated by a dark component, but it also supported the idea that dark matter is essentially collisionless. The idea is that the cluster merged (collided) and the hot plasma (baryons) suffered from a ram pressure from gas particle collisions and experienced a drag force while the dark matter simply sailed through the collision, not affected by pressure and drag forces. This seemed a triumph at the time, but this litmus test began to fail in data from other clusters (*e.g.* Abell 520 [46]) casting some doubt on the quality of the analyses and biasing of lensing data. With this doubt in mind, it is appropriate to ask whether galaxy collisions/mergers can necessarily provide evidence against dark matter. The answer is “No”, because even alternative theories (MOND, TeVeS, Hot Dark Matter, etc.) can not fully explain the data.

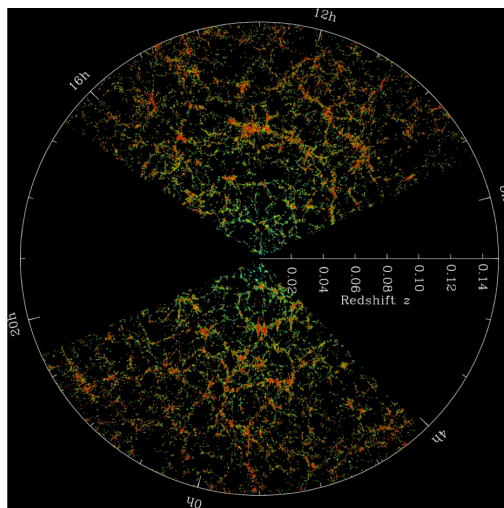
The data from gravitational lensing is building rapidly now, as the field flourishes with new interest and highly developed analysis techniques. The number of cataloged lensed objects has grown to the point that conclusions can be drawn about the large scale structure of the Universe. Again sticking with general relativity as the underlying gravity theory, lensing data leads to a value of  $\Omega_m \sim 0.25$  in the  $\Lambda$ CDM framework. Specifically, weak lensing results in an approximation of the Universe’s power spectrum, fitting well with a hierarchical CDM-dominated model of structure formation [38]. More details on large scale structure are discussed in Sec. 1.2.4.

#### 1.2.4 *Cosmic microwave background*

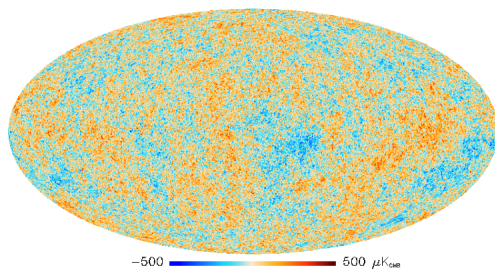
The wealth of phenomena discussed above provides the necessary ingredients to build a detailed static picture of the observable Universe. However, the fundamental questions remain: “How did the Universe begin, how did it evolve into this ‘current’ state and does the story of dark matter really fit into a coherent answer to these questions?” We have already discussed many clues offered by Nature that can be made consistent with dark matter from the scales of dwarf galaxies up to clusters of

galaxies, but we need to look even farther away and earlier in time to truly answer these questions and decide whether dark matter is intrinsic to our Universe.

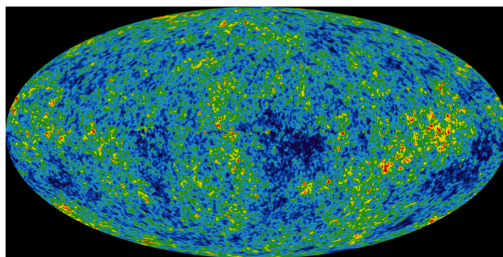
Thanks to optical surveys and meticulous spectrographic measurements (SDSS, 2dFGS and 6dFGS), we now have redshift data from over a million galaxies, which can be used to form a detailed map of our Universe. An example of such a map is shown in Fig. 1.9a, which goes out to about two billion light years from Earth. The surprising feature is the “clumpiness” of matter on these scales. The images show that space is primarily isotropic and empty, with average galaxy density  $\bar{\rho}_{galaxy} \approx 10^5 \times \bar{\rho}_{universe}$  and average cluster density  $\bar{\rho}_{cluster} \approx (10^2 - 10^3) \times \bar{\rho}_{universe}$ , but there seems to be structure on scales well beyond galaxies and clusters. The indication of large scale structure formation is an important clue for developing a precise cosmological model. Even if we go all the way back to the time of last scattering around 380,000 years ( $z \approx 1100$ ) after the Big Bang, we still see signs of a Universe that is not perfectly smooth. Observationally, this is as far back in time that Nature will allow us to “see”, so any details about earlier times must be inferred from measurements of the resulting black body spectrum. Recently, the Planck collaboration released its remarkable high resolution CMB data. The low frequency spectrum is shown in Fig. 1.9b, which suggests that these large scale structures began forming extremely early in the Universe’s history. It is believed that before the photons began free-streaming at the time of last scattering, the baryons and photons were in thermal equilibrium. The entire “visible” Universe was in causal contact in a radiation dominated era with the photons providing a net negative pressure that kept any matter from gathering together into clumps from gravitational forces. If this were merely the case, then our Universe would indeed have retained its smoothness, with the matter being spread much more evenly than what we observe. Ultimately, the plasma cooled and coalesced, also forming light elements (at recombination), the



(a) Image from [47].



(b) Image from [48].



(c) Image from [49].

Figure 1.9: (a) shows a 2D slice from a 3D map of the local galaxy distribution out to  $z = 0.15$  from SDSS-III. The Earth is at the center and each dot represents a galaxy color coded by the age of each galaxies star content (*red* indicates older stars). The missing wedges are not included because the data there is obscured by dust from the Milky Way. (b) shows the low frequency (30 Hz) full sky map of the CMB from Planck. (c) is the less resolved CMB from WMAP.

details of which will be discussed in Sec. 1.2.5. The point here is that there must have been something present to provide the seeds of gravitational attraction prior to recombination. So, a form of matter that interacts extremely weakly to photons and baryons was added to the theoretical cosmic landscape during this period. The idea is that this matter will not “feel” the immense pressure provided by the radiation. Therefore, the weakly interacting matter was free to collapse, falling into its own

gravitational wells. As this non-baryonic matter clustered, the gravitational forces became locally stronger and began to overcome the plasma pressure. Baryons began clumping alongside the dark matter. One important thing to note here, is that the weakly interacting dark matter could not have been relativistic. Otherwise, it would have escaped the gravity wells in this scenario. As a result, this form of dark matter is said to be cold, leading to the term “cold dark matter”. With the entire Universe no longer in causal contact, photons began to free-stream, retaining their characteristic frequency, which over time has been stretched by the expansion of space. The free-streaming photons provide the measured signals of the CMB.

The information encoded in the CMB is derived from the black body spectrum with peak temperature  $T \sim 2.725$  K and fluctuations in the  $\mu\text{K}$  range. The most telling feature of the CMB lies in the details of the fluctuations (anisotropies), which are interpreted using a spherical harmonic expansion of the temperature variation as a function of pairs of projected angles on the sky [50]:

$$\frac{\delta T}{T}(\theta, \phi) = \sum_{\ell=2}^{+\infty} \sum_{m=-\ell}^{+\ell} a_{\ell m} Y_{\ell m}(\theta, \phi) \quad (1.24)$$

The variance  $C_\ell$  of  $a_{\ell m}$  can be written as:

$$C_\ell \equiv \langle |a_{\ell m}|^2 \rangle \equiv \frac{1}{2\ell + 1} \sum_{m=-\ell}^{\ell} |a_{\ell m}|^2 \quad (1.25)$$

The quantity usually plotted comes from the result of assuming Gaussian fluctuations, in which case all of the information is encoded in the power spectrum  $\mathcal{D}_\ell = \ell(\ell + 1)C_\ell/(2\pi)$ . These fluctuations arise from pressure oscillations of the baryonic matter, which would look much different than the actual CMB data if we stuck with the critically damped scenario outlined above. However, as the baryons

began to fall into the dark matter gravity wells, the radiation pressure acted as a restoring force, similar to a mass on a spring in a gravitational field. The details of the resulting harmonic oscillations of the collapsing baryons are encoded in the temperature of the photons, as compressed regions raised the photon temperature and the less dense rarefactions led to lower photon temperatures (adiabatic perturbations). Additionally, the oscillations were driven by the change in relative strength of the gravitational potentials and the radiation pressure. As more baryons collected in the dark matter wells, more drag force was experienced, leading to further red shifting of the photons (Sachs-Wolfe perturbations). This also affects the phase of the oscillations relative to the cosmic horizon by acting in a similar sense to a shift in the zero point of an oscillating mass-spring system. The apparent “brightness” of the temperature arises from an additional Doppler shift due to the non-zero velocity of the plasma at recombination. The resulting temperature power spectrum (see Fig. 1.10) provide the strongest support to date for the  $\Lambda$ CDM cosmology, leading to the matter energy densities already mentioned at the end of Sec. 1.2.1. It also yields vital information needed to break degeneracies between the plethora of pre-recombination theoretical scenarios. For example, the anisotropies are now measured with fine enough precision to rule out Non-Gaussianity (NG) in the CMB [32]. This supports a very basic model of Inflation, which is driven by a single scalar field that “slowly” decayed, producing a two-point power spectrum consistent with the CMB data and the optical and lensing surveys previously mentioned. Some of the latest results from the CMB were already mentioned in Sec. 1.2.1 and we summarize these results graphically in Sec. 1.2.5. Another way to summarize the current understanding of the age and evolutionary stages of the Universe is shown through artistic interpretation (Fig. 1.11), which caricatures time and space from the Big Bang to the present.

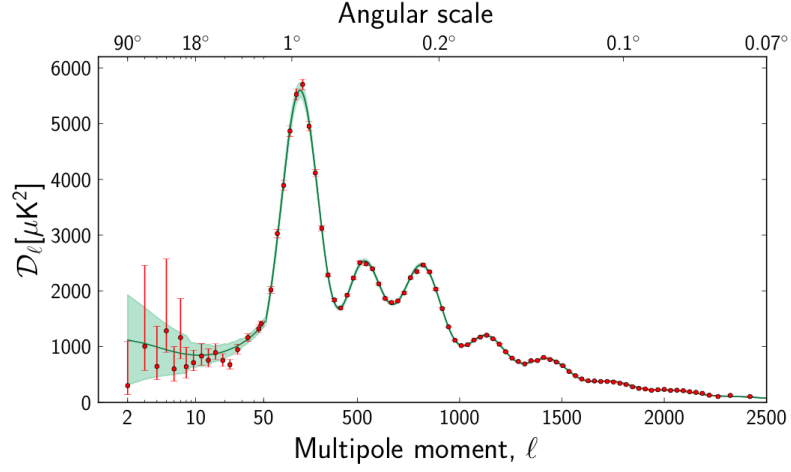


Figure 1.10: Temperature angular power spectrum as a function of angular separation and multipole moment from Planck 2013 CMB data, where  $\mathcal{D}_\ell = \ell(\ell+1)C_\ell/2\pi$ . The *dark green curve* is a best-fit  $\Lambda$ CDM model with errors bars and *light green shaded region* including error and cosmic variance. Figure from [51].

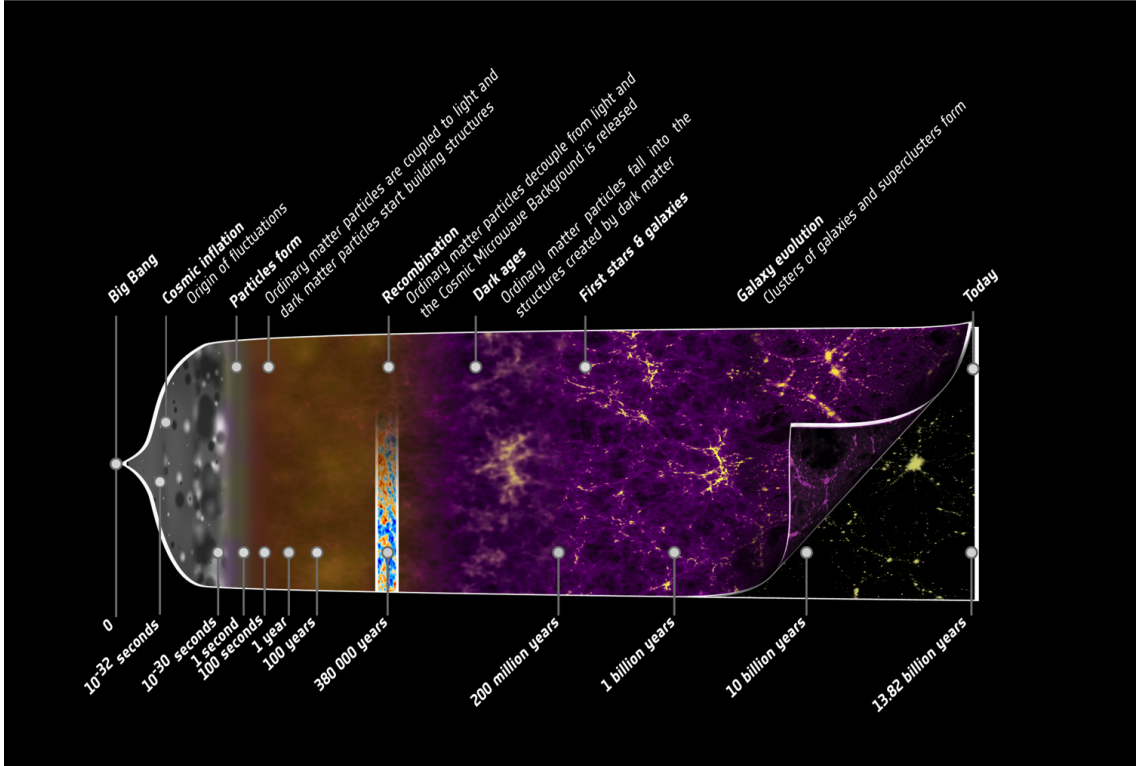


Figure 1.11: Artistic representation of the evolution of the Universe with numbers derived from Planck 2013 CMB data. Figure from [52].



### 1.2.5 *Big bang nucleosynthesis*

The  $\Lambda$ CDM cosmology offers a consistent picture of the Universe from the moment just before recombination to today. It corroborates evidence on vast scales placing ever tighter constraints on  $\Omega_m$ ,  $\Omega_k$  and  $\Omega_\Lambda$ . However, we have not discussed whether these constraints, especially on  $\Omega_m$ , are necessarily consistent with conditions required to synthesize ordinary matter in the ratios we observe. These conditions are defined by the well-understood theory of Big Bang Nucleosynthesis (BBN), which occurred during the cosmic time period between  $t \sim 0.1 - 10^4$  s. The CMB provides many important details from this period, but BBN offers a separate theoretical and observational check. The resulting primordial abundances of elements from BBN are highly sensitive to the available baryon-to-photon ratio  $n_B/n_\gamma = \eta$  through the relation  $\Omega_b = 3.66 \times 10^7 \eta h^{-2}$  where  $100h = H_0 \text{ km s}^{-1} \text{ Mpc}^{-1}$  [53]. Thus, calculating and measuring these abundances allows us to understand the microscopic conditions that led to their formation and infer cosmological details back to mere fractions of a second after the Big Bang. We do not speculate to much earlier times, as there is, as yet, no “standard” model for the GUT scale.

According to the standard model of BBN, the bulk of the currently observed light elements (D,  $^3\text{He}$ ,  $^4\text{He}$ ,  $^7\text{Li}$ ) were produced during the first few minutes of cosmological time, as the Universe cooled from the hot Big Bang [54, 55, 56]. The Universe was radiation dominated during this time, so the energy density scaled as  $\rho \propto a^{-4}$ . Since the volume scaled faster than the energy, the energy per co-moving volume decreased, causing subsequent lowering of temperature. At temperatures  $10 \text{ MeV} \gtrsim T \gtrsim 1 \text{ MeV}$ , weak interactions were in thermal equilibrium leading to

neutron  $n$  and proton  $p$  number densities being driven by nuclear statistics:

$$(n/p)_{eq} = \exp[-Q/T] \quad (1.26)$$

where  $Q \equiv m_n - m_p = 1.293$  MeV. The Boltzmann equations characterizing number densities relative to entropy are schematically shown as in [57]:

$$\frac{dY_i}{dt} = -H(T)T \frac{dY_i}{dT} = \sum (\Gamma_{ij}Y_j + \Gamma_{ikl}Y_kY_l + \dots) \quad (1.27)$$

where  $i = {}^1\text{H}, n, \text{D}, {}^4\text{He}$ , etc,  $\Gamma_{ij\dots}$  are the generalized rates for element interconversion and decay,  $H(T)$  is the temperature-dependent Hubble expansion rate and the  $Y_i = n_i/s$  are the temperature dependent ratios of number density  $n_i$  to entropy  $s$ .  $H(T)$  is represented by the statistical formula:

$$H(T) = T^2 \times \left( \frac{8\pi^3 g_* G}{90} \right)^{1/2} \quad (1.28)$$

where  $G$  is Newton's gravitational constant and  $g_* = g_{boson} + (7/8)g_{fermion}$  with  $g$  defining the statistical degrees of freedom. For  $T \gtrsim 1$  MeV, nearly all the baryon content is shared equally in the form of  $n$  and  $p$ , with other elements at essentially zero abundance. At a time  $t \sim 1$  sec, and temperature  $T \sim 1$  MeV, conditions are such that the weak interactions that interconvert neutrons and protons “freeze out” (*i.e.*  $\Gamma$  becomes smaller than  $H$ ). The equilibrium ratio of neutrons to protons at freeze-out is  $(n/p)_{freeze-out} \simeq 1/6$ . In the next three minutes or so,  $0.3 \text{ MeV} \gtrsim T \gtrsim 0.1 \text{ MeV}$ , some of the neutrons have undergone weak decay, lowering the ratio to  $n/p \simeq 1/7$ . At this point, the ratio  $n/p$  is essentially fixed, with the remaining neutrons ending up in the light element with the highest binding energy,  ${}^4\text{He}$ . Heavier elements are suppressed due to relatively large Coulomb barriers, and lighter elements are

photodisintegrated rapidly due to extremely high photon flux ( $\eta^{-1} \sim 10^{10}$ ) and low binding energies. Therefore, D (and  $^3\text{He}$ ) and  $^7\text{Li}$  occur in trace amounts of  $\mathcal{O}(10^{-5})$  and  $\mathcal{O}(10^{-10})$  respectively. The  $^4\text{He}$  mass fraction  $Y_p$  can be approximated by:

$$Y_p \simeq \frac{2(n/p)}{1 + (n/p)} \simeq 0.25 \quad (1.29)$$

Experimentally determined cosmic abundances are reported relative to hydrogen content and are very difficult to obtain. One must utilize old, metal poor sources, since a high metal content indicates stellar processing that alters the element counts. The measurements are then used to infer primordial abundances. Ratios of  $^4\text{He}/\text{H}$  are found by observing H and He emissions in HII regions illuminated by young stars in compact blue galaxies. D is only destroyed (converted to  $^3\text{He}$ ) in stars, so its abundance necessarily decreases over time, providing a lower bound on primordial D. Measurement of D/H is done by observing absorption lines as the light from high redshift quasars passes through low-metallicity clouds.  $^3\text{He}$  can be created or destroyed in stellar processes leading to  $\sim$ constant value of  $(\text{D}+^3\text{He})/\text{H}$ . As a result of these trends, measurements of the ratio  $^3\text{He}/\text{D}$ , taken from chemically evolved species within the Milky Way, provide a firm upper limit on primordial  $^3\text{He}/\text{D}$ .  $^7\text{Li}/\text{H}$  is measured in low-metallicity objects in the Milky Way's galactic halo. The data shows an anomalous constant value of  $^7\text{Li}/\text{H}$  over a wide range of metallicities. The measured  $^7\text{Li}/\text{H}$  are also lower than the standard BBN predicted value by a factor as high as  $\sim 4$  or so. This suggests that the amount of  $^7\text{Li}$  is not significantly altered by stellar processes, and the anomaly may have a cosmic origin, even outside the standard BBN context. The primordial abundances of the light elements are summarized in Fig. 1.12 from both Standard BBN and from the CMB. The calculated cosmological constraints from a combination of the CMB, supernovae (SNe) and BAO

are shown in Fig. 1.13.

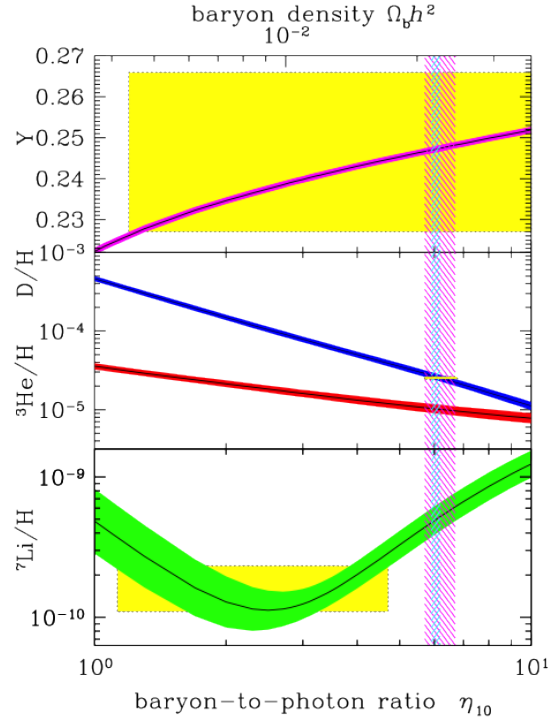


Figure 1.12: Abundances of  ${}^4\text{He}$ ,  $\text{D}$ ,  ${}^3\text{He}$ ,  $\text{Li}$  from Standard BBN predictions as a function of baryon-to-photon ratio, with 95% CL bands shown in color. The colored boxes are measured values. The two vertical bands show the baryon density from CMB (*narrow*) and the BBN concordance range (*wide*). Figure from [53].

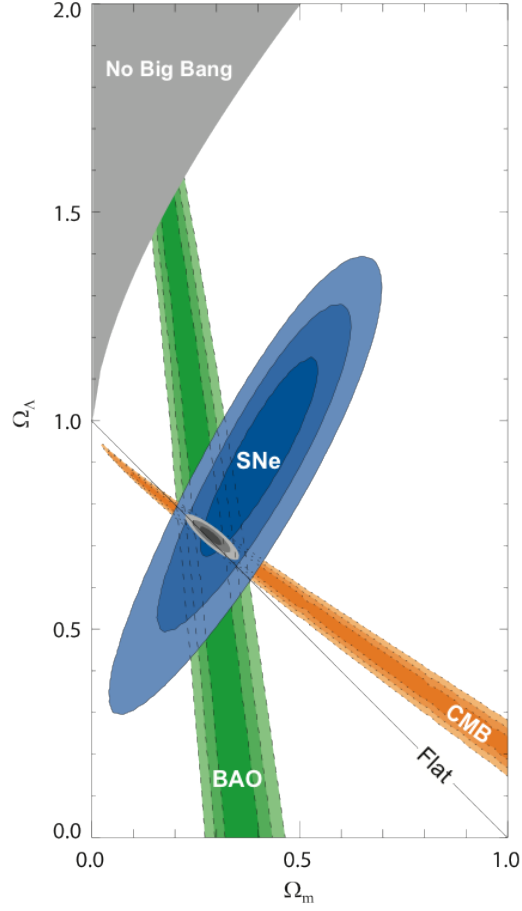


Figure 1.13: Cosmological constraints on  $\Omega_\Lambda$  and  $\Omega_m$  from Cosmic Microwave Background (CMB), Supernovae (SNe) and Baryon Acoustic Oscillation (BAO) data showing 68.3%, 95.4% and 99.7% confidence contours. The *grey* contours illustrate the combination from all three sources assuming a vacuum energy dominated equation of state ( $w = -1 \Rightarrow p = -\rho \Rightarrow \rho \propto \text{const.}$ ). The line labeled “Flat” indicates the trend for a flat Universe ( $k = 1$ ). Figure from [58].

Using the predicted abundances from standard BBN and the observed D/H,  $^4\text{He}/\text{H}$  and  $^7\text{Li}/\text{H}$  values, a 95% CL for the baryon-to-photon ratio can be determined:  $4.9 < \eta_{10} < 6.4$ , reported in units of  $\eta_{10} = \eta \times 10^{10}$  [59]. This is converted to

a total baryon density range:

$$0.018 < \Omega_b h^2 < 0.023 \quad (1.30)$$

Assuming the Planck result,  $H_0 = 67.3 \text{ km s}^{-1} \text{ Mpc}^{-1}$  and the central value  $\Omega_b h^2 = 0.020$  from Eq. 1.30, leads to a total baryon density  $\Omega_b \approx 0.044$ .

The light element abundances, combined with the latest CMB data from Planck yield the tightest constraints on  $\Lambda$ CDM parameters. In particular, the Planck results provide huge support for the basic six-parameter  $\Lambda$ CDM cosmology. Some of the relevant dark matter parameters are summarized in Table 1.1 and the matter energy content of the Universe is shown graphically in Fig. 1.14.

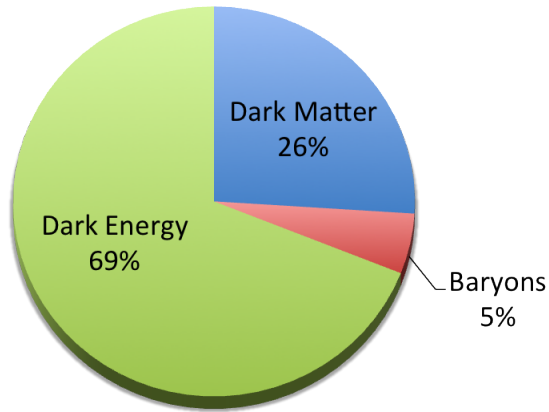


Figure 1.14: Matter energy content of the Universe using cosmological parameters from the most recent Planck results summarized in Table 1.1.

Table 1.1: Summary of dark matter cosmological parameters. The table is reproduced from [32], where the most recent results from Planck were combined with the other astrophysical data listed in parallel.

	Planck + WMAP	Planck + Lensing + WMAP + highL	Planck + WMAP + BAO + highL
Age of Universe (Gyr)	$13.817 \pm 0.048$	$13.794 \pm 0.044$	$13.798 \pm 0.037$
$H_0$	$67.3 \pm 1.2$	$67.9 \pm 1.0$	$67.8 \pm 0.77$
$\Omega_b$	$0.04868 \pm 0.00062$	$0.04897 \pm 0.00057$	$0.04888 \pm 0.00053$
$\Omega_c$	$0.2647 \pm 0.0060$	$0.2619 \pm 0.0049$	$0.2621 \pm 0.0038$
$\Omega_\Lambda$	$0.685^{+0.018}_{-0.016}$	$0.693 \pm 0.013$	$0.692 \pm 0.010$

### 1.3 Dark Matter Candidates

Astrophysics and cosmology provide an overwhelming body of evidence in support of dark matter, all but demanding its existence. Even alternative theories of gravity require some amount of matter that has not been seen directly. The next step is to reveal the nature of dark matter and determine why it continues to elude direct observation. Understanding its nature and behavior may be the most important key to establishing a true standard cosmological model as well as finalizing or expanding the Standard Model (SM) of particle physics. This section is presented in terms of a hierarchy of existence, similar to [60]. I discuss existing matter that contributes to  $\Omega_m$ , then move to well-motivated candidates for non-baryonic forms, and finish with more exotic solutions to the missing mass problem.

#### 1.3.1 Baryonic dark matter

Many efforts have been made to reconcile the missing mass in the Universe with a very high baryonic contribution ( $\Omega_b \sim 1$ ) to the total matter energy density  $\Omega_m$ .

On the one hand, this led to postulation of theories involving non-standard BBN in a baryon-inhomogeneous environment (remnants of GUT scale physics) or BBN with a super-symmetric extension [57, 61]. On the other hand, the simple observational approach has been to look for baryonic matter located in galactic halos. In general, these objects are known as MAssive Compact Halo Objects (MACHOs) in the form of black holes, brown/white dwarfs, star remnants, Jupiter-Like Objects (JLO) and possibly even frozen, cold or hot H gas [62].

H is observed in large abundance relative to the total baryon mass in the Universe. However, H can not account for the mass of an entire galactic halo for several reasons. The cases of frozen (solid) and cold H are ruled out with simple electrostatic and thermodynamic arguments, and a large density of hot H gas conflicts strongly with X-ray observations [62].

An exploding star ejects  $\sim 40\%$  of its matter in the form of heavy elements. This process could account for some of the galactic halo, but the large number of low-metallicity objects observed, and lack of theoretical support for such a fine-tuned scenario involving several cycles of stellar processing precludes this as a viable option [63].

Experiments have limited MACHOs in the mass range  $0.6 \times 10^{-7} M_{\odot} < M < 30 M_{\odot}$  to  $\lesssim 40\%$  of the Milky Way's galactic halo mass [64, 65]. This does not include other mass ranges, which may be detected in the future via gravitational waves [66]. The limit above only includes brown/white dwarfs, JLO's and baryonic black holes. More recent surveys suggest that the bulk of MACHO mass could be made up of white dwarfs, with a total contribution to the galactic halo of  $\sim 20\%$ . However, these results are subject to much criticism due to small sample sizes and limited chemical pathways leading to the production of the white dwarfs [67].

The overall results of astronomical surveys (primarily from micro-lensing) indicate



that the Milky Way’s halo is mostly non-baryonic, with the 100% baryonic halo hypothesis ruled out at the 95% CL in the above mass range [62, 65, 67]. At any rate, the baryonic matter should all be accounted for in the CMB data and BBN calculations, so these results do not significantly alter the hypothesis of non-baryonic dark matter.

### *1.3.2 Non-baryonic dark matter: Standard model*

#### *1.3.2.1 Standard model neutrinos*

The most obvious place to look for non-baryonic sources of dark matter is the Standard Model. The only remaining SM suspects are the three flavors of light neutrino ( $\nu_e, \nu_\mu, \nu_\tau$ ). Until recently, though, it was not known whether neutrinos were massive. Observations of flavor oscillations show undeniable evidence for neutrino mass [68, 69], making them exciting dark matter candidates. The excitement for 100% light neutrino dark matter dwindles rapidly when calculating neutrino masses and relic abundances. A direct mass measurement is not yet available, but using the flavor oscillation data, we can infer limits on the masses and use the limits to place constraints on the neutrino contribution to  $\Omega_m$ . This is done by recalling that the frequency of flavor oscillation is proportional to the difference of the squares of the masses from flavor one to flavor two:

$$\Delta m_{12}^2 = m_2^2 - m_1^2 \tag{1.31}$$

This equation and a positive oscillation observation necessarily implies that at least one neutrino flavor mass is greater than zero, but an argument from the data can be made that at least two are non-zero. Oscillation from muon neutrinos to tau neutrinos are seen from cosmic ray collisions in the Earth’s upper atmosphere. The

mass difference has been calculated (in natural units,  $c = 1$ ) [53, 68]:

$$\nu_\mu \rightarrow \nu_\tau, \quad \Delta m_A^2 \sim 2.4 \times 10^{-3} \text{ eV}^2 \quad (1.32)$$

Signals from solar neutrinos going from electron neutrinos to either muon or tau neutrinos give the result [53, 69]:

$$\nu_e \rightarrow \nu_\mu, \nu_\tau, \quad |\Delta m_\odot^2| \sim 7.6 \times 10^{-5} \text{ eV}^2 \quad (1.33)$$

A lower limit on the mass of the heaviest neutrino is easily approximated by taking the square root of the largest mass difference (assuming the lighter flavor mass is zero) [53]:

$$m_{\text{heaviest } \nu} = m_3 \gtrsim 0.048 \text{ eV} \quad (1.34)$$

Laboratory experiments involving  $^3\text{H}$   $\beta$ -decay and accelerator-based measurements have set upper limits on all three flavors [53, 70, 71]:

$$m_1 \lesssim 2.5 - 2.8 \text{ eV}, \quad m_2 \lesssim 190 \text{ keV}, \quad m_3 \lesssim 18.2 \text{ MeV} \quad (1.35)$$

These values vary in the literature, see for example [72, 73, 74, 75]. Combining these upper limits with the small mass difference limits implies that the upper limit on the lowest mass most likely applies to all flavors  $m_i \lesssim 2.5 - 2.8 \text{ eV}$ , ( $i = 1, 2, 3$ ). With these masses in hand, we can proceed in determining a relic abundance along the same lines as in Sec. 1.2.5 from standard BBN. If all neutrino flavors were in thermal equilibrium at the time of BBN, then the statistical formula for the relic abundance results in [50]:

$$\Omega_\nu h^2 = \sum_{i=1}^3 \frac{g_i m_i}{93 \text{ eV}} \quad (1.36)$$

where  $g_i = 1$  for Majorana neutrino and  $g_i = 2$  for Dirac neutrino. The above equations are used in conjunction with CMB, gravitational lensing and large scale structure to form following limits:

$$0.05 \text{ eV} < m_1 + m_2 + m_3 < 0.7 \text{ eV} \quad (1.37)$$

$$0.0006 < \Omega_\nu h^2 < 0.0076 \quad (1.38)$$

Using the most recent CMB result from Planck ( $H_0 = 67.3 \text{ km s}^{-1} \text{ Mpc}^{-1}$ ) gives the expected neutrino contribution to the overall matter energy density:

$$0.0013 < \Omega_\nu < 0.017 \quad (1.39)$$

The good news is that  $\Omega_\nu > 0$ , so we have indeed identified one form of non-baryonic dark matter. Unfortunately, it only makes up a tiny fraction of the expected dark matter content. We should roughly expect this, because neutrinos are not consistent with all of the requirements for an acceptable single candidate. Although neutrinos are non-luminous and non-baryonic, they are relativistic and would have escaped the gravitational wells responsible for large scale structure formation in the early Cosmos. Because of this, neutrinos are referred to as Hot Dark Matter (HDM).

### *1.3.3 Non-baryonic dark matter: Beyond the standard model*

We have effectively run out of dark matter candidates within the extent of known physics. There appears to be no more reasonable astrophysical or cosmological options to explore and we have spanned the entire SM in our theoretical search. The only choice appears to be physics beyond the SM. In order to postulate a new particle dark matter candidate, we first require certain minimal properties. The particle must

have a substantial (and precise) relic density and should not have decayed away in large amounts from the early Universe. It must also, obviously, interact very weakly with electromagnetic radiation. The remaining “well-motivated” candidates that possess these qualities are sterile neutrinos, axions, Primordial Black Holes (PBHs) and the class of Weakly Interacting Massive Particles (WIMPs).

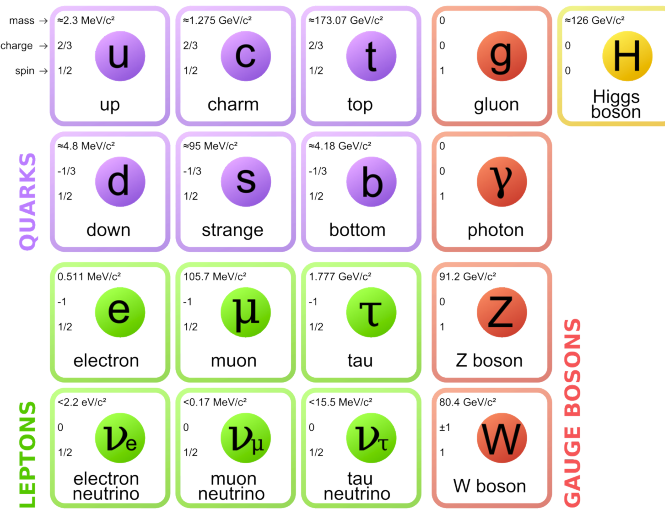


Figure 1.15: Summary of SM particles. Figure from [76].

### 1.3.3.1 Sterile neutrinos

Sterile neutrinos were proposed in 1994 [77] as an effort to explain large scale structure formation at times ( $T \sim 100 \text{ MeV}$ ) earlier than what is predicted by the standard CDM model, without straying too far from the SM. In fact, sterile neutrinos are basically just right-handed SM neutrinos. At tree level, they couple to SM neutrinos through a mixing angle, decaying into a left-handed neutrino and a photon,  $\nu_s \rightarrow \nu_L + \gamma$ . The idea is that sterile neutrinos were always produced at a rate

lower than the expansion rate and, thus, never reached thermal equilibrium during structure formation. This leads to a particle mass of  $\sim$  few keV with a radiative decay width longer than the age of the Universe and a possible detectable decay signal (photons as X-rays) [78, 79]. The term for this type of dark matter is therefore Warm Dark Matter (WDM). At first glance, the sterile neutrino is a fantastic DM candidate, with the exciting possible side-effect of solving the “cusp/core problem” of densities at galactic centers [80]. Unfortunately, the argument for this type of relic neutrino loses much of its steam by requiring unreasonably high lepton asymmetry  $\geq 10^{-3}$  and lacking detection of the resulting mono-energetic X-ray photon signal [53]. Also, the recent Planck CMB data places a very strong constraint on the number of relativistic degrees of freedom  $N_{eff} = 3.30 \pm 0.27$  and an upper limit of  $\sum m_\nu < 0.23\text{eV}$  on the sum of neutrino masses [32]. The Planck constraint on  $N_{eff}$  gets even tighter when combined with deuterium measurements and goes to  $N_{eff} = 3.02 \pm 0.27$ , consistent with standard BBN value of  $N_{eff} = 3.046$  [32]. This significantly limits the parameter space leaving the remaining option of sterile neutrino production in the very early Universe by the decay of some heavy particle [81]. Future prospects in observation remain motivated and are being pursued [82]. At this point, even fractional “effective neutrinos” are being proposed, which could possibly account for extra  $\sim 0.3$  in  $N_{eff}$  [83].

#### 1.3.3.2 *Primordial black holes*

Primordial black holes could make up a significant amount (or all) of dark matter if certain additional constraints are imposed, outside of those that led to the micro-lensing limits seen above. An interesting case is made if we assume that PBHs collapsed prior to nucleosynthesis, such that they are not subject to standard BBN baryonic mass constraints. It has been proposed that PBHs could have collapsed

as early as the QCD phase transition time  $\sim 10^{-5}$  sec [84], perhaps in a double Inflation scenario [85]. Production mechanisms are not further discussed here, although very interesting, I instead focus on conditions leading to an observable mass domain. The available window to investigate seems to be  $m_{PBH} \lesssim 0.6 \times 10^{-7} M_\odot$  and  $m_{PBH} \gtrsim 30 M_\odot$ , however, Hawking radiation would cause complete evaporation for  $m_{PBH} \lesssim 0.25 \times 10^{-20} M_\odot$  over the course of cosmic evolution [86]. Data from femto-lensing, the CMB and energetic gamma rays from galactic centers suggest that the only mass domains left to explore are  $10^{-17} M_\odot \lesssim m_{PBH} \lesssim 10^{-19} M_\odot$  and  $10^{-13} M_\odot \lesssim m_{PBH} \lesssim 10^{-7} M_\odot$  [87]. Thus, some phase space remains open for future PBH searches, including the possibility of gravitational wave signatures left from their coalescence. At a minimum, PBHs could be a nice complement to other particle dark matter candidates. One group even claims that re-analysis of the micro-lensing data is consistent with primordial non-baryonic black holes comprising most, if not all, of the dark matter content in the already excluded PBH mass ranges [84]. A larger data sample is needed to settle the issue, which signifies a healthy pathway for thriving future research.

### 1.3.3.3 Axions

The candidates discussed so far were primarily proposed to solve the missing mass problem. Axions are different in that regard, since they were proposed to reconcile a specific issue in particle physics, the strong CP problem [88, 89, 90]. The parameters strictly motivated by particle physics make axions relevant non-baryonic dark matter prospects. When these particles are thrust into the dark matter mix, a cosmological upper limit on the mass arises from calculation of the decay rate into photons,  $a \rightarrow \gamma\gamma$ . A loose upper limit of  $m_a \lesssim 20$  eV results from requiring axions to survive the age of the Universe with a meaningful abundance [79]. A

tighter limit comes from the fact that axions are able to escape astrophysical objects (*e.g.* red giants and supernovae) and carry away significant quantities of energy. Measurements on these bodies and others produce a dramatically lower mass limit  $m_a \lesssim 10$  meV [79, 91]. A lower bound on the mass is driven by several theoretical factors. If the mass is too small, the Universe may become over-closed. A very light axion could also evade detection quite easily until a dramatic improvement of detection technology is realized. Also, depending on the exact time of Inflation, axions could represent either a very small part or entirely all of the dark matter content. The combination of these wide-ranging possibilities may demote axions into the “exotic” category, therefore the appropriate mass range for search corresponding to reasonable set of cosmological conditions is  $6 \mu\text{eV } \theta_i^2 \lesssim m_a \lesssim 6 \text{ meV}$ , where  $\theta_i$  is a constant  $\leq 1$ , depending on the time period of Inflation [50, 79]. Direct detection experiments have come up empty-handed so far, but future axion searches are highly anticipated [92, 93, 94, 95, 96, 97, 98].

#### 1.3.3.4 WIMPs

Sterile neutrinos, PBHs and axions are indeed interesting and relevant options for non-baryonic dark matter, but none of them necessarily lead to the correct relic abundance. The class of particles that do have the correct relic abundance, fitting very neatly into the  $\Lambda$ CDM cosmology, are WIMPs. In fact the WIMP is a sort of Goldilocks scenario, possessing the perfect set of properties to endorse the vast body of cosmological and astrophysical evidence leading up to the dark matter hypothesis. In order to postulate such a particle, we must migrate into the rich theoretical world of supersymmetry (SUSY), which essentially states that every SM particle has a super-partner with an identical set of quantum numbers, but differs by half-integer spin. Thus, every fermion has a boson super-partner and vice versa. SUSY was

originally proposed to solve the problems dealing with hadrons in particle physics [99, 100, 101], but the historical evolution and theoretical spinoffs pertaining to dark matter have been fascinating.

A surplus of SUSY particles may exist, especially depending on the reader's preference in applying the theory, but the example of interest here comes from some amount of mixing of the spin-1/2 fermions, Wino ( $\tilde{W}$ ), Bino ( $\tilde{B}$ ) and Higgsino ( $\tilde{H}$ ), which result in four mass eigenstates known as neutralinos [50, 79]:

$$\tilde{B}, \tilde{W}^3, \tilde{H}_1^0, \tilde{H}_2^0 \rightarrow \chi_1, \chi_2, \chi_3, \chi_4 \quad (\text{Neutralinos}) \quad (1.40)$$

Of course, the WIMP may very well turn out to be a linear combination of other fundamental particles, again depending on one's preference on how to extend the SM. Whatever its true makeup, the WIMP could solve many problems at once. The best candidate yet is the lightest of the neutralino mass eigenstates in Eq. 1.40, the Lightest Supersymmetric Particle (LSP), which comes from the Minimal Supersymmetric SM (MSSM). The relic density of such a particle can be calculated, independent of the physical model characterizing its composition. Similar to the BBN scenario described above in Sec. 1.2.5, we assume that WIMPs were in thermal (and chemical) equilibrium in the hot, early Universe. The Boltzmann equation governing the WIMP number density ( $n_\chi$ ) as a function of the Hubble parameter ( $H$ ) and a balance between its production ( $n_\chi^{eq}$ ) and self-annihilation ( $n_\chi$ ) terms is:

$$\frac{dn_\chi}{dt} + 3Hn_\chi = -\langle\sigma_A v\rangle [(n_\chi)^2 - (n_\chi^{eq})^2] \quad (1.41)$$

where  $\langle\sigma_A v\rangle$  is the thermally averaged WIMP annihilation cross section into lighter particles with relative velocity  $v$ , and  $t$  is time. At the time (temperature) of



freeze-out, the annihilation rate equals to, then drops below the expansion rate,  $\Gamma = n_\chi \langle \sigma_A v \rangle \lesssim H$ . At this point, the cosmic abundance is fixed, and the approximate relic density can be calculated relative to the critical density:

$$\Omega_\chi h^2 = \frac{m_\chi n_\chi}{\rho_0} \approx \frac{3 \times 10^{-27} \text{cm}^3 \text{s}^{-1}}{\langle \sigma_A v \rangle} \quad (1.42)$$

It is also useful to consider the variable  $Y = n/s$ , as in Eq. 1.27 and to combine the mass and photon temperature  $T$  into one term  $x = m/T$ . Combining Eq. 1.42 with the equation describing the evolution of entropy ( $s$ ):

$$\frac{ds}{dt} = -3Hs \quad (1.43)$$

we get the following Boltzmann equation from the conservation of entropy [102]:

$$\frac{dY_\chi}{dx} = \frac{1}{3H} \frac{ds}{dx} \langle \sigma_A v \rangle [(Y_\chi)^2 - (Y_\chi^{eq})^2] \quad (1.44)$$

Skipping some of the details, which can be found in [102] and included references, we simply note that a reasonable set of weak scale parameters leads to the relic density in terms of present day parameters, denoted by a script 0:

$$\Omega_\chi h^2 = \frac{\rho_\chi^0 h^2}{\rho_c^0} = \frac{m_\chi s_0 Y_0 h^2}{\rho_c^0} = 2.755 \times 10^8 Y_0 m_\chi / \text{GeV} \quad (1.45)$$

The quantity  $Y_0$  is most useful, because in the standard cosmology, the mass per entropy per co-moving volume is constant after freeze-out as seen in Fig. 1.16. Other interesting features clearly illustrated by Fig. 1.16 are the different relic abundances that result from the various adjustments of freeze-out time and cross section. For example, for a given WIMP mass,  $m_\chi$ , the relic abundance goes down the later the

WIMP freezes out. The fact that the simple  $\mathcal{O}(\text{weak scale})$  cross section applied

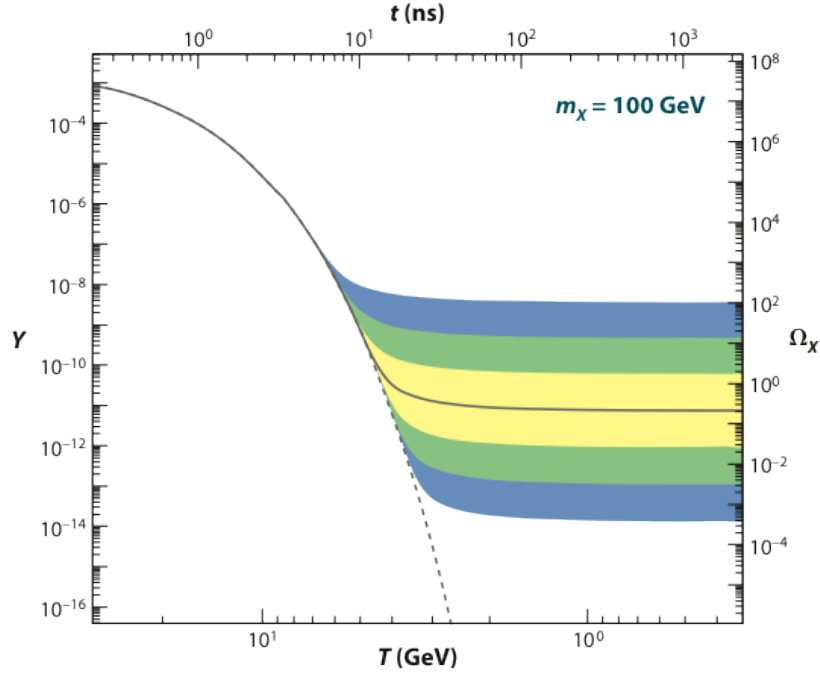


Figure 1.16: WIMP number density  $Y_\chi \rightarrow Y$  per co-moving volume for WIMP mass  $m_\chi = 100$  GeV and the resulting relic density,  $\Omega_\chi$ , as a function of cosmological time,  $t$ , and photon temperature,  $T$ . The *solid grey contour* corresponds to the cross section (and freeze-out time) that leads to the “correct” relic density. The shaded regions indicate parameter space covered by cross sections that differ from the correct one by factors of 10 (*yellow*),  $10^2$  (*green*) and  $10^3$  (*blue*) from the correct one. The *dotted grey contour* shows the result of a WIMP that never freezes out and remains in thermal equilibrium. Figure from [79].

to the LSP leads to the correct relic abundance is referred to as “The WIMP Miracle”, also making it possible to detect. Thus, the WIMP in the form of the LSP (neutralino) takes its preferred seat in the cosmic search for CDM.

The other electrically neutral SUSY particles are the superpartners of neutri-

nos, being the sneutrinos ( $\tilde{\nu}_e, \tilde{\nu}_\mu, \tilde{\nu}_\tau$ ) and that of the graviton, called the gravitino ( $\tilde{G}$ ). The sneutrinos are all but ruled out as dark matter WIMPs due to direct detection exclusion limits on the mass and cross section required for a correct relic abundance [103]. The gravitino is unique in that it only interacts via gravity, so is not a WIMP, and lies in the category of exotic non-WIMP candidates (more of a GIMP, so to speak). The gravitino would also be extremely difficult to detect, as well as being stable only under very precise cosmological circumstances [50].

Other candidates are not discussed in detail here, but the standard list of possibilities include extremely massive WIMPs in the range  $m_\chi \sim \text{few hundred TeV}$  (WIMPZILLAS), extra-dimensional possibilities with fractional baryon number (Kaluza-Klein states), and several others that are well-covered in the following reviews for example [50, 79, 103].

#### 1.3.3.5 *Emergence*

Another exotic consideration is the idea of emergence, which is characterized by behavior manifested in a system that can not necessarily be deduced from the sum of its parts using first principles. Examples of this sort of behavior are seen in biology and in the social sciences [104, 105]. For example, consider a family of humans living independently from a society. The family maintains its own supply of food and water, so support from outside the group is not needed for survival. Theoretically, the family would continue to survive until the youngest member dies of old age or disease, not being able to reproduce viable offspring with siblings. However, one day another family encroaches into family 1's territory, and, before long, family 2 brings a few million of its relatives. One would naively assume that each of the thousands of families has its own garden in which to cultivate food, and fresh mountain stream from which to drink. The reality is that land and water is limited, so this new

society has to develop an economy and government in order to develop and share its limited resources in a “fair” way, and thus survive. Otherwise, the population may self-annihilate under its own internal pressure by warring until a new steady state is reached. So, the properties of economy and government emerge from the collective group and place it in a lower energy eigenstate, minimizing the change in entropy and ultimately a new “culture” is born. These properties were not present before and can not be explained by the four forces of Nature. Perhaps these higher order social concepts revive the concept of quintessence. At any rate, emergent properties are somewhat mysterious and unexplained at the moment, but could be an interesting path forward. The concept of superconductivity is an example in physics [106]. With regard to cosmology, space-time may be subject to an emergent property when enough mass collects (under the four known forces of Nature) and goes beyond some critical emergence density, at which point a fifth force is “born” under the new order, manifesting peculiar behavior [107].

#### 1.4 Indirect Detection of WIMPs

We now proceed by considering the WIMP (*i.e.* the neutralino) as the most likely CDM particle. In order to prove that dark matter consists of neutralino WIMPs, we must somehow unravel its particle nature. Turning again to particle physics, the MSSM tells us that the WIMP may be indirectly observed by identifying the products of its self-annihilation or decay. When a WIMP self-annihilates, it forms pairs of SM particles which go on to produce detectable signals [108, 109, 110]:

$$\chi + \bar{\chi} \rightarrow q\bar{q}, W^+W^-, Z\bar{Z}, \dots \rightarrow \bar{p}, \bar{D}, e^+, \gamma, \nu \quad (1.46)$$

The best places to look for these signals are locations of high local dark matter density, since the annihilation rate is proportional to the density squared,  $\Gamma_A \propto$

$\rho_{DM}^2$  [50]. These occur in places where WIMPs may be gravitationally trapped (*e.g.* centers of galaxies and stars and in possible dark matter halo substructures). A weak annihilation signal is possible in the more diffuse outer regions of the dark matter halo, but the presence of locally dense regions could lead to the identification of point sources.

Many efforts are being made to detect the various signals. Neutrino experiments, primarily “aimed” at the sun are looking for neutrinos with a boost in total flux that has much higher energy than the standard solar-produced type. The null results in the neutrino energy range  $10 \text{ GeV} \lesssim E_\nu \lesssim 1 \text{ TeV}$  by the Super-Kamioka Nucleon Decay Experiments (Super-Kamiokande), IceCube Neutrino Observatory (IceCube), and Antarctic Muon and Neutrino Detector Array (AMANDA) have produced strong limits on several MSSM scenarios. The solar measurements can also be used to infer limits on the WIMP-nucleon spin-dependent scattering cross-section  $\sigma_{SD}$  assuming a model where the annihilation products decay into neutrinos, which is driven by  $\sigma_{SD}$  [79]. These limits, along with future spin-independent limits, will become extremely important to the search for low mass WIMPs discussed below.

Experiments looking for  $\bar{p}, e^+$  and  $\gamma$  signals are also producing interesting results by measuring the cosmic ray (CR) spectrum. The known process of CR nuclei interacting inelastically with interstellar gas leads to the production of charged pions that go on to decay into  $e^+, e^-, \nu$  [108, 109, 111]. The calculation of the relative flux  $\Phi_{e^+} = e^+/(e^+ + e^-)$  vs. energy shows that  $\Phi_{e^+}$  should decrease as the energy rises. Data from the Fermi Large Area Telescope (Fermi LAT), PAMELA, and the Alpha Magnetic Spectrometer (AMS) show that the positron flux actually rises with energy [112, 114, 113]. Some astrophysical solutions have been proposed to explain the results summarized in Fig. 1.17, but dark matter annihilation remains a viable description.

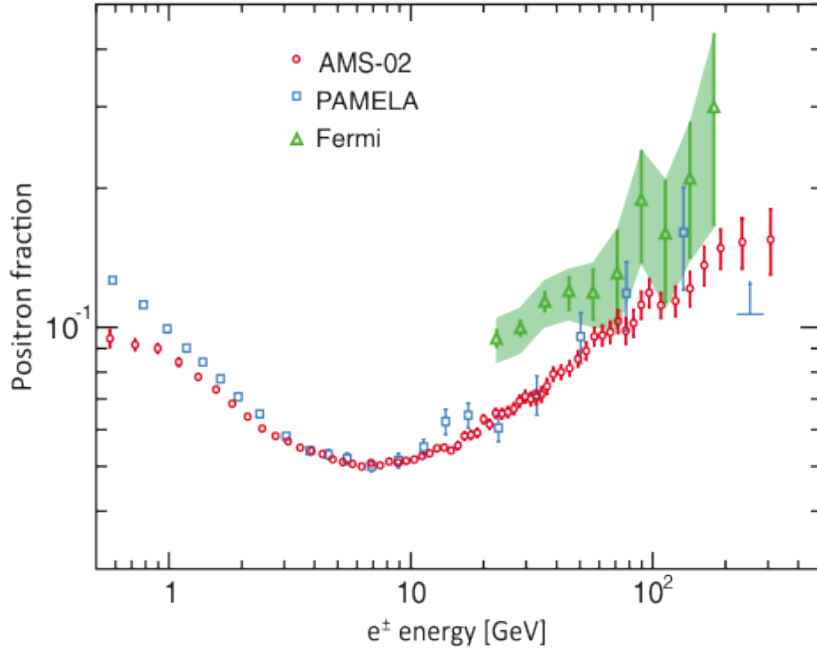


Figure 1.17: Summary of positron fraction measurements vs. electron-positron energy from the PAMELA, FermiLAT, and AMS latest results. Figure from [114].

In addition to astrophysical sources, the recent ramp-up in particle accelerator energy at the Large Hadron Collider (LHC) make it possible to probe SUSY phase space. Evidence for SUSY has not yet been found at the LHC, but future results regarding dark matter remain highly anticipated.

The task of indirect detection of dark matter has been successful in identifying several anomalies that are, at best, difficult to reconcile with a consistent astrophysical and cosmological picture. Although many interesting phenomena are observed, they lead to a high degree of degeneracy in the theoretical parameter space. Therefore, indirect detection can not provide the final word on the nature of dark matter.

## 1.5 Direct Detection of WIMPs

The only way to uncover the true particle nature of dark matter is to provide evidence of its direct interaction with a detector medium that can not be explained by any other physical process with a very high confidence level. The task of direct observation is tremendous, considering the weakly interacting nature of the WIMP, the unprecedented sensitivities involved and the ultra-low background environments required to obtain a reasonable signal-to-noise ratio. However, direct detection will provide the necessary information to break many parameter degeneracies and solidify the theoretical mold in particle physics and cosmology.

Detection of WIMPs is possible, by definition, through their weak interaction with SM particles via the quantum mechanical property of spin or simply via mass. This is convenient since we can not build a detector out of non-SM species. In principle, the WIMP miracle, stated above, leads to an interaction cross-section between WIMPs and SM nuclei (*i.e.* quarks) that naturally has a value making it possible to observe scattering events directly. Also, according to the dark matter halo models, the Earth should be deeply embedded in the Milky Way’s halo, making it possible to observe an interaction with Earth-based detectors. There are many methods of identifying and quantifying a WIMP-nucleus scatter, discussed below, but ultimately the kinematics are identical. One detail immediately noticed is the difference between nuclei with an odd vs. even number of nucleons,  $A$ . A spin-dependent cross-section,  $\sigma_{SD}$  is not possible in a nucleus with even  $A$ , since the spins singularly cancel each other. For nuclei with odd  $A$ , spin-dependent interaction is possible, with a “collision” occurring between the WIMP and the un-paired nucleon. Target nuclei with  $A \lesssim 30$  benefit from relatively large spin dependent coupling, whereas heavier nuclei receive a much greater enhancement from spin-independent (scalar,  $\sigma_{SI}$ ) coupling proportional to

$A^2$ . The details of expected WIMP-nucleus scattering rates and some of the latest experimental results are discussed in the remainder of this section.

### 1.5.1 WIMP scattering kinematics

The formalism of WIMP-nucleus scattering kinematics begins by considering a stationary target in a surrounding cloud of WIMPs, roughly consistent with the Earth being embedded in a dark matter halo. The differential scattering rate, usually in units [events/kg/keV/day], is given by the equation [115]:

$$\frac{dR}{dE_R} = \frac{R_0}{E_0 r} e^{-E_R/E_0 r} \quad (1.47)$$

where  $E_R$  is the recoil energy,  $R$  is the event rate per unit mass,  $R_0$  is the total event rate,  $r$  is the kinematic factor  $4M_\chi M_N / (M_\chi + M_N)^2$  for WIMP mass  $M_\chi$  and target nucleus mass  $M_N$ , and  $E_0$  is the most probable WIMP kinetic energy ( $M_\chi v_0^2/2$ ) determined by Maxwell-Boltzmann statistics usually taken from the most probable velocity of the solar system in the Galaxy ( $v_0 \approx 220$  km/sec). This form of the differential event rate is useful in illustrating its smoothly varying and featureless nature. A more general form is required to treat the full set of parameters involved in a real scenario that accounts for moving targets and more precise scattering cross-section contributions. The more general form is given in integral form [116]:

$$\frac{dR}{dE_R} = \frac{\rho_0}{M_N M_\chi} \int_{v_{min}}^{\infty} v f(v) \frac{d\sigma_{WN}}{dE_R}(v, E_R) dv \quad (1.48)$$

where  $\rho_0$  is now explicitly the local WIMP density,  $\frac{d\sigma_{WN}}{dE_R}(v, E_R)$  is the differential WIMP-nucleus scattering cross-section,  $f(v)$  is the WIMP speed distribution in the detector frame and  $v_{min} = \sqrt{M_N E_R / (2\mu_N^2)}$  corresponding to the WIMP speed resulting in recoil energy  $E_R$  with  $\mu_N = M_\chi M_N / (M_\chi + M_N)$ . The total event rate is found



by integrating over the velocities shown and over the energy range  $E_R = (E_t, \infty)$ , where  $E_t$  is the threshold energy set by the chosen detector medium and technology. We hold off integration for the moment, because Eq. 1.48 is not quite the whole story in that it only applies to the case of zero momentum transfer ( $q = 0$ ). In order to account for non-zero momentum transfer and the loss of coherence, the differential cross-section can be written in terms of the zero momentum case ( $\sigma_0$ ) and an additional nuclear form factor  $F(E_R)$  [116]:

$$\frac{d\sigma_{WN}}{dE_R} = \frac{M_N}{2\mu_N^2 v^2} (\sigma_0^{SI} F_{SI}^2(E_R) + \sigma_0^{SD} F_{SD}^2(E_R)) \quad (1.49)$$

The form factor can be expressed in many ways, depending on the scattering model used (*e.g.* thin shell, solid sphere, etc.). The SD form factor gets quite complicated [117], but the SI form factor can be expressed more simply by the Helm treatment, for example [118]:

$$F(E_R) = \frac{3j_1(qr_0)}{qr_0} e^{-q^2 s^2/2} \quad (1.50)$$

where  $j_1$  is a spherical Bessel function,  $q = \sqrt{2M_N E_R}$ ,  $r_0 = s\sqrt{1.44M_N^{2/3} - 5}$  and  $s$  is the “skin thickness” (1 fm = 5.07 GeV<sup>-1</sup>).

We are now equipped to write down the full representation of the differential scattering rate. The mathematical details are worked out in several places [103, 115, 119], but a useful, computation friendly representation (with  $c \neq 1$  units explicitly shown below for clarity) is:

$$\begin{aligned} \frac{dR}{dE_R} = \frac{N_T \rho_0 \sigma_0 c^2}{M_\chi^2 r v_E} F^2(E_R) & \left[ \text{erf} \left( \sqrt{\frac{3}{2}} \frac{v_{min} + v_E}{\bar{v}} \right) \right. \\ & \left. - \text{erf} \left( \sqrt{\frac{3}{2}} \frac{v_{min} - v_E}{\bar{v}} \right) \right] \end{aligned} \quad (1.51)$$

where  $N_T \equiv (\# \text{ of target nuclei}) / (\text{kg target}) = (6.022 \times 10^{26})/A$ ,  $\rho_0 \approx 0.3 \text{ GeV } c^{-2} \text{ cm}^{-3}$ ,  $c$  is the speed of light,  $v_E$  is the Earth velocity and other parameters are as stated above, with the exception of  $\sigma_0$ , which is the SI WIMP-nucleon cross-section (not the WIMP-nucleus version from above). Here, it is useful to write down the WIMP-nucleon cross-section in terms of the separate contributions from protons  $g_p$  and neutrons  $g_n$ :

$$\sigma_0 = \frac{4\mu_N^2}{\pi} [Zg_p + (A - Z)g_n]^2 \quad (1.52)$$

It is clear that if we assume that neutrons and protons contribute roughly equal amounts to the SI scattering process ( $g_p \approx g_n$ ), then the SI cross-section scales as  $A^2$ , as expected.

This sort of mathematical treatment is fairly standard in direct detection experiments, with the difference in the fine details causing minor changes in the results. We use this formalism in the next section to discuss the various schemes employed to capture the elusive WIMP in the laboratory.

### 1.5.2 Direct detection schemes

We now proceed with the mathematical tools needed to examine the variety of WIMP direct detection schemes. The experimental landscape is vast and thriving, driven as much by scientific rigor as by the artistic imagination of the experimenter.

A first stab at a reasonable set of assumptions can be made from cosmological and galactic arguments, suggesting WIMP masses in the range  $10 - 1000 \text{ GeV}/c^2$ . The rule-of-thumb provided by Eq. 1.47 suggests that recoil energies in the range of  $\sim 1 - 100 \text{ keV}$  should be possible using a wide variety of chemical elements as detector media [115]. The actual nuclear recoil energy measured in any detector

comes from the WIMP-nucleus elastic scattering, illustrated by the equation:

$$E_R(\theta) \approx 2E_\chi \frac{M_\chi M_N}{(M_\chi + M_N)^2} [1 - \cos(\theta)] \quad (1.53)$$

where  $\theta$  is the scattering angle and  $E_\chi$  is the kinetic energy of the WIMP. A summary of maximum nuclear recoil energies,  $E_{R,\max} = E_R(180^\circ)$ , is shown in Fig. 1.18 for typical target nuclei and various WIMP masses. It is clear that the best kinematic

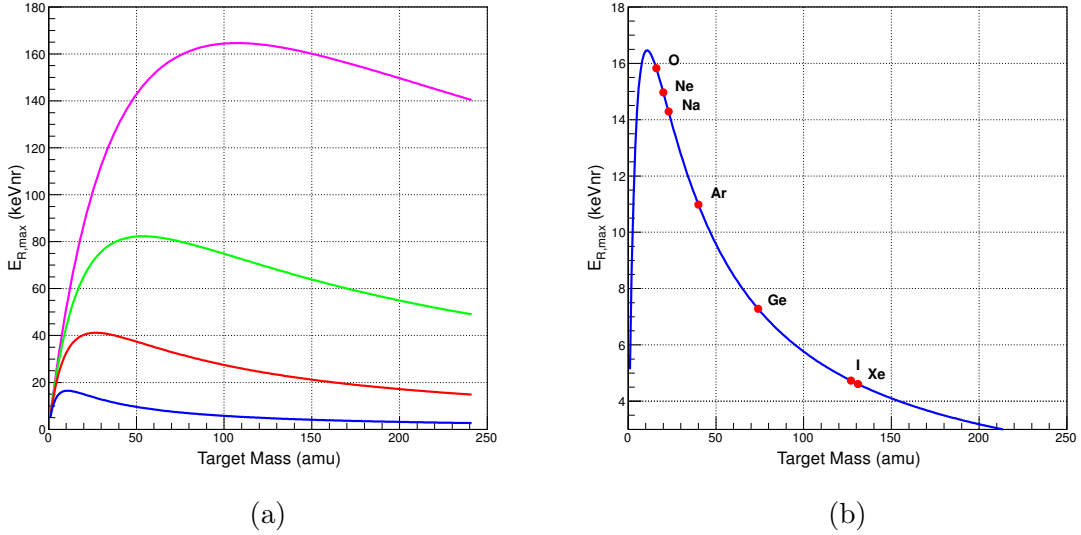


Figure 1.18: (a) shows the maximum nuclear recoil energy  $E_{R,\max}$  from a WIMP-nucleus elastic scatter as a function of target nucleus mass for WIMP masses of 100 (magenta), 50 (green), 25 (red) and 10  $\text{GeV}/c^2$  (blue). (b) shows  $E_{R,\max}$  for a 10  $\text{GeV}/c^2$  WIMP (solid curve) with the commonly used target nuclei labeled.

match for WIMP-nucleus elastic scattering occurs when  $M_\chi = M_N$  shown by the peaks in Fig. 1.18a. In choosing a target medium one also has to consider the trade-off between higher detection rates via the  $\sigma_0 \propto A^2$  enhancement with heavier nuclei

at lower energies and the cost of lower available recoil energies from the resulting kinematics. Two examples of the expected differential rates are shown in Fig. 1.19 for a typical set of parameters and WIMP masses  $M_\chi = 30$  and  $100 \text{ GeV}/c^2$ .

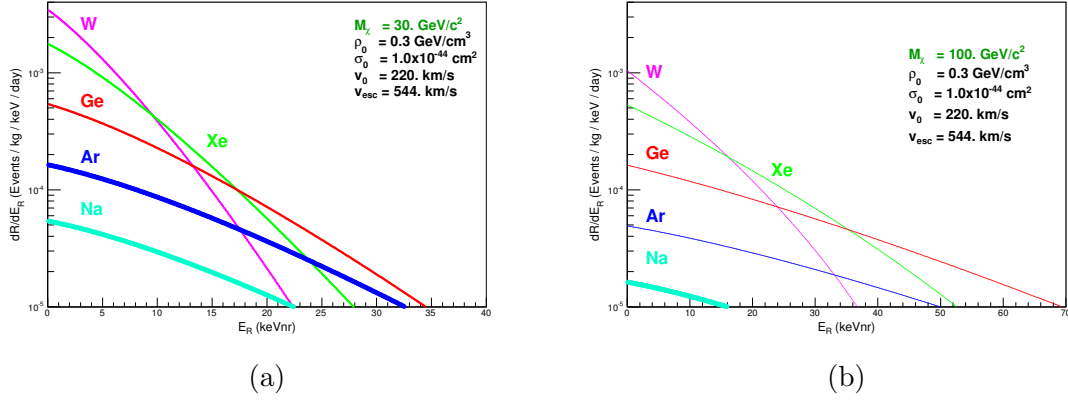


Figure 1.19: (a) shows differential event rates ( $dR/dE_R$ ) as a function of nuclear recoil energy ( $E_R$ ) for common target nuclei using input parameters from the recent LUX result [120] and a WIMP mass  $M_\chi = 30 \text{ GeV}/c^2$ . (b) is a similar plot, but with  $M_\chi = 100 \text{ GeV}/c^2$ .

These calculations assume a background-free, threshold-free environment and drive the sort of zeroth order choice of an appropriate target nucleus, optimized by the desired parameter space to be explored. There are many forms of radioactive backgrounds that can deposit energy alongside the WIMP collision and effectively bury the WIMP signal in the noise of a broad energy spectrum. Backgrounds come in the form of radioactive impurities in the detector materials and surrounding structures as well as from high energy cosmic rays. Strict material controls minimize some of the backgrounds and detailed assays allow for precise mapping of the expected background spectrum. In order to escape the high energy muons and subsequent

neutron flux from cosmic rays, detectors are operated deep underground, with the surrounding rock acting as a passive shield. A summary of the underground labs is shown in Fig. 1.20, where the effective cosmic ray shielding is compared to an equivalent water depth.

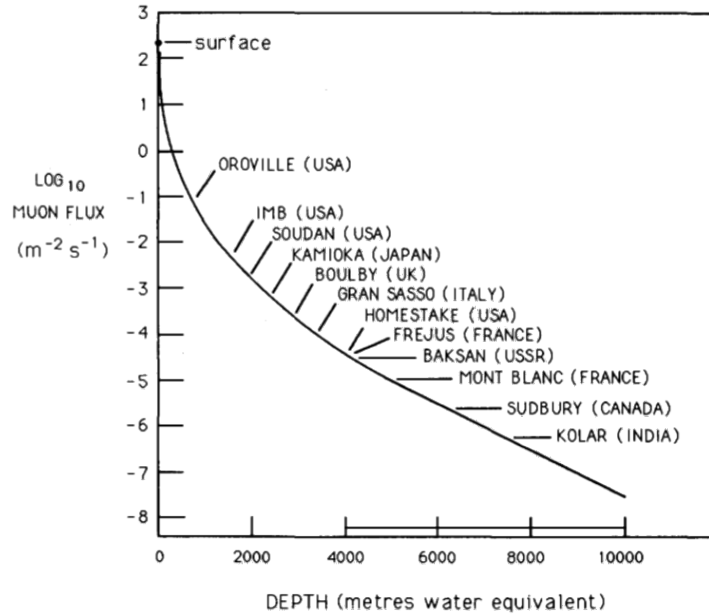


Figure 1.20: Approximate muon flux as a function of depth in underground labs used for low-background experiments. Figure from [121].

Given that the backgrounds are minimized as much as possible, the choice of a specific detector technology is driven by the action that takes place immediately after an initial WIMP-nucleus collision. As the nucleus recoils, it deposits its kinetic energy in the surrounding detector medium, leaving behind a trail of heat, excited atoms and excess charge. Detector technology has advanced sufficiently to include the collection of the resulting phonons, scintillation light, charge or a combination of

these within a single detector setup. This is illustrated graphically in Fig. 1.21, which

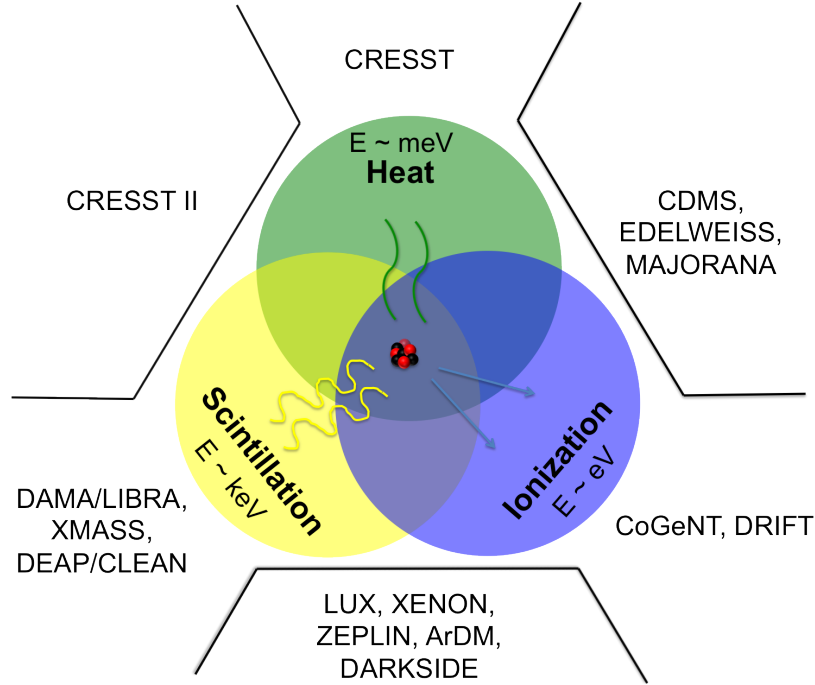


Figure 1.21: Graphical summary of several named collaborations in the direct search for dark matter and detection scheme employed. The energies labeled indicate an approximate low energy threshold for the associated energy deposition channel.

shows several named collaborations, along with the associated energy channel(s) and approximate energy threshold. For example, the CRESST experiment was capable of detecting a heat signal only, and detector upgrades made it possible for CRESST II to read out the phonons and scintillation light simultaneously.

The primary goal of any rare event search is to observe a signal that is  $5\sigma$  above background in order to claim discovery of something new in physics. However, the overall success of a WIMP search is not necessarily defined as such. The information

from null results still motivates theoretical pathways and improves our understanding of Nature. To date, all direct detection efforts have produced only null results within the “mainstream” of physics. This is not to say that all efforts have come up empty handed. The next section discusses several anomalies that have been seen across a variety of detection schemes.

### 1.5.3 Signal hints and the case for low mass WIMPs

The latest results from the DAMA/LIBRA group present over a decade of data from ultra-pure NaI(Tl) arrays located in the Gran Sasso National Laboratory (LNGS) in Italy. The data shows an excess of low energy events (2-6 keV recoil energy), as well as a peculiar annual modulation exhibited by a cosine behavior of only the low energy signal, with a period of  $0.999 \pm 0.002$  yr [124, 122, 123]. (See Fig. 1.22.) The signal and annual modulation ( $8.9\sigma$  C.L.) are consistent with the Earth passing

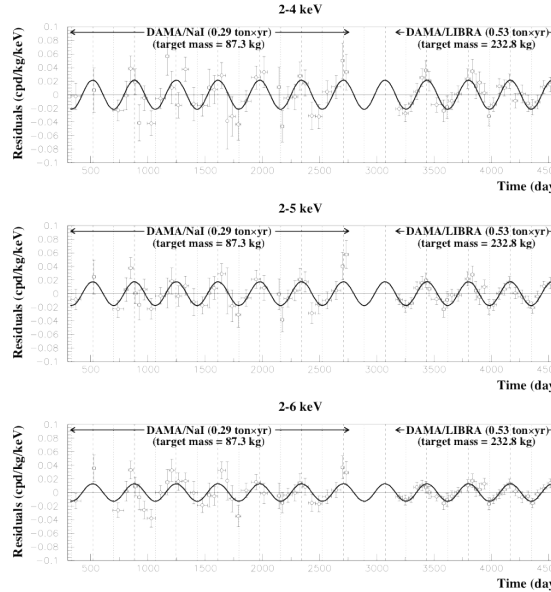


Figure 1.22: Low energy signal in DAMA/NaI and DAMA/LIBRA showing annual modulation during several years of running. Figure from [124].

through a local region of a galactic halo of low mass WIMPs. The modulation can be explained by the difference in the Earth's velocity relative to the galactic halo, which can be approximated by  $v_E \approx 244 + 15 \sin(2\pi t)$ , where  $0 < t < 12$  is the time in months since March.

In 2008 and 2010, the CoGeNT collaboration cautiously reinforced the DAMA/LIBRA result by reporting both an excess of low energy events and an annual modulation in its p-type point contact high-purity germanium detectors located in the Soudan Underground Laboratory in Soudan, MN [125, 126]. One possibility accounting for some of the modulated signal is an atmospheric effect involving muons and radon in the underground. This hypothesis was tested in 2013 in the Soudan lab by the MINOS group. The group found its own modulated signal due to atmospheric muons and radon to be out of phase with the CoGeNT data at the  $3\sigma$  C.L., concluding that these atmospheric effects do not significantly contribute to the CoGeNT modulation [127]. The MINOS measurement gains additional strength because the data was taken at the same time and location as the CoGeNT running, making it a nearly one-to-one data comparison. A similar comparison has yet to be done with DAMA/LIBRA in LNGS.

In 2011, the CRESST-II collaboration released 730 kg-days of data revealing several events above expected backgrounds in the oxygen recoil band of its  $\text{CaWO}_4$  crystals located in LNGS [128]. (See Fig. 1.23). They performed two maximum likelihood analyses resulting in local parameter space maxima centered on WIMP masses of 11.6 and 25.3  $\text{GeV}/c^2$ .

Very recently, in April 2013, the CDMS-II group released 140.2 kg-days of running from its eight silicon detectors based in Soudan [130, 129]. After rigorous event selection and blind analysis, three WIMP candidate events emerged, consistent with a WIMP mass of 8.6  $\text{GeV}/c^2$ . (See Fig. 1.24).



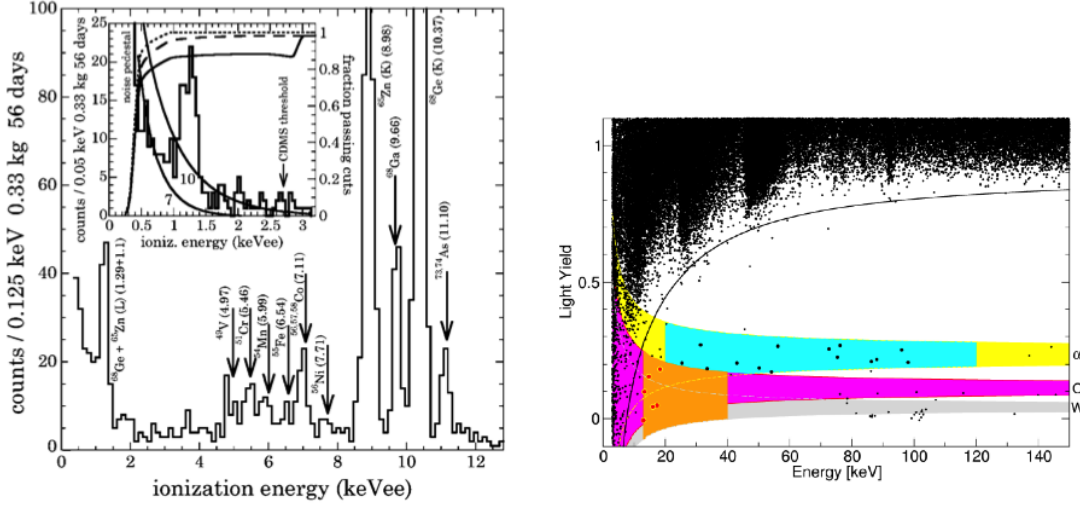


Figure 1.23: Low energy spectrum from CoGeNT (*left*) with projected exponentially rising signal due to a 7 GeV/ $c^2$  and 10 GeV/ $c^2$  WIMP overlaid (*left inset*). Arrows above the peaks indicate possible cosmogenic peaks and peaks with no arrows are L-shell EC peaks of  $^{65}\text{Zn}$  and  $^{68}\text{Ge}$ . (See [126] for original plot and full details). CRESST-II data (*right*) from one detector module (Ch20) showing light yield vs. energy. The orange highlighted portion is the WIMP acceptance region, showing 6 events in this channel. The other colored bands indicate expected  $\alpha$  backgrounds and the nuclear recoil regions of interest for the oxygen (O) and tungsten (W). (See [128] for original plot and full details).

The results of the searches are summarized in Fig. 1.25, which shows the current limits placed on the WIMP-nucleon SI cross-section ( $\sigma_{SI}$ ) as a function of WIMP mass ( $M_\chi$ ). The hints of low mass WIMPs seen by four independent collaborations using distinctly different detector technologies are indeed tantalizing. However, the most intriguing and disturbing feature of Fig. 1.25 is the fact that this parameter space has largely been excluded by XENON100, ZEPLIN-III and CDMS-II. The CDMS-II limits come from its high-purity germanium data released in 2010, including two dark matter candidate events. The probability that the events are due to expected background is 23%, so the result is not statistically significant, and thus places strong limits on the spin-independent cross section and WIMP mass [131]. The

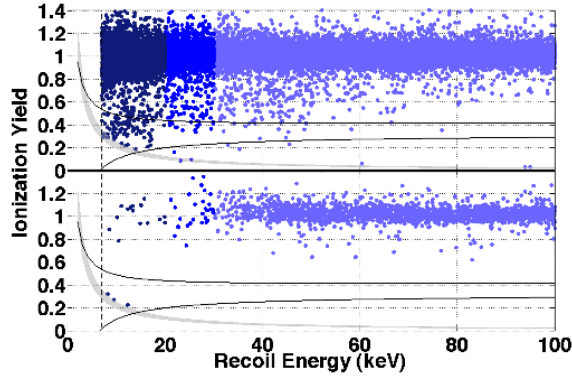


Figure 1.24: Ionization yield vs. recoil energy for CDMS-II silicon detectors before (*top*) and after (*bottom*) phonon timing cuts. The bottom plot shows the 3 dark matter candidate events in lower left-hand portion of the acceptance region outlined by the *black curves*. (See [130] for original plot and full details).

even stronger XENON100 limits come from 225 kg-days of running its two-phase liquid/gas xenon time projection chamber (TPC) in LNGS. It reported two dark matter candidate events with a 26.4% probability of being attributed to background [132]. This, like the CDMS-II germanium result, is not statistically significant, but adds to the excitement and intrigue of the WIMP search. Adding further to the complexity and intrigue of the WIMP search, the Large Underground Xenon (LUX) experiment released a null result, shown in Fig. 1.26, from 85.3 live-days of running its two-phase xenon TPC in the Sanford Underground Research Facility (SURF) in Lead, SD. This data places the strongest limits on  $\sigma_{SI}$  and  $M_\chi$  to date.

Although an enormous portion of the cross-section/WIMP mass phase space is excluded, the hints of signals in the low mass region beg further experimental investigation. The possibility of future detection of low mass WIMPs is the primary motivation of this work.

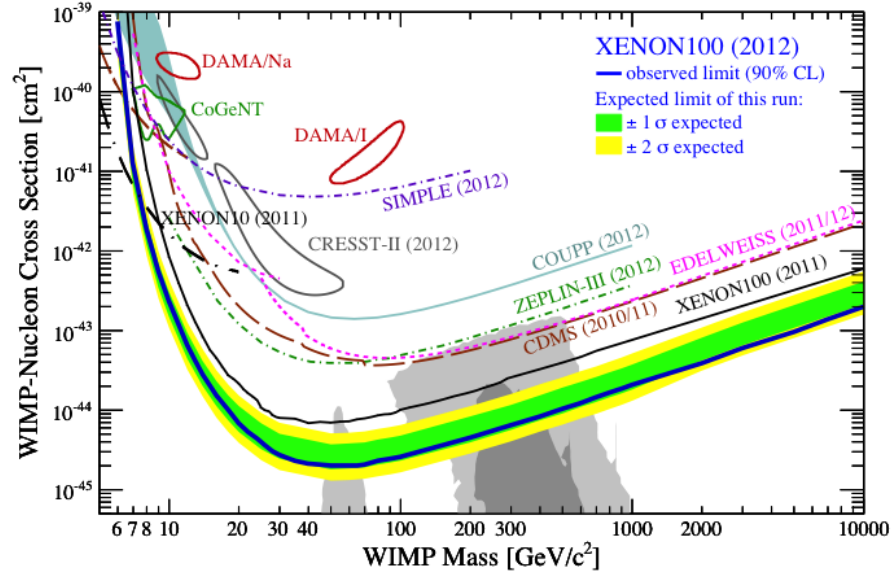


Figure 1.25: Summary plot of the limits on SI elastic WIMP-nucleon cross-section  $\sigma_{SI}$  as a function of  $M_\chi$ . The areas above the curves have been ruled out by the corresponding experiments. The colored contours indicate the phase space favored by the labeled groups, with the (*grey*) and (*light grey*) representing phase space favored by Constrained MSSM. (See [132] for original plot and full details).

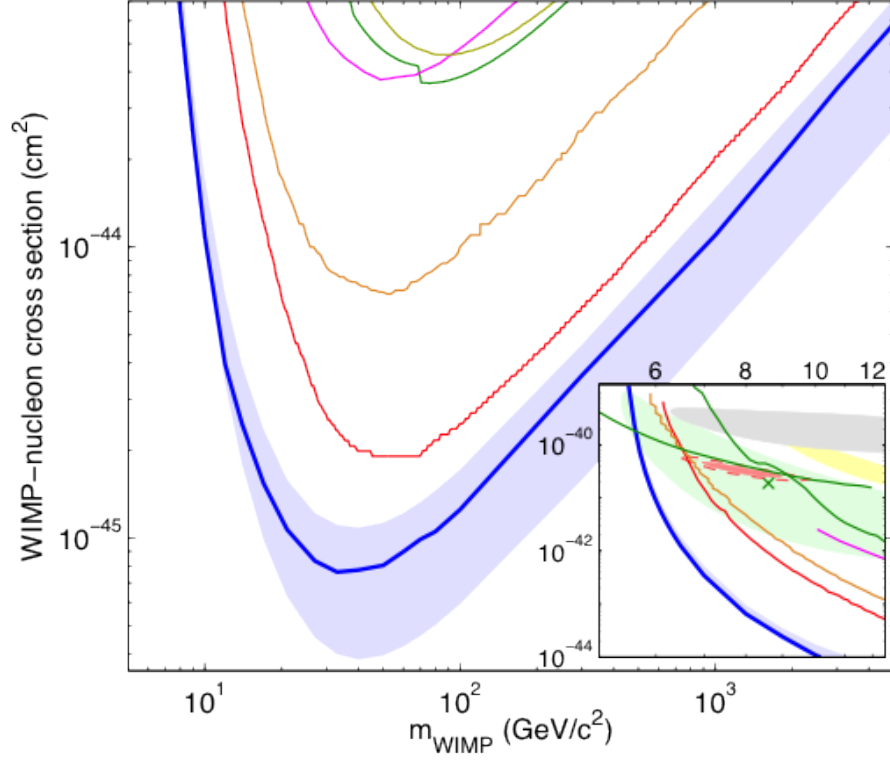


Figure 1.26: Summary plot of the SI elastic WIMP-nucleon cross-section  $\sigma_{SI}$  as a function of  $M_\chi$  with most recent LUX 90% C.L. (*blue curve*)  $\pm 1\sigma$ . Also shown are limits from Edelweiss II (*dark yellow curve*), CDMS II (*green curve*), ZEPLIN-III (*magenta curve*) and XENON100 100 live- day (*orange curve*), and 225 live-day (*red curve*) results. The inset (same axis units) focuses on low WIMP masses and includes the regions favored by CoGeNT (*light red contour*), CDMS II 95% allowed region (*green contour*) with centroid (*green X*), CDMS II low threshold analysis (*upper green curve*), 90% allowed region from CRESST II (*yellow contour*) and DAMA/LIBRA allowed region (*grey contour*). (See [120] and references therein for original plot and full details regarding individual results and interpretations).

## 2. LOW ENERGY NUCLEAR RECOILS

In this section, we explore the detailed physics of the different energy depositions (*i.e.* electron recoils vs. nuclear recoils) relevant to dark matter direct detection. We discuss the microscopic features of WIMP-like (nuclear recoil) and non-WIMP-like (electron recoil) interactions with respect to the different stopping powers involved. This was studied in detail by J. Lindhard *et al.* over 60 years ago and is characterized by an overall quenching of the total (true) energy deposition of a recoiling nucleus when compared to electron recoils [133, 134, 135]. We break down these types of interactions into different energy dissipation channels and discuss how each channel’s response to a nuclear (vs. electron) recoil changes with energy. A fundamental understanding of the energy itemization is required to reconstruct the true energy scale of all interactions in a detector, and separate the interesting signals from the background. In the case of a signal above background, the energy scale is used to calculate the WIMP mass and WIMP-nucleon cross section in conjunction with a best fit of cosmological parameters. This understanding is exceedingly important for the extremely low energy thresholds required to detect low mass WIMPs. The first section in this chapter is meant to develop a fairly general understanding of how a true energy scale is set in any detector. Later sections focus on the various energy depositions and dissipations in various dark matter direct detection media. We narrow this down to xenon TPCs and attempt to provide the necessary theoretical preliminaries for motivating the results of this work in gaseous xenon.

### 2.1 Setting the “True” Energy Scale

We saw in Sec. 1.5.1, that the true recoil energy ( $E_R$ ) from a WIMP-nucleus elastic scatter enters the expected differential rate equation explicitly within the nuclear

form factor as well as being the dependent variable in the integration of the total detection rate. Computing the integral of Eq. 1.51 for various interpretations of  $E_R$  leads to complicated effects on the overall behavior of the integrand causing possible systematic uncertainties. The largest errors occur at the low energy limit of the integral, the threshold energy ( $E_t$ ), where the counting statistics of real signals is usually poor on top of exponentially rising backgrounds. This can lead to magnified errors at energies close to  $E_t$ . In general, these uncertainties are minimized by tremendous efforts to measure radioactive backgrounds and perform excruciatingly detailed Monte Carlo (MC) studies aimed at producing the most accurate background energy spectrum possible. Assuming an acceptable signal-to-noise ratio and maximally understood backgrounds, any signal above background is, at the very least, interesting. In order to go from interesting to groundbreaking, the location of any “bump(s)” within the true energy spectrum needs to be well-motivated and accurately reconstructed. Otherwise, statistical fluctuations of low-likelihood events into the signal region of interest can be misinterpreted.

A major part of setting the true energy scale is the real vs. ideal detector response to all energy depositions. These efficiencies are discussed in a later section. Here, we focus strictly on the physics of a recoiling nucleus and how different interpretations of its dynamics can lead to varying results. For example, consider a detector that relies on charge collection for calorimetry, and is sensitive enough to measure a single quantum of charge (one electron) with very high efficiency. Indeed this is close to an ideal situation, but even sensitivity to a single quantum of charge can be rendered useless if the underlying physics that led to its liberation is not understood. After all, there are generally three channels through which a recoiling nucleus dissipates its kinetic energy as it rattles around a detector, effectively cooling back down to thermal equilibrium. The three channels are manifested in the form of heat, scintillation, and

ionization. There is not yet a detection scheme that offers the ability to measure all three channels simultaneously. The best we can do so far is to cover two at once, relying on theoretical descriptions to infer the energy “missing” in the remaining channel. (See Fig. 1.21.)

Since we can not measure all three energy dissipation <sup>1</sup> channels at once, then the least we can do, experimentally, is understand to the maximum extent, the one or two that are being measured. In other words, we seek an accurate answer to the question (for the specific case of ionization), “How much charge do I expect to be liberated during a typical elastic scatter?” The same question needs to be answered for scintillation and heat in other regimes. This means calibrating a detector’s response to known energy sources. In practice, dark matter detectors are calibrated with small, commercially available radioactive isotopes. This is because the complete experimental apparatus usually involves complicated cryogenics and a complex array of active and/or passive shielding operating deep underground. As a result, the calibration must be done *in situ*, involving portable radioactive isotopes placed near the detector externally or short-lived isotopes injected internally. Ideally, the calibration runs would be performed with a monochromatic beam of neutrons at precision-tuned energies, since the neutron’s collision with a target nucleus mimics a WIMP-like interaction. Unfortunately, the operating environment precludes such measurements. Instead, a white neutron spectrum is used from relatively high energy (up to few MeV) commercially available neutron generators. The detector response is then mapped out with MC studies, but can be very inaccurate at low energies

---

<sup>1</sup>We continue to use “dissipation” of energy when talking about energy transfers subsequent to the main energy deposition that takes place during the elastic scatter. We want to make it clear that the energy actually measured in a detector results from secondary processes that occur after the elastic scattering has taken place. In other words, it is the kinetic energy of the recoiling nucleus, electron, etc. that is truly reconstructed and only through conservation of energy and momentum does this translate to the specific properties of the incident particle.

because the underlying physics encoded in the MC is still poorly understood. The standard way to pick out energies from a broad spectrum neutron source is to perform scattering measurements with a small demonstrator detector and an additional neutron counter to provide coincidence and time-of-flight (TOF) data. This method works well at relatively high energies, where the scattering angle is large. Large scattering angles allow for the demonstrator to be exposed to a high neutron flux with adequate shielding of the coincidence counter. At low energies, the scattering angle is very shallow, so it is very difficult to get a clean signal in a finite amount of time. Also, this scheme still relies on statistical matching of the reconstructed energy spectrum to the true energy, calculated from the geometry and timing. The method is not perfect, but constitutes the state-of-the-art until this work and future ones like it can prove otherwise.

Clearly, the name of the game in setting the true energy scale is finding an intense radioactive source, capable of delivering monochromatic energies. The obvious choice is to use gamma sources, which come in small, portable packages that are easily deployed externally, and offer very precise, discrete energy lines. The problem with gamma (or beta or alpha) sources is that the method of energy deposition is fundamentally different from a WIMP-like interaction. A WIMP couples to the quarks in the nucleus only, bypassing the electron cloud on its way to the nucleus. Gammas, betas and alphas couple strongly to the electrons surrounding the nucleus, either knocking some charge loose, exciting the atom, or some combination of both, thus motivating the terms “nuclear recoil” and “electron recoil” referred to above. This is illustrated graphically in Fig. 2.1. A nuclear-to-electron recoil comparison is not one-to-one. The difference is quantified by the distinct stopping powers ( $dE/dx$ ) of a recoiling nucleus vs. recoiling electron. These stopping powers and their effect on the measured signal is examined next.



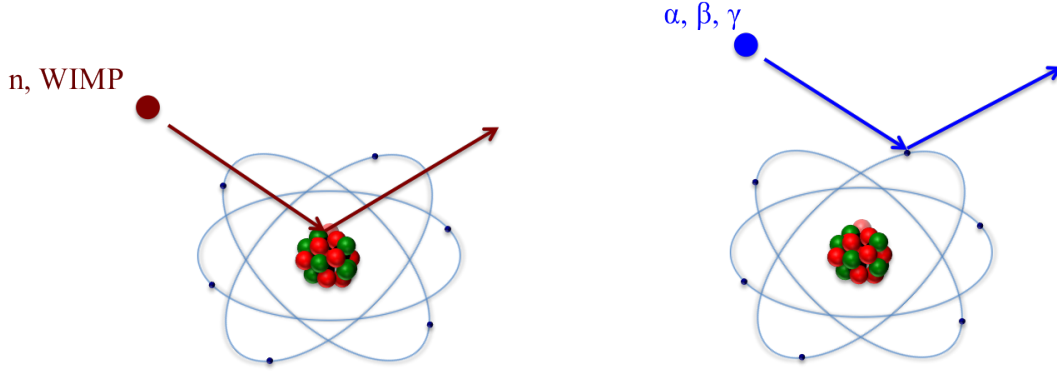


Figure 2.1: Illustration of a neutron or WIMP elastically scattering off a nucleus (*left*) and a gamma, beta or alpha interacting with the electrons (*right*).

## 2.2 Lindhard Theory

The seminal work on nuclear and electronic stopping powers was published in the 1960's by Lindhard *et al.* [133, 134, 135]. They developed a standard theoretical treatment of energy dissipation from the standpoint of atomic collisions with the surrounding medium. The general formulation is applicable to virtually any incident particle ( $Z_1, A_1$ ) in any medium ( $Z_2, A_2$ ), but here we focus on the case of an atom recoiling in a homogeneous medium of the same species ( $Z_1 = Z_2$ ), ( $A_1 = A_2$ ). This is the most common case for direct dark matter search via WIMP-nucleus elastic scattering, for example Xe in Xe, Ar in Ar, Ge in Ge and Si in Si. The theory can be extended to include non-monatomic configurations such as inorganic scintillators or Penning mixtures, but only differs in the inhomogeneous solution of a set of integral equations. The quantum mechanical many-body collisional physics is the same.

First consider an electron or gamma ray interacting with pure xenon gas. Gamma ray processes are generally characterized by the photoelectric effect, Compton scattering and pair production. These processes can be viewed as wholly electronic in

nature<sup>2</sup>, leading to the liberation of charge or excitation of atomic electrons and subsequent release of x-rays, scintillation photons, etc. Similarly for electrons, the interaction occurs in electron-electron processes, leading again, to ionization and excitation. There is a negligible amount of momentum transfer to the atomic nuclei that results in atomic motion from either electrons or gammas. Thus, ionization and scintillation occur with essentially 100% efficiency for incident electrons or gammas, and xenon TPCs are optimized to measure these signals with very high efficiency, whether using liquid xenon (LXe) or high pressure gas xenon (HPXe).

Now consider an elastically scattered xenon nucleus in xenon gas resulting from an incident neutron or WIMP, for example. The momentum transfer results in motion of the recoiling atom (we use this interchangeably with “recoiling nucleus”) with total energy  $E$ , which is dissipated by a number of subsequent collisions until the atom is thermalized. The atom can transfer its energy to either atomic electrons or other atomic nuclei.

Binary collisions with other nuclei occur in the classical limit according to screened Rutherford scattering [133, 137]. This is referred to as “nuclear stopping”. A large amount of energy can be transferred during nuclear stopping due to kinematic matching in a homogeneous medium. These cascading nuclear collisions are largely manifested as heat, which is exploited well by solid semiconductors and other crystals, where phonon extraction is possible. In a noble liquid or gas however, this heat signature is not measurable and results in a large loss of “measurable” signal.

In order for a nuclear recoil to produce a measurable amount of ionization or primary scintillation in a xenon TPC, the recoiling atom must interact with the atomic electrons. This is referred to as “electronic stopping”. This process can be

---

<sup>2</sup>There are higher order effects of gamma ray scattering off atomic nuclei (*e.g.* Mössbauer effect) but lead to sub-eV nuclear recoil energies. [136]

rather inefficient at low energies ( $< \mathcal{O}(100)$  keV) when compared to nuclear stopping partly due to the kinetic mismatch between the large recoiling atom and the relatively small electron. Although a scattered electron can gain a fairly significant amount of kinetic energy, leading to its own cascade of secondary processes, this represents a tiny fractional loss of the recoiling atom's energy. The electronic stopping was first quantified by Lindhard *et al.* by considering a Thomas-Fermi statistical treatment of two interpenetrating electron clouds.

### 2.2.1 The Lindhard factor

The total energy transferred to a medium after an elastic scattering event can be written as:

$$E = \eta + \nu \quad (2.1)$$

where Lindhard *et al.* explicitly stated that  $\eta$  is “the sum total of energy given to electrons” and  $\nu$  “is the total energy given to atoms, excluding internal atomic excitation of atoms” [134]. The particular energy dissipation channels are shown for the case of xenon in Fig. 2.2.

Now, let us take a look at the fractional components of the two primary energy dissipation channels,  $1 = \eta/E + \nu/E$ , where we formally define the Lindhard factor ( $f_n$ ) as the fraction of a recoiling atom's kinetic energy given to the surrounding electrons:

$$f_n \equiv \frac{\eta(E_r)}{E_r} \quad (2.2)$$

where the  $E_r$  dependence of  $\eta$  is explicitly shown. It is most important to note that  $\eta$  (and hence  $f_n$ ) is not solely a measure of ionization, but rather the total energy (fraction of energy) given to electrons. This total electron energy is then broken down into ionization and excitation. Excitation leads to the creation of prompt scintillation

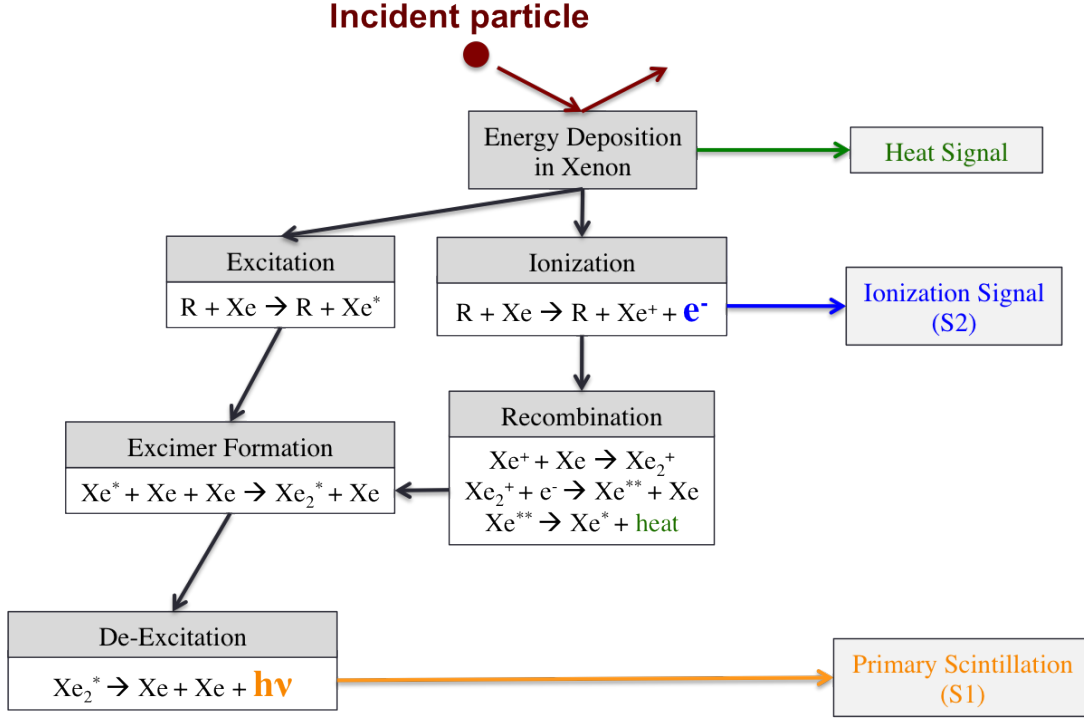


Figure 2.2: Block diagram representation of the energy dissipation channels in xenon and the resulting measurable signals in the form of heat, primary scintillation and ionization.

photons and ionization leads to escaping electrons, as well as additional scintillation due to recombination. This distinction is paramount, since both scintillation (S1) and ionization (S2) are measured simultaneously in a noble gas TPC. Following this reasoning and the work of [138] and [139],  $f_n$  can be expressed in terms of the total number of photons ( $n_\gamma$ ) and electrons ( $n_e$ ) measured:

$$E_r = \epsilon \left( \frac{n_\gamma + n_e}{f_n} \right) \quad (2.3)$$

where  $\epsilon$  is the average energy required to create a single quantum of energy in the form of an electron or photon. Obviously, for electron recoils depositing an energy  $E_{ee}$ , the Lindhard factor is one, so  $E_{ee} = \epsilon(n_\gamma + n_e)$ .

It is easily seen that an accurate calculation of  $\epsilon$  from simultaneous measurements of  $n_\gamma$  and  $n_e$  at a precise energy can be combined with nuclear recoil data to make the most accurate “true” determination of  $f_n$ . This represents the most powerful form of particle discrimination in a noble element TPC. Only with this form of  $f_n$  is it useful to talk about its precise mathematical form. Lindhard *et al.* expressed  $f_n$  as:

$$f_n = \frac{kg(\varepsilon)}{1 + kg(\varepsilon)} \quad (2.4)$$

where  $\varepsilon = 11.5E_r(\text{keV})Z^{-7/3}$  for a nucleus of atomic number  $Z$ ,  $k = 0.133Z^{2/3}A^{-1/2}$  and  $g(\varepsilon)$  is a fitted function (from [115])  $g(\varepsilon) = 3\varepsilon^{0.15} + 0.7\varepsilon^{0.6} + \varepsilon$ . A generic calculation for xenon leads to  $k = 0.166$ , regardless of the liquid or solid phase. This form of  $f_n$  is debated somewhat in LXe [137], mainly in the formulation of  $k$ , but very few attempts have been made to perform an actual combined S1, S2 analysis with little to moderate success [139, 140, 141, 142]. More work is required to fully endorse this model, especially in the gas phase, where no low energy data has been published.

### 2.2.2 Ionization yield in xenon

The simultaneous measurement of S1 and S2 at nuclear recoil energies  $\gtrsim 10$  keVnr in xenon does not present a significant challenge in modern detectors, which is fine for WIMP masses in the range of  $\gtrsim 20$  GeV/ $c^2$  or so. However, low mass WIMPs would produce a significant number of events at energies lower than  $\sim 10$  keVnr. This presents both a significant challenge, as well as an opportunity at the same time. It has been shown in LXe that the photon fraction, defined as  $n_\gamma/(n_\gamma + n_e)$  falls off, perhaps sharply, at recoil energies below  $\sim 10$  keVnr [139]. This is a challenge for schemes that rely on S1 to set the true energy scale, especially those that rely solely on S1 for particle detection [143, 144]. It is standard practice for LXe schemes to

extrapolate the results of the primary scintillation efficiency ( $\mathcal{L}_{eff}$ ) down to energies lower than existing nuclear recoil data sets in order to push the energy threshold (and subsequent dark matter limits) ever lower. This may be completely false in hindsight, since the sharply falling S1 at very low energies may indicate that the only result of dark matter search with any S1 requirement in this range leads to a null result, regardless of WIMP mass and cosmological parameters.

The opportunity lies in the behavior of the electron fraction, defined as  $n_e/(n_\gamma + n_e)$ , which has the potential to sharply rise at lower energies, unless thwarted by unknown nuclear quenching or threshold effects at very low energies. In a xenon TPC, this scheme corresponds to the S2-only detection regime, where no requirement for S1 is made. A few attempts have been made to use S2-only data in LXe on existing data sets (see Fig. 1.25 and associated references), but there have not yet been dedicated S2-only physics runs with reliable nuclear recoil calibration data at energies  $\lesssim 3$  keVnr.

The primary motivation of this work is to investigate the nuclear recoil response of xenon at very low energies using a scheme that is optimized for extremely low ionizing events. As shown in Fig. 1.19, the requirement for total mass in the active volume in a detector is somewhat relaxed for a detector optimized for low mass WIMPs. Therefore, we consider gaseous xenon, which presents the possibility of reduced cost and diminished technical challenge in terms of design, fabrication and operation. The compromise on the full scale must be made to operate at pressures as high as practicable to maximize the mass, but maintain the significant operational and cost advantage over cryogenic schemes.

To investigate the viability of this option, we built a small HPXe TPC with extremely high light collection efficiency, capable of very large electroluminescent (EL) gains. The goal was to demonstrate sensitivity to counting single electrons

in order to measure the specific ionization yield ( $Q_y$  in electrons/keVnr) of nuclear recoils to as low an energy as possible. The ionization yields could then be used to set the electron equivalent energy ( $E_{ee}$ ) scale of the nuclear recoils using the nuclear ionization quenching ( $\mathcal{Q}$ ), which is specific to only the ionization signal via:

$$E_{ee} = \mathcal{Q}E_r = Q_y W_{ion} E_r \quad (2.5)$$

where  $W_{ion}$  is the energy required to create one electron-ion pair in the HPXe. Knowledge of these parameters could then be used to convert the “visible” energy seen during a dark matter physics run to the true recoil energy produced by possible WIMP interactions. The downside to the S2-only regime is obviously the loss of the powerful S2/S1 ratio used to discriminate between electron and nuclear recoils in a TPC. The interesting thing is that at very low energies, as stated above, the S2/S1 discrimination technique may be rendered useless anyway.

The S2-only scheme represents somewhat of a departure from the Lindhard theory, in that it no longer requires specific knowledge of the true  $f_n$ , but rather the specific ionization yield ( $Q_y$ ) and nuclear ionization quenching ( $\mathcal{Q}$ ). This is still useful to the formulation of the Lindhard effects, since some information about primary scintillation may be available indirectly through careful study of its complementary relationship with the electron fraction.

### 3. EXPERIMENTAL SETUP

The nuclear recoil measurements for this work were carried out in a small high-pressure gaseous xenon (HPXe) time projection chamber (TPC) at the Texas A&M University (TAMU) Nuclear Science Center. The facility houses a 2UDH Pelletron accelerator, capable of producing precision-tuned proton energies up to 4 MeV. The accelerator and beam line components are optimized to produce very narrow proton energy bands directed at a thin LiF target mounted on a beam window at the end of the beam line. Nearly mono-energetic neutrons are produced in the forward direction via the  ${}^7\text{Li}(p, n){}^7\text{Be}$  reaction in the thin layer of Li. This narrow, well-known spread in neutron energy is the key to the accuracy and precision of the recoil measurement. Thus, a huge effort is spent on careful tuning and control of the proton beam and target in order to set the true energy scale and map the resulting detector response. The construction of the TPC, detector electronics, neutron beam and overall scattering setup are discussed in this section.

#### 3.1 Detector Construction

The detector was designed to achieve very high light collection efficiencies for both primary (S1) and secondary scintillation (S2) light. The resulting geometry is a very compact active region, attempting to mimic an integrating sphere with high optical transparency to the photosensors and high reflectivity of inactive parts. Some effort was made to minimize the non-instrumented volume of xenon, but this is not as important as in a liquid xenon (LXe) detector. The mean free path of neutrons in the HPXe is very long at the energies used here, so the probability of double scatters, resulting in neutron energy degradation is extremely low.



### 3.1.1 Physical layout of the TPC

The overall layout of the TPC consists of a parallel wire grid cathode, seven equally spaced field rings to provide the uniform drift region and two high-transparency crossed wire meshes acting as the gate and anode for the electroluminescent (EL) region. The active region is encased in plastic, which is rigidly mounted to a 10" diameter CF flange end cap and placed inside a 12" long thin-walled stainless steel (SS) cylindrical pressure vessel. The active region is centered in the vessel. A thin-walled SS radioactive source insertion tube enters the vessel from the opposing end cap and is located  $\sim 3$ " radially outward from the center of the detector.

The cathode consists of 0.004" diameter SS wires with 0.10" pitch, mounted under high tension on an Al frame, which is fixed to the end of a High Density Polyethylene (HDPE) cylinder. In order to maximize the light collection efficiency inside the active volume, a cubic geometry was used, which lead to interesting constraints on the field rings. The field rings are 0.01" diameter SS wires with 0.125" pitch, each wound around four HDPE quarter-cylinder wedges in precision machined grooves, such that the resulting profile is a four leaf clover pattern with the center of the clover defining the square profiled drift region. See Fig. 3.1. The ends of the field rings are brought together on the outside of one of the "clover leaves" and fixed to a set of screws. In this way, the field ring ends share the mounting point with the resistor chain allowing for all sharp edges to be joined together in a smooth ball of solder and captured between nuts. The resistors are 100 M $\Omega$  ( $\pm 1\%$ ) metal-oxide axial high voltage resistors from Vishay Dale [145] and are arranged to provide a linear voltage difference between the cathode (-500 V) and gate (+500 V). The gate and anode (+2750 V) grid planes are made by stretching the wire mesh over precision machined ridges on the face of a HDPE cylinder and clamping them in place with Al

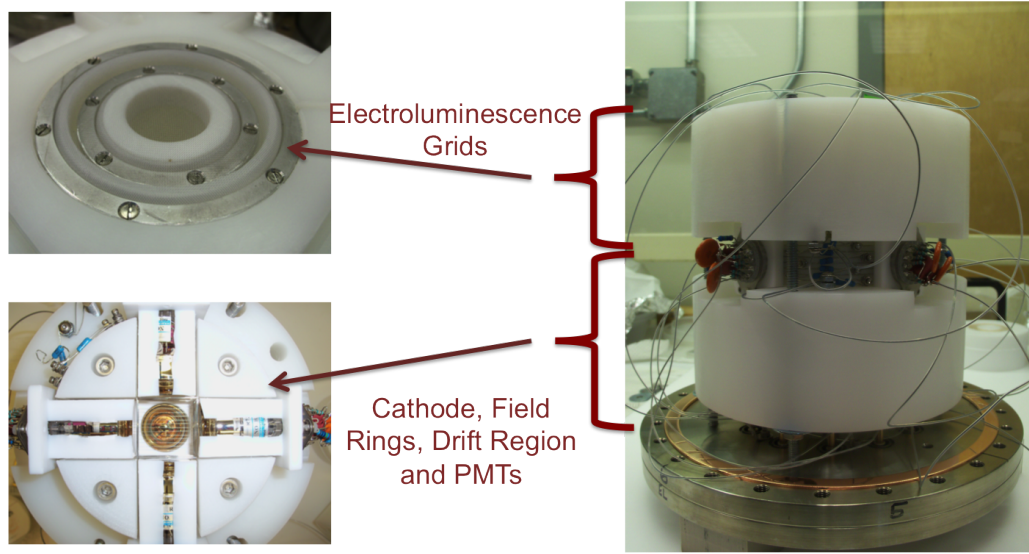


Figure 3.1: Photographs showing the TPC internal components. The *upper left* shows the EL grids with both (gate and anode) 88% open area meshes in place. The *lower left* shows a view looking into the drift region toward the cathode with the cathode, field rings, PMTs and reflective PTFE holders in place. The *right* photo shows a view of the fully assembled internals with all resistor chain and internal electronics and wiring in place.

rings. The spacing between the meshes defines the EL gap, which is fixed at 0.118" (3 mm). The mesh is a commercially available SS woven wire mesh from TWP, Inc. [146], with 0.0012" diameter wires at an average pitch of 0.02". The electrodes are summarized in Table 3.1, and the motivation for the actual voltage settings is discussed in a later section. Thus, the active region of the TPC contains a 1"  $\times$  1"  $\times$  1" cubic drift region, with an additional 0.118" EL gap. A cross-sectional drawing is shown in Fig. 3.2.

### 3.1.2 Cleaning protocol

There was no effort to use radio-pure materials in the detector, however, a high standard of cleanliness was maintained during construction. The standard protocol was to scrub (whenever possible) the machined parts first with tap water and deter-

Table 3.1: Summary of the TPC electrodes and the resulting optical transparency to normally incident light.

Electrode/Grid	Type	Wire Diameter (in)	Pitch (in)	Optical Transparency, Normal Incidence
Cathode	parallel wires	0.004	0.1	96%
Field Rings	parallel wires	0.010	0.125	92%
Gate	crossed wires	0.0012	0.02	88%
Anode	crossed wires	0.0012	0.02	88%

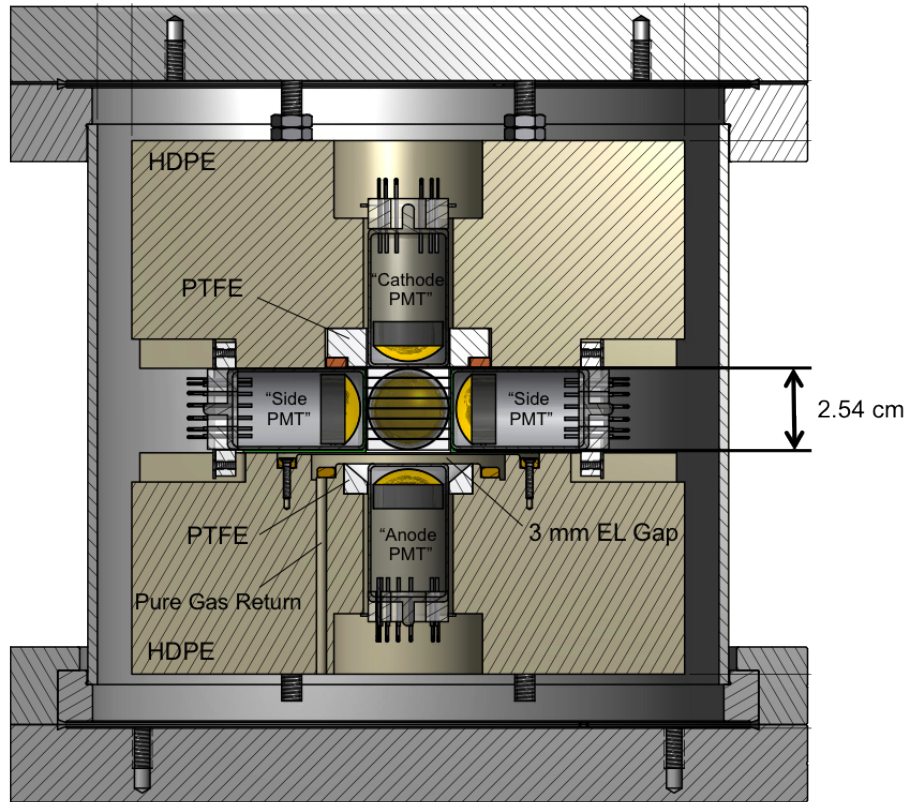


Figure 3.2: Cross-sectional schematic of the TPC and pressure vessel used in this work.

gent (Alconox). The parts were then rinsed with deionized (DI) water and placed in an ultrasonic Alconox + DI water bath for at least 30 min. The parts were again rinsed with DI water, then placed in an ultrasonic bath with DI water only. The

final cleaning step was an ultrasonic bath in pure isopropyl alcohol for at least 30 min. The parts were then air-dried and assembled in a laminar flow dust reduction environment.

### 3.1.3 Gas handling and purification

The pressure vessel is connected to the gas handling system, which includes a vacuum system and gas purification components. See Fig. 3.3. The gas purification

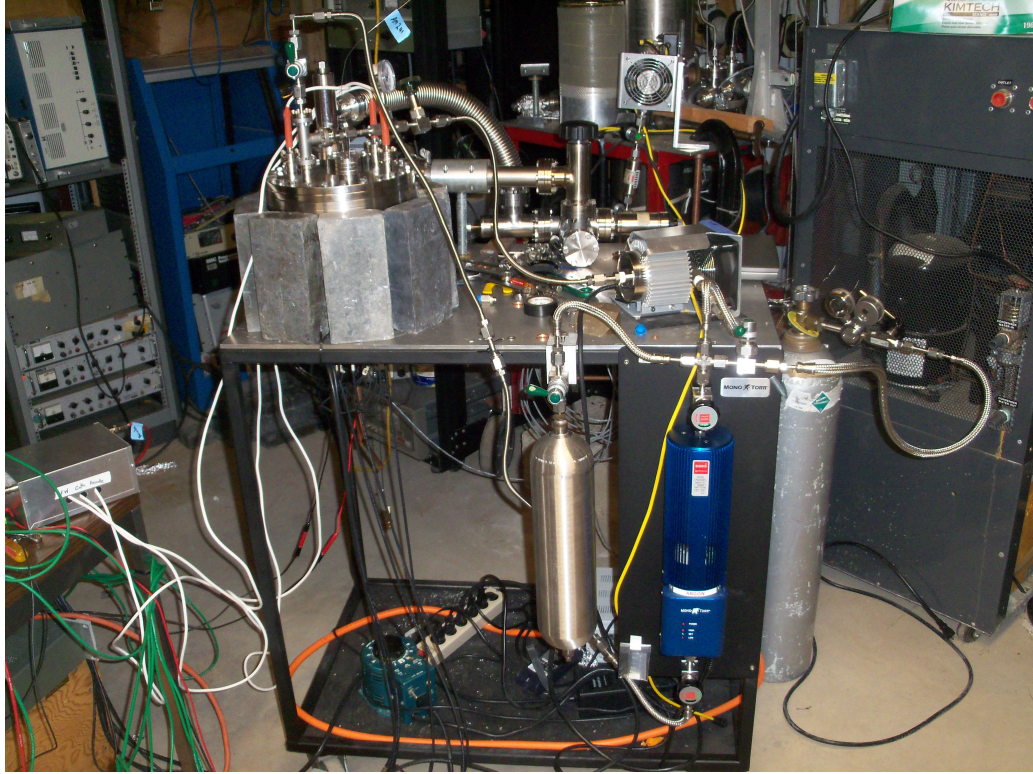


Figure 3.3: Picture of the complete experimental setup with the TPC surrounded by lead for background characterization. The electronics and DAQ are out of view to the left.

process was started by evacuating the system to a pressure  $\lesssim 10^{-5}$  torr while moni-

toring with a residual gas analyzer (RGA). After pumping for at least 24 hours with no leaks, the vacuum system was shut off and the xenon gas was introduced from the gas bottle to an operating pressure of 6 bar absolute. Prior to initiating gas flow through the SAES PS3-MT3-R heated purifier, a calibration run was taken with 60 keV gammas from an  $^{241}\text{Am}$  source to assess initial purity. Flow was commenced using a magnetically-driven, oil-free pump from PumpWorks, Inc. (Model PW2070) at a standard flow rate of 5 slpm at room temperature. The purity of the gas was monitored by taking periodic S1 and S2 sample data runs at nominal voltage settings, again with the  $^{241}\text{Am}$  source. The details are discussed below. Here, we only point out that a high state of purity was reached in minutes after the initial  $\sim 4$  hour purifier conditioning period.

The compact, nearly light-tight active xenon volume is well-isolated from the surrounding inactive gas. In order to ensure circulation of the active xenon, the gas returning from the purifier is ported directly into the EL region of the TPC via HDPE tubing. The gas was allowed to circulate for several weeks, while repairs were made to the accelerator and beam line components, prior to any nuclear recoil data runs. The system also includes a SS reclamation cylinder, where the xenon can be cryogenically pumped by submerging the cylinder in a  $\text{LN}_2$  bath.

#### *3.1.4 Photosensors*

The active HPXe is surrounded on all sides by 1" Hamamatsu R7378A photo-multiplier tubes (PMTs) embedded in the plastic, providing nearly  $4\pi$  geometrical solid angle coverage. The PMTs have a 10-stage multiplier in a fused silica body and were chosen because of their high pressure capability (up to  $\sim 20$  bar), small size and good spectral response over a wide range of wavelengths (160 nm - 650 nm). The quantum efficiency (QE) for unshifted xenon scintillation light ( $\sim 175$  nm) is

typically 10-15%. The PMTs are head-on type with a circular face, so the remaining dead space surrounding each PMT face is filled with PTFE plastic, making the active volume almost completely light-tight and highly reflective. Each PMT is set back from its closest TPC electrode by  $\sim 0.04''$  to minimize transient micro-arcs and glass scintillation from occurring on the fused silica faces between electrode boundaries [147]. The PMT photocathodes were operated at ground potential and a +HV anode, shown in the schematic in Fig. 3.4, which also contributes to better noise characteristics when operating near high voltage electrodes.

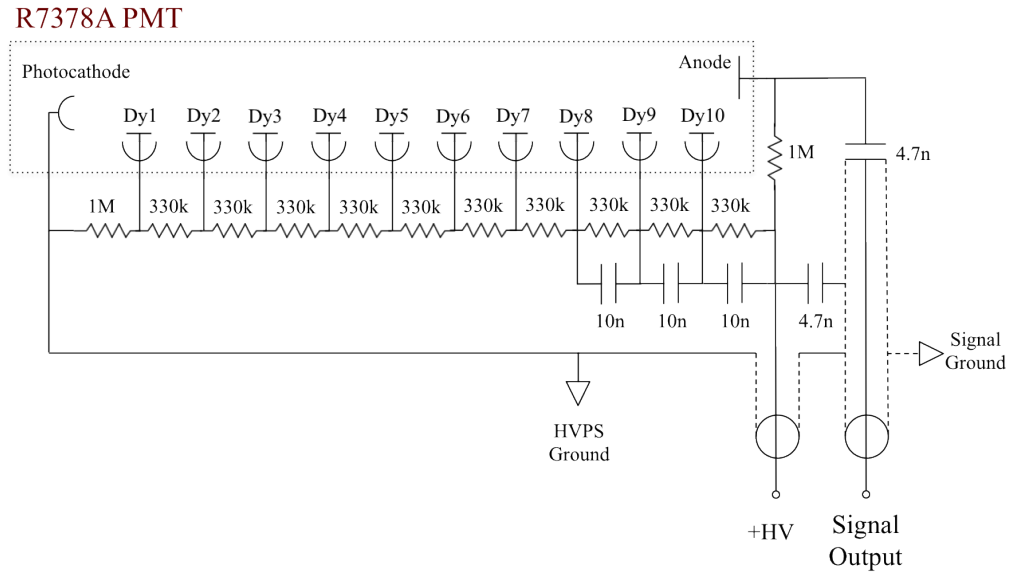


Figure 3.4: R7378A PMT base schematic for grounded photocathode operation with +HV on the PMT anode.



### 3.1.5 Electronics and signals

PMT signals from the four sides and the cathode-end were amplified ( $\times 10$ ) by a preamplifier (Phillips Scientific, Model 776), then fed into a discriminator (Phillips Scientific, Model 710), where the summed signals could be used as a hardware trigger for the 8-channel data acquisition (DAQ) system (Acqiris, Model DC265). The anode PMT signal was split before amplification. One of the anode PMT signal cables was sent through the preamp-discriminator-DAQ chain and the other un-amplified signal was read out directly by the DAQ in order to monitor possible pulse saturation due to the extremely high EL gain. See Fig. 3.5 for electronics layout.

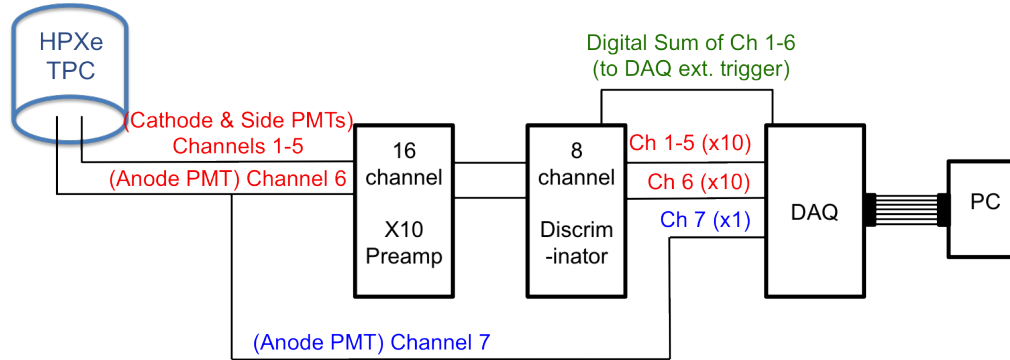


Figure 3.5: Block diagram of the electronics and signal chain. Channels 1-5 are  $\times 10$  amplified analog signals from the cathode and side PMTs. Channel 6 is a  $\times 10$  amplified analog signal from the anode PMT and Channel 7 is the un-amplified analog anode PMT signal. The discriminator's threshold was set to trigger on single photoelectrons. Any channel above threshold produced a 150 ns square wave and was sent to the summing circuit. The summed square waves were sent to the DAQ's external trigger input for S1 coincidence triggers. S2 triggers came from the Channel 6 raw  $\times 10$  signal.

At the DAQ, the PMT pulses were digitized at a frequency of 500 MHz, producing

digital waveforms with 2 ns binning. After every successful hardware trigger, the waveforms were read out by the acquisition software and assessed by a level two software trigger. (See Ch. 5 for trigger descriptions.) After passing all trigger criteria, a successful waveform was recorded and written to disk in binary format for offline processing and analysis.

### 3.2 Proton Beam at Texas A&M

The Texas A & M Nuclear Science Center is located in College Station, TX and is home to a 2UDH Pelletron accelerator (National Electrostatics Corp.) capable of producing up to 4 MeV charged particle beams. The charged beam begins at the Duoplasmatron ion source that injects  $H^-$  ions into the evacuated beam line. The  $H^-$  ions are initially accelerated to 22 keV and made into a focused parallel beam with the use of a magnetic field in the plasma, extractor plate and Einzel lens. The beam current is manually optimized upstream of the Pelletron accelerator by monitoring two Faraday cups and adjusting the source, an inflection magnet, a second Einzel lens and electrostatic X-Y steerers. A typical beam current at the accelerator entrance is  $\sim 2 - 6 \mu A$ , so it is referred to as a micro-beam. Inside the accelerator, the ions enter a linear electrostatic field produced by a set of field rings surrounding the beam line that vary in voltage from ground potential to the +HV terminal (variable up to 2 MV). The tank is filled with  $SF_6$  insulating gas to withstand the high voltages. At the +HV terminal position, the focused beam of  $H^-$  ions impacts a thin carbon foil ( $10 \pm 3 \mu g/cm^2$ ). The foil strips the electron from the  $H^-$  ions with almost zero change in proton momentum. The remaining protons undergo a second acceleration from the +HV terminal to ground potential via a second set of linearly graded field rings. Downstream of the accelerator, the proton beam is refocused with a set of quad magnets and bent  $30^\circ$  off the centerline axis



with a bending magnet (BM), also referred to as a switching magnet. Three sets of vertical slits limit the proton beam spread. The final set of slits is near the end of the beam pipe and provides a feedback signal to the accelerator control circuit. In manual control mode, the terminal potential (TP) can be adjusted by hand while monitoring the micro-beam current on the slits and two additional Faraday cups downstream of the BM. However, manual control relies on simultaneous adjustment of the BM and TP by the operator, suffering from imprecision and non-reproducibility from run to run. Instead, the feedback gain and slit width are adjusted to provide very stable, repeatable automatic proton energy control. This mode of operation allows us to change the field of the BM, while the control circuit automatically adjusts the TP (*i.e.* beam energy) to keep the beam centered on the slits to the nearest  $\pm 1$  keV. All nuclear recoil data runs were taken in automatic slit control mode with typical beam currents at the end window in the range 30 - 350 nA.

The Pelletron accelerator is shown in the photos in Fig. 3.7, as well as a block diagram of the major beam line components in Fig. 3.6.

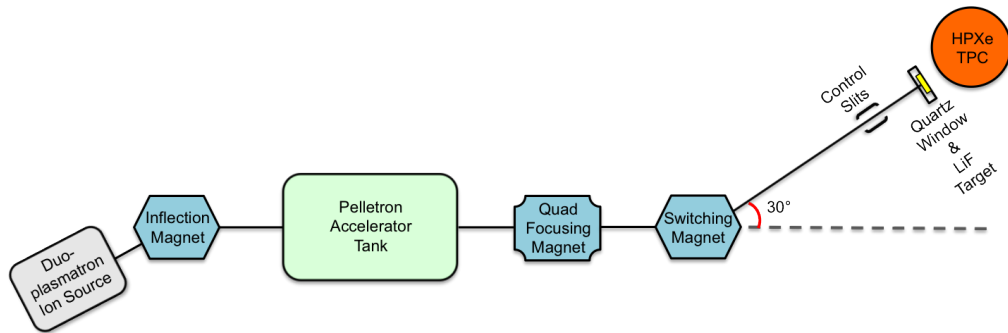


Figure 3.6: Block diagram of the Pelletron accelerator and major beam line components at the Texas A&M Nuclear Science Center.

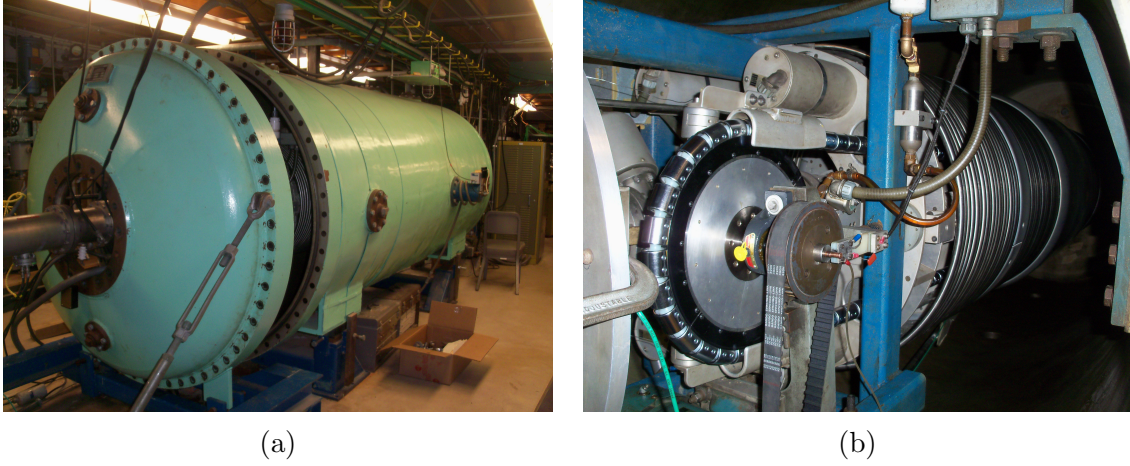


Figure 3.7: (a) and (b) show the Pelletron accelerator tank (opened for maintenance) and the internal structures respectively. The entire charging system was re-built prior to the actual nuclear recoil measurements.

### 3.3 Proton Beam Energy Calibration

The neutrons used in the scattering experiment are produced when the proton beam strikes a LiF target at the end of the beam pipe via the nuclear reaction  ${}^7\text{Li}(p, n){}^7\text{Be}$ . The LiF was vacuum deposited on a  $2'' \times 0.375'' \times 0.005''$  strip of Ta by Thin Film Labs in Milford, PA with a thickness corresponding to a 2 keV proton kinetic energy loss.

An accurate and precise knowledge of the incoming protons' kinetic energy is required to calculate the resulting neutron spectrum. The proton beam energy is set by the TP in the accelerator plus the initial 22 keV gained at the Duoplasmatron source. An approximate energy can be determined from just the voltage readout of the TP to the nearest  $\pm 10$  keV, but much higher accuracy is needed for this experiment. A more accurate indication of the energy is obtained from the BM and the electrodynamic calculation of the protons' response to the magnetic field.

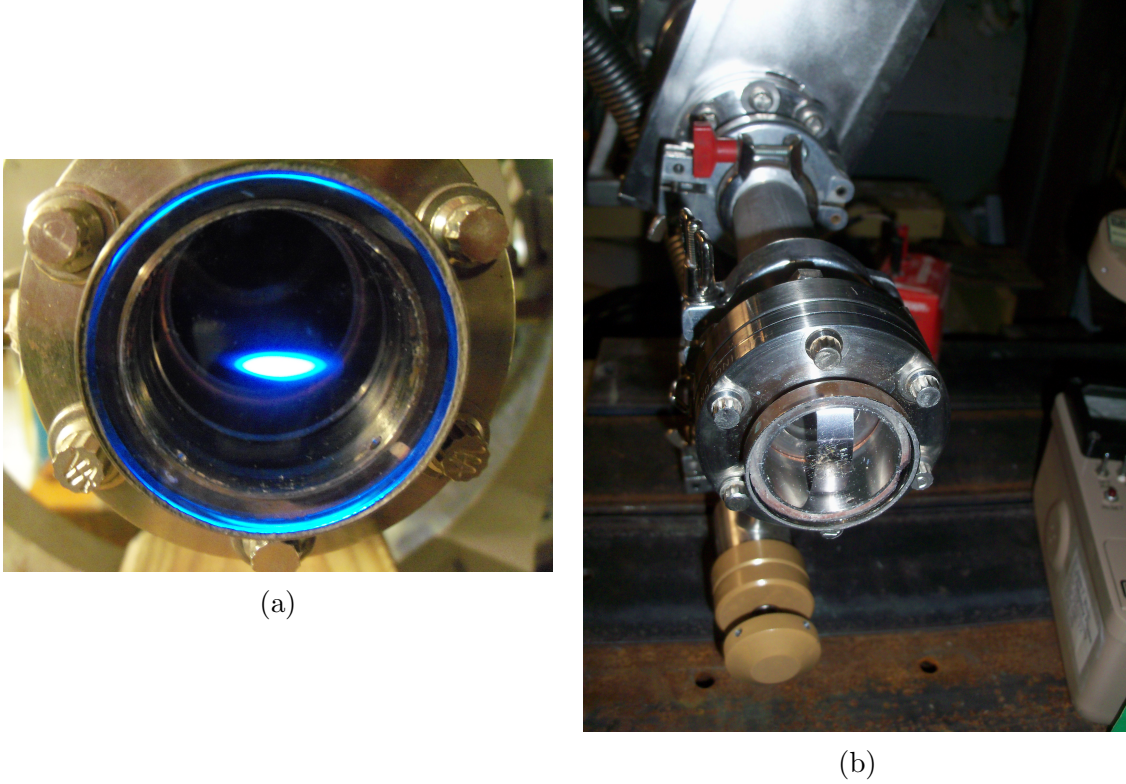


Figure 3.8: ( a) shows proton beam spot hitting the quartz window with no LiF target in place. ( b) shows the LiF coated Ta metal strip mounted on the beam window inside the evacuated beam pipe.

The absolute value of the field is measured directly to the nearest  $\pm 1\mu\text{T}$  using a high-precision, temperature compensated Hall probe (Model HTM81-0608-10-T) and Tesla meter (Model 8010) from F. W. Bell. The extremely stable BM is controlled by simply adjusting the current in the field windings. This accuracy and precision, combined with the automatic control mentioned in Sec. 3.2, allows for the ability to select proton energies with the turn of a knob using the following equation:

$$E_p(B) = \frac{qB^2(a^2 + d^2)^2}{8m_p d^2} \quad (3.1)$$

where  $q$  is the electronic charge of the proton,  $B$  is the value of BM magnetic field

transverse to the beam,  $m_p$  is the proton mass and  $a$  and  $d$  are the length and width of the BM field region respectively.

One caveat of using this method is that the exact geometry and flux density of the BM must be well-known over the entire path of the protons within the magnetic field. Unfortunately, the lack of as-built drawings and the tightly enclosed physical construction of the BM preclude accurate measurements of the necessary geometrical parameters. Instead, the BM field is measured at a fixed location immediately adjacent to the beam pipe and is calibrated to the energy of a well-known physical process. Subsequent changes in the energy are then calculated relative to the calibrated field value. This was the primary motivation of choosing a LiF target, which has a precise threshold energy for neutron production at  $E_t \approx 1.882$  MeV. See Sec. 4.1 for a more in depth discussion. This value has been established experimentally in the literature [148, 149]. Using the threshold energy as a standard calibration point, the geometrical factors in Eq. 3.1 can be parameterized and rolled into one term:

$$E_p(B) = \frac{qB^2 g(a, d)}{8m_p} \quad (3.2)$$

where  $g(a, d)$  is defined by:

$$g(a, d) \equiv \frac{(a^2 + d^2)^2}{d^2} \quad (3.3)$$

and determined from the threshold energy by:

$$g(a, d) = \frac{8m_p E_{p,th}}{qB_{th}^2} \quad (3.4)$$

Now, all the terms in Eq. 3.1 are known so that the proton energy can be calculated using the measured BM magnetic field value and the corresponding  $g(a, d)$  factor. In order to account for variations in operational conditions from run to run, the beam

energy was calibrated prior to each neutron data set.

The threshold of neutron production during calibration in the LiF was determined by monitoring a BF<sub>3</sub> proportional counter surrounded by polyethylene plastic placed directly downstream of the target. The Pelletron accelerator's automatic slit control was used, centering the protons in the beam pipe, while the BM current was turned up incrementally. The BM field and number of BF<sub>3</sub> counts were recorded for a fixed amount of time per field setting. The current was turned up until a sharp rise was observed in the number of BF<sub>3</sub> counts. At that point, the highest energy protons corresponding to  $E_{p,th}$  were just coming into contact with the edge of the LiF target, producing neutrons strictly in the forward direction in the lab frame. Lower energy protons (*i.e.*  $E_p < E_{p,th} = 1.882$  MeV) are impacting the LiF, but do not have sufficient energy to produce neutrons via the  ${}^7\text{Li}(p,n){}^7\text{Be}$  reaction. This particular calibration point allowed us to determine the highest energy protons in the beam and calculate the spread in the beam energy based on the LiF target width and thickness. Thus, we preserved the ability to measure and accurately determine the highest energy neutrons and resulting maximum backscatter nuclear recoils.

One thing to note here is that the calibration method is often done in reverse to what is described above. Usually, one starts at a BM setting corresponding to  $E_p > E_{th}$ , then turns the energy down until a sharp decrease in counts is observed in the BF<sub>3</sub> counter. The problem with that method is that the BM current control knob has some hysteresis, and it was immediately noticed that going from turning down the current to the turning up the current shifted the calibration point. As a result, the knob was always turned from low-to-high current during calibration and for the subsequent data run. If the desired energy was overshoot, then a new calibration point was determined and the energy for the data run re-tuned.

### 3.4 Nuclear Recoil Scattering Setup

The final setup for the nuclear recoil scattering measurements is shown in Fig. 3.9. Many other setups were attempted in order to optimize the measurement and minimize gamma backgrounds, including various other external shielding configurations. However, the gamma background was well-controlled with minimal to no additional lead shielding and neutrons outside the  $\sim 10^\circ$  acceptance cone were unlikely to scatter back into the chamber. Thus, this setup allows the highest energy neutrons to enter the active volume with extremely small energy spread with acceptable gamma backgrounds.

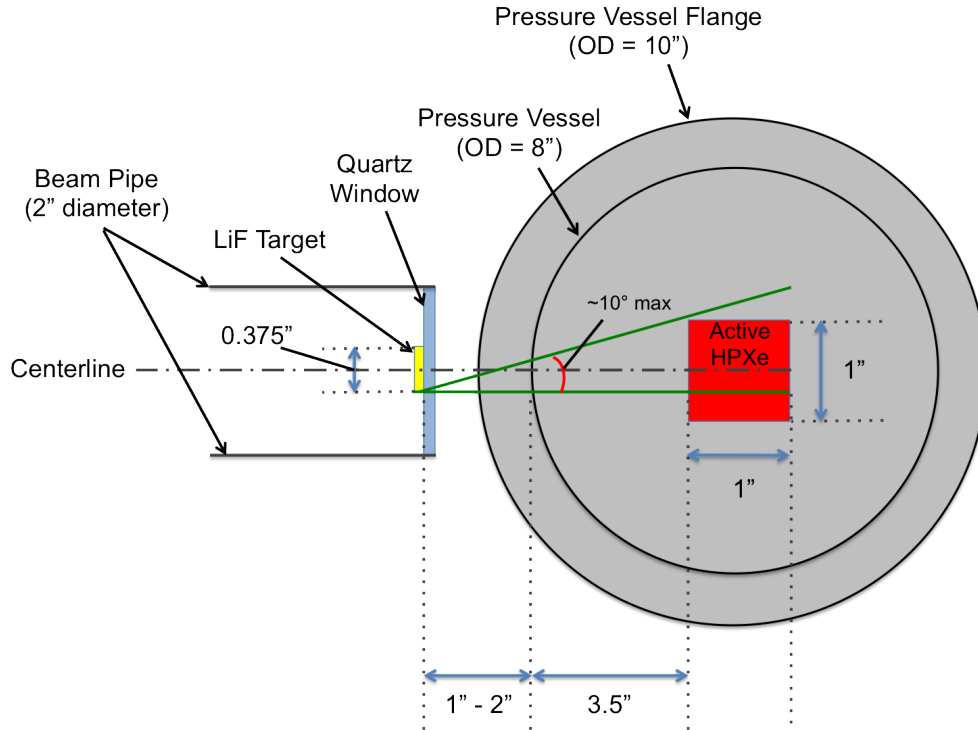


Figure 3.9: Scattering setup showing the beam pipe, quartz window, LiF target, pressure vessel and active volume of HPXe. A removable 1"  $\times$  2"  $\times$  3" lead block (not shown) was placed between the beam window and pressure vessel and used to characterize the gamma background from the LiF target. The lead was oriented such that it was centered on the beam window with the 1" thickness in the path of the beam.

## 4. SIMULATIONS

Several aspects of the detector and experimental setup were simulated. A realistic neutron spectrum was generated and used to optimize external shielding and characterize the neutron flux inside the active xenon volume. *Geant4* (Version 4.9.5) [150, 151] was used for Monte Carlo (MC) simulation of the neutron beam and to calculate the nuclear recoil kinematic response of the xenon. *Garfield* (Version 7.44) [152] with the *Magboltz* [153] and *Heed* [154] interfaces was used to determine the gas properties in the drift region, as well as the gain and possible secondary ionization in the EL region with electrostatic input from *COMSOL Multiphysics* (Version 4.3) [155]. A separate ray tracing program was written in *C++* to determine more accurate light collection properties based on the geometry and reflective properties of the TPC components. The details of the simulations are discussed in this section. The full analysis and results are presented in Ch. 5 and used to validate the nuclear recoil data.

### 4.1 Neutron Beam

A primary goal of this experiment was to produce a “beam” of mono-energetic neutrons using protons incident on a LiF target. There are several factors that contribute to the energy spread, which the final neutron beam simulation must account for, but let us first consider the target itself.

The 75 nm thick layer of LiF was vacuum deposited on a  $2'' \times 0.375'' \times 0.005''$  piece of Ta metal. An incident beam of protons interacts with the Li in the target via the nuclear reaction  ${}^7\text{Li} + p \rightarrow {}^7\text{Be} + n$ . The resulting neutron energy ( $E_n$ ) spectrum



can be calculated via simple nuclear reaction kinematics:

$$E_n = E_p \frac{m_p m_n}{(m_n + m_r)^2} \left\{ 2 \cos^2 \theta + \frac{m_r(m_r + m_n)}{m_p m_n} \left[ \frac{Q}{E_p} + \left( 1 - \frac{m_p}{m_r} \right) \right] \right. \\ \left. \pm 2 \cos \theta \sqrt{\cos^2 \theta + \frac{m_r(m_r + m_n)}{m_p m_n} \left[ \frac{Q}{E_p} + \left( 1 - \frac{m_p}{m_r} \right) \right]} \right\} \quad (4.1)$$

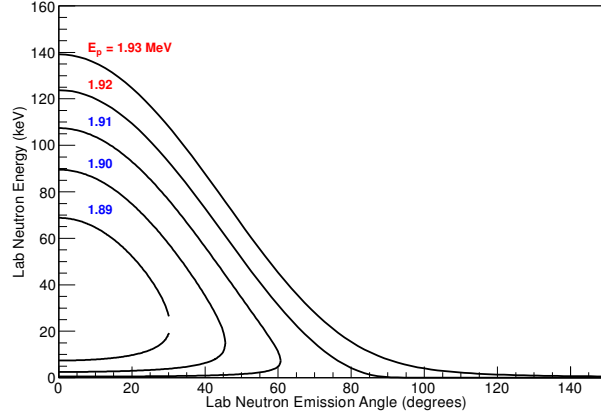
where  $E_p$  is the incident proton kinetic energy,  $m_p$  is the proton mass,  $m_n$  is the neutron mass,  $m_r$  is the residual  ${}^7\text{Be}$  nuclear mass,  $Q = (m_p + m_{\text{Li7}} - m_n - m_{\text{Be7}}) = -1.646$  MeV is the Q-value of the nuclear reaction, and  $\theta$  is the lab emission angle. The fact that the Q-value is negative indicates that the reaction is endothermic with a threshold energy ( $E_t$ ), below which the reaction does not take place. The threshold energy is calculated by setting the portion under the radical equal to zero and taking the minimum value ( $\theta = 0^\circ$ ):

$$E_t = \frac{-Q(m_r + m_n)}{m_r + m_n - m_p} \approx 1.882 \text{ MeV} \quad (4.2)$$

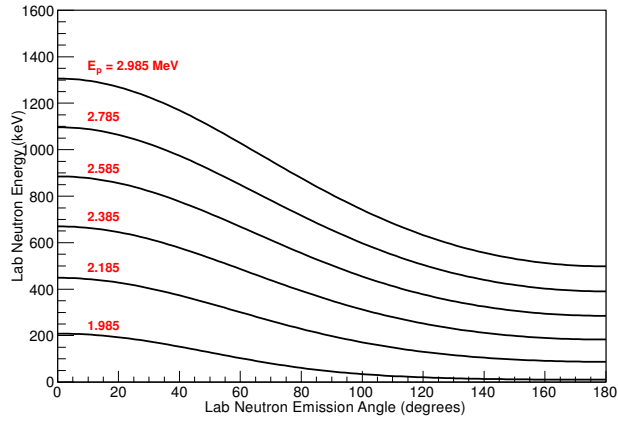
The other obvious feature of the neutron energy spectrum is that below a certain energy,  $E_n$  is double-valued. This can be understood by considering the conservation of momentum in the center-of-mass system. The result is that neutrons are produced strictly in the forward direction ( $0^\circ \leq \theta < 90^\circ$ ) in the lab frame from proton energies between  $E_t$  and an energy defined by  $E_p^*$ : (See [149].)

$$E_p^* = \frac{m_{\text{Be7}}(m_{\text{Be7}} + m_n - m_p)}{m_{\text{Be7}}(m_{\text{Be7}} + m_n - m_p) - m_p m_n} E_t \approx 1.92 \text{ MeV} \quad (4.3)$$

When the incident proton energy exceeds 1.92 MeV, neutrons are produced at all angles. Example spectra are shown in Fig. 4.1. If the LiF layer is thick enough, then for a given proton energy, neutrons are emitted at all energies and angles below



(a) Neutron energies (keV) as a function of emission angle (degrees) in the lab frame. Incident proton kinetic energies are shown for the double-valued (*blue*) and single-valued energy ranges (*red*).



(b) Neutron energies (keV) as a function of emission angle (degrees) in the lab frame with incident proton kinetic energies shown for the corresponding curves.

Figure 4.1: Neutron energies as a function of lab emission angle.

the corresponding curves in Fig. 4.1. For the double-valued energies, the neutron production region lies to the left of each curve. A thick target is one in which the incident protons are able to lose all their kinetic energy before emerging from the target. The target used in this work is extremely thin though, so the protons lose

only a fraction of their kinetic energy inside the LiF layer. The average proton kinetic energy lost in the 75 nm thick target is plotted in Fig. 4.2 for energies ranging from  $E_t$  to the highest energy in this work.

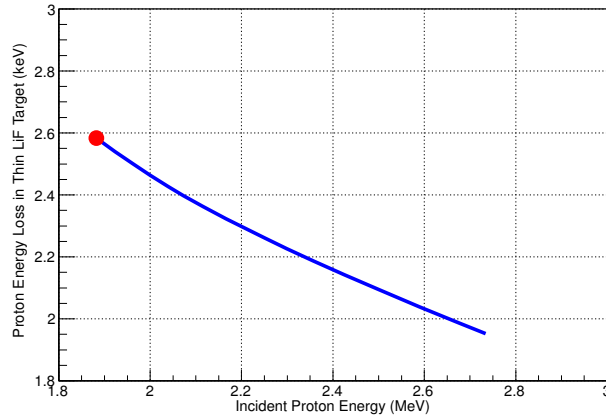


Figure 4.2: Proton energy loss in the 75 nm thick LiF target (keV) as a function of incident proton energy (MeV). The plot ranges from the threshold energy of 1.882 MeV (*red dot*) for the  ${}^7\text{Li}(p, n){}^7\text{Be}$  reaction to the highest proton energy used in the final data set (2.734 MeV). All proton stopping powers were taken from the NIST Pstar database [156].

Since the proton only loses  $\sim 2$  keV in the LiF target, then only a band of neutron energies is produced. On the full scale of angles, the 2 keV spread in beam energy is not visible. Fig. 4.3a thus shows part of the band of energies produced in the forward direction for the highest  $E_p$  used here ( $E_p = 2.734$  MeV). Fig. 4.3b shows the neutrons that travel directly into the active volume of xenon in the TPC or have a good chance of scattering off the HDPE and surrounding components back into the xenon with appreciable energy. These are considered to be within the geometric acceptance cone. The full spectrum of neutron energies and angles were generated

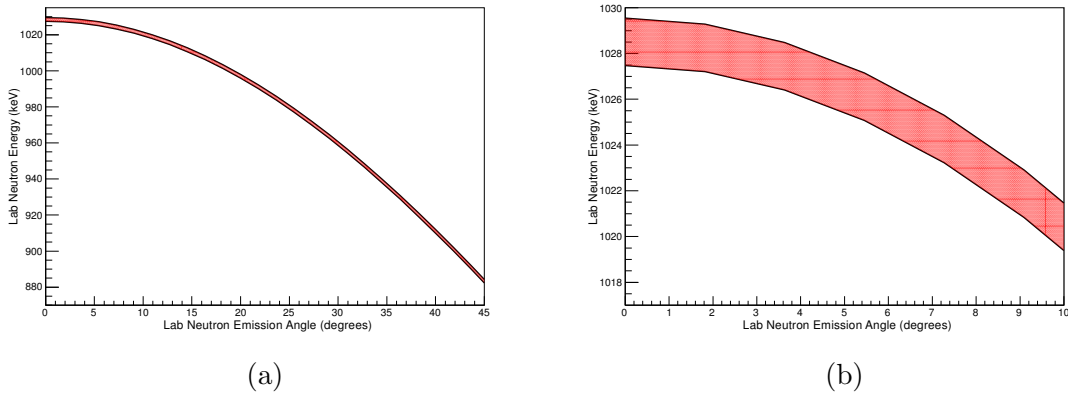


Figure 4.3: (a) shows the neutron energy band (keV) (*red shaded*) as a function of emission angle (degrees) in the lab frame for the thin LiF target corresponding to a maximum incident proton kinetic energy of 2.734 MeV. (b) shows the same spectrum, but only including the energies falling inside the geometric acceptance cone of the active xenon in the TPC during the neutron data runs.

in *Geant4* and fired at the chamber. It was verified that only the neutrons within this  $10^\circ$  acceptance cone significantly contributed to any scattering in the active xenon volume. Therefore, in order to maximize computation efficiency, only the band of neutron energies within the  $10^\circ$  cone were generated for the simulations. Neutrons “accidentally” entering the active volume from bouncing around the room contributed negligibly to the nuclear recoil signals. The results of the MC simulations are presented in Sec. 4.2 and Ch. 5.

## 4.2 The Kinematic Edge

When the neutrons elastically scatter off the xenon nuclei in the detector, a range of nuclear recoil energies ( $E_{nr}$ ) is produced based on the kinematic equation:

$$E_{nr} \approx 2E_n \frac{m_n m_{Xe}}{(m_n + m_{Xe})^2} [1 - \cos \theta] \quad (4.4)$$

where  $E_n$  is the neutron kinetic energy,  $m_n$  and  $m_{Xe}$  are the mass of the neutron and xenon nucleus respectively, and  $\theta$  is the scattering angle. We have seen in the previous sections, that a great deal of effort was spent on minimizing the spread in  $E_n$ , but even with mono-energetic neutrons, there is still a broad recoil energy spectrum ranging from  $\sim$ zero to the maximum recoil energy  $E_{nr,max} \rightarrow E_r$ . In this work, instead of singling out a neutron energy with coincidence measurements and complicated scattering setups, we look for the sharp drop-off in the energy spectrum corresponding to  $180^\circ$  backscattered neutrons. We call this the “kinematic edge”. In xenon, a neutron can transfer a maximum of  $\sim 3\%$  of its total kinetic energy. If the energy resolution is good enough, then the kinematic edge can be used to map the recoil response of the highest energy incident neutrons with very high accuracy. Just for comparison, in LXe, the density is high enough ( $\sim 3 \text{ g/cm}^3$ ) and neutron flux from commercial neutron generators is also high enough to perform coincidence measurements. However, gaseous xenon, even at higher pressures (here 6 bar), presents difficulties because the interaction rate is extremely low due to low densities and low neutron yield of the microbeam. Thus, coincidence measurements in HPXe would take painfully large amounts of time to execute. The general scattering setup and detector construction used in the *Geant4* simulations are shown in Fig. 4.4 along with a sample of neutron tracks. Some lead was used in a few of the early scattering data runs in an attempt to control the gamma backgrounds. The lead was simulated whenever applicable, but is not shown here for clarity. Also, the internal HDPE and PTFE plastic was simulated, but not shown here for clarity as well.

A recoil energy spectrum from the MC simulation, with perfect detector resolution, is shown in Fig. 4.5 for  $E_p = 2.734 \text{ MeV}$ . Also shown in the figure are sample neutron energy distributions that are generated by the  $\sim 0.5'' \times 0.5''$  beam spot on the LiF target, as well as the neutron energies that actually make it inside the active vol-

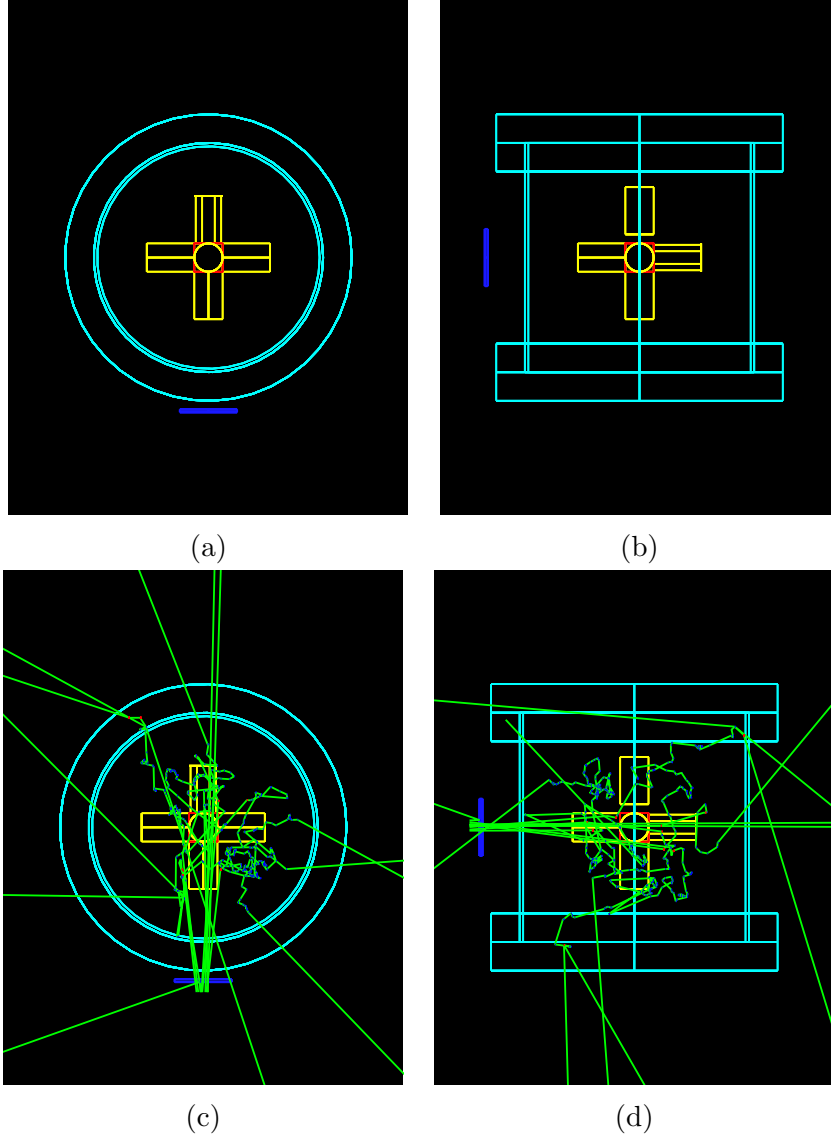


Figure 4.4: (a) and (b) show the scattering setup and detector construction used in the *Geant4* simulation. Only the quartz beam pipe window (*blue*), the SS chamber, flanges and end caps (*light blue*), PMTs (*yellow*) and active xenon volume (*red*) are shown for clarity. All the internal HDPE and PTFE was modeled, but not shown here. (c) and (d) show example neutron tracks (*green*) as the neutrons scatter off the detector components.

ume. The spectrum shows the corresponding kinematic edge for the central neutron kinetic energy  $E_n \approx 1027$  keV, which is  $E_r \approx 31.6$  keVnr. When the finite detector

resolution is added, the spectrum is smeared somewhat. This smearing, along with the conversion to the real S2 signal is accounted for and compared to the data in Ch. 5 for all neutron runs.

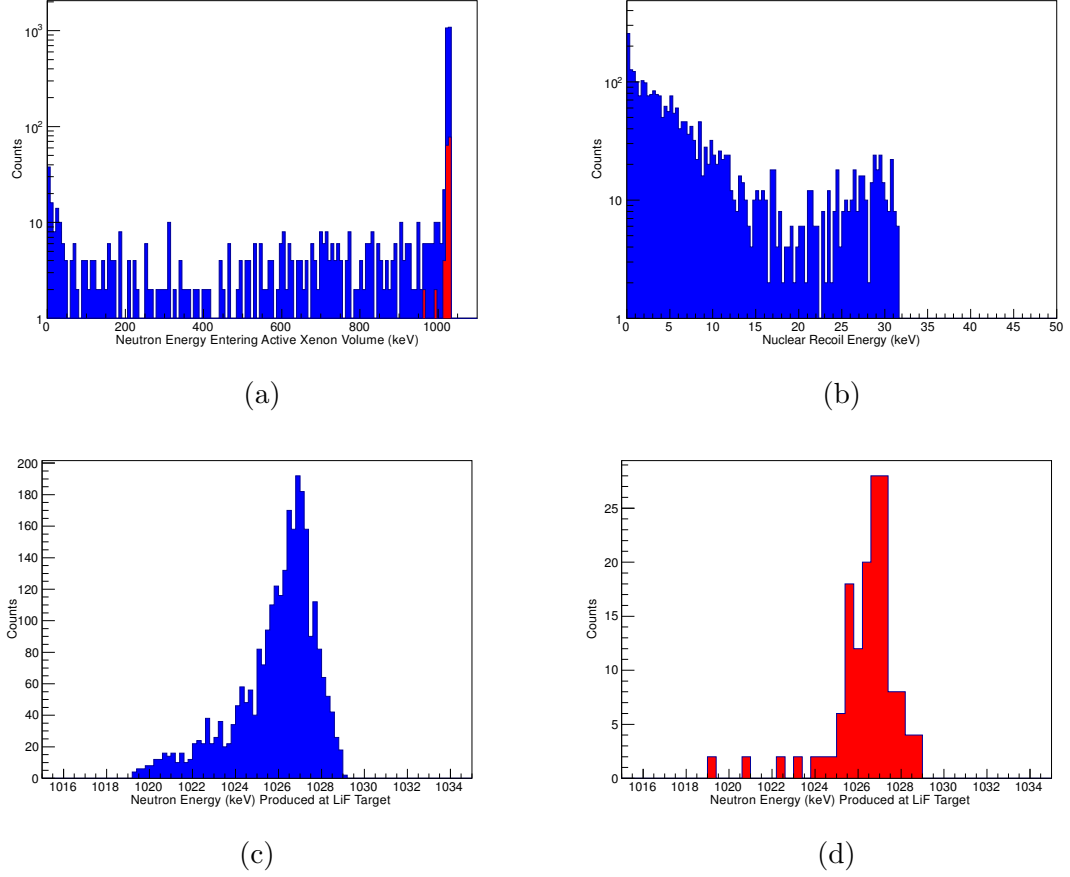


Figure 4.5: (a) shows all neutron energies (*blue*) entering the active xenon volume in the MC study for the highest energy in this work  $E_p = 2.734$  MeV. The (*red*) portion is shown for illustration and corresponds to the neutrons contributing to the  $E_{nr} > 28$  keVnr. (b) shows the xenon recoil spectrum in the TPC at 6 bar pressure for the same neutron energies in (4.5a). (c) shows the neutron energy distribution simulated at the LiF target. (d) shows the energy spread of the neutrons at the LiF target that cause recoils  $E_r > 28$  keVnr.

### 4.3 Electroluminescent (EL) Gain

Electroluminescence occurs when a drifting charge gains enough energy in a medium to cause atomic excitation through collisions, leading to subsequent relaxation and ejected scintillation photons. The S2 signal in the TPC is derived from this process and driven specifically by the total charge (*i.e.* electrons) reaching the EL gap and the potential difference between the gate and anode. The EL gain is defined as the number of emitted “secondary” photons per electron and has been studied for several years in HPXe by many different groups. See [157] and [158], for example, and references therein. Experimental techniques, especially in the form of gas purity and photo-sensing, have improved the studies dramatically in the last few years. The latest results show that for ultra-pure xenon gas (virtually free of electronegative contamination) with uniform E-field in the EL gap, the overall gain is:

$$n_{el} = 140 \int_x \left( \frac{E}{p} - 0.83 \right) p \, dx \quad (4.5)$$

where  $n_{el}$  is the total number of photons produced per electron crossing the gap,  $x$  is the gap length in cm,  $E/p$  is the reduced electric field in  $\text{kV cm}^{-1} \text{ bar}^{-1}$  (which can be a function of position),  $p$  is the pressure in bar, 140 is a gain constant with units photons/kV, 0.83 is the  $E/p$  threshold to reach the first excitation energy in xenon in these units, and the integral is calculated across the entire gap (where  $E/p > 0.83$ ). Xenon is an ideal gas, so this equation is valid for a wide range of pressures and temperatures. However, since the gain relies on the number of collisions taking place between the electrons and xenon, as well as xenon-xenon atomic collisions, a more accurate way to write this equation is in terms of the number density ( $N$ ) of xenon atoms:

$$n_{el} = 0.140 \int_x \left( \frac{E}{N} - 3.386 \right) N \, dx \quad (4.6)$$



where the units are altered slightly so that the reduced electric field  $E/N$  is now in Td units ( $10^{-17}$  V cm<sup>2</sup> atom<sup>-1</sup>) and the constants are adjusted accordingly.

Calculating the EL gain is trivial for a uniform E-field. However, the TPC geometry and voltage settings chosen for this work produce fields that vary near the anode wire surfaces in the EL gap. In order to account for these non-linear effects, E-field calculations had to be combined with direct excitation simulation within the *Garfield* framework to compute the actual gain. Since there was, at the time of this work, no way to generate the 3d E-fields in *Garfield* and simulate the gas properties and drifting electrons simultaneously, some simplifications were made. Detailed E-field maps were generated in 3d using *COMSOL Multiphysics*. These maps were used to convert the 3d geometry to an equivalent 2d geometry that could be modeled directly in *Garfield* and used to perform the excitation calculations. The geometry and voltages are shown in Fig. 4.6. In order to calculate the E-fields, only a unit cell of one wire crossing point is required, but four wire crossing points are used for illustration. The E-fields are shown in Fig. 4.7. Some rough EL gain calculations were performed in *COMSOL* by integrating the gain equation along selected paths (*e.g.* along line segments corresponding to the E-field lines shown at the far right of Fig. 4.6). However, these calculations do not account for diffusion and the relatively tortuous path of the electrons. *Garfield* with the *Magboltz* and *Heed* interfaces properly account for the diffusion of the drifting electrons and their more realistic trajectories in an E-field.

Before we discuss the actual *Garfield* result, we present the method to convert from 3d to 2d. In order to convert from the 3d field map of the crossed-wire meshes to an equivalent 2d parallel wire geometry, we had to carefully choose the wire diameters, pitch and voltages for the simulation. In other words, we can not simply use the actual crossed-wire mesh wire diameter and pitch in the 2d model. We had

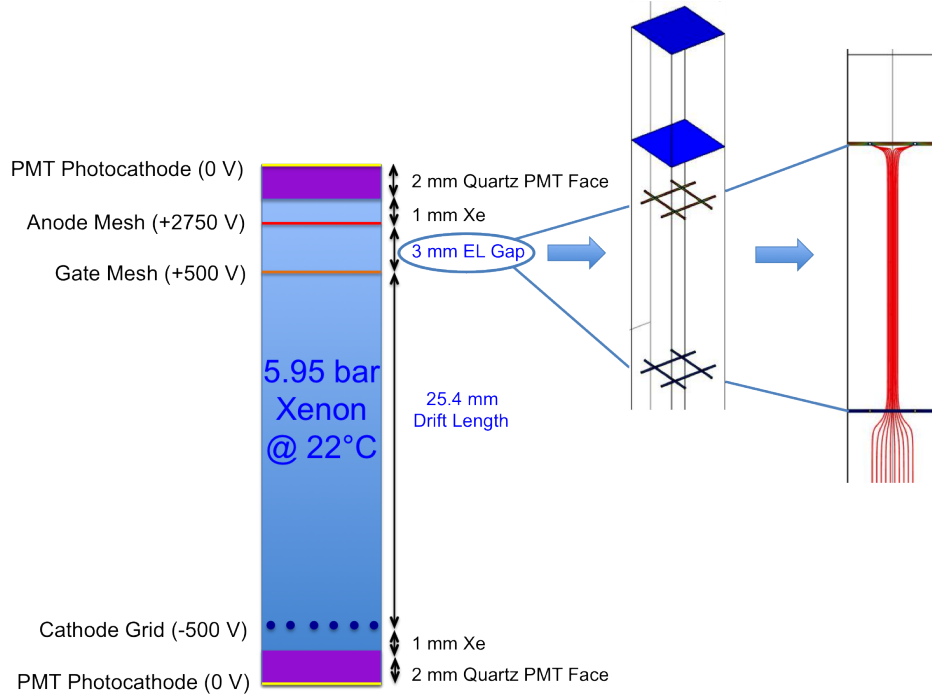


Figure 4.6: Cross-section of the center of the TPC (*left*) with the cathode, gate and anode planes shown with voltages labeled, as well as the PMT faces nearest the cathode and anode. The *middle* figure shows the 3d image of the unit cell of the crossed-wire mesh used to calculate the E-fields in *COMSOL*. The *right* figure shows where the majority of field lines (*red*) originating in the drift region end up on the anode.

to somehow account for the additional “electrode density” in the y-direction. It is common to scale the 2d geometry of a parallel wire grid to larger/smaller dimensions in order to optimize computation performance. For example, consider an EL gap made of two parallel wire planes (gate and anode). Assuming the EL gap length is large compared to the wire pitch and diameter, then one can produce an identical electrostatic situation if the wire pitch and diameter are scaled such that the ratio of pitch-to-diameter ( $p/d$ ) is maintained. Along the same lines, in order to maintain identical electrostatics from 3d to 2d, the  $p/d$  from the crossed-wire mesh was scaled with an additional factor of  $\sqrt{2}$  to average out the effects of the 2d plane of wires.

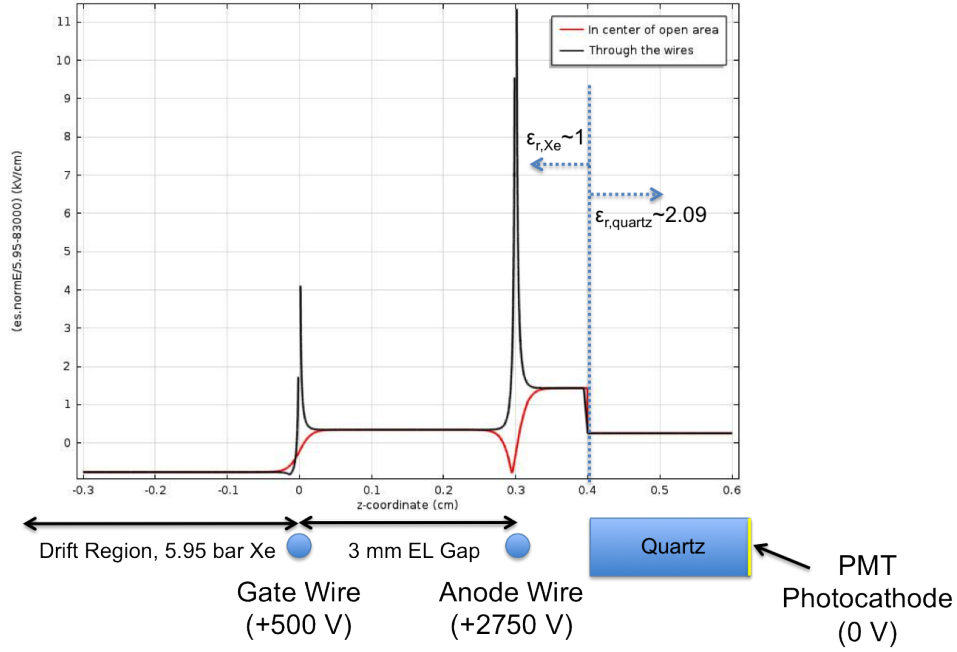


Figure 4.7: Reduced electric fields in the TPC as a function of  $z$ -position along the axis of the drift field. The vertical scale corresponds to  $(E/p - 0.83)$  so that any value above zero produces EL light. The enhancement just to the right of the anode is due to the difference in relative permittivities of the xenon and quartz PMT face.

This is explicitly shown as:

$$\left(\frac{p}{d}\right)_{2d} \approx \frac{1}{\sqrt{2}} \left(\frac{p}{d}\right)_{3d} \quad (4.7)$$

The 2d geometry is shown in Fig. 4.8. The same dimensions are used for the gate and anode, since they are identical in reality. In addition to choosing suitable 2d wire diameters and pitch, appropriate voltages had to be calculated using the actual 3d bulk E-fields from the detailed *COMSOL* map, labeled  $E_1$ ,  $E_2$  and  $E_3$  in Fig. 4.8. Given the wire diameters, pitch, grid/plane spacings and bulk E-fields, the electrode voltages can be determined with a simple calculation. The procedure is described well in [159], so it will not be repeated here. The resulting parameters for the 2d *Garfield* model are summarized in Table 4.1. The E-fields from the 3d and 2d

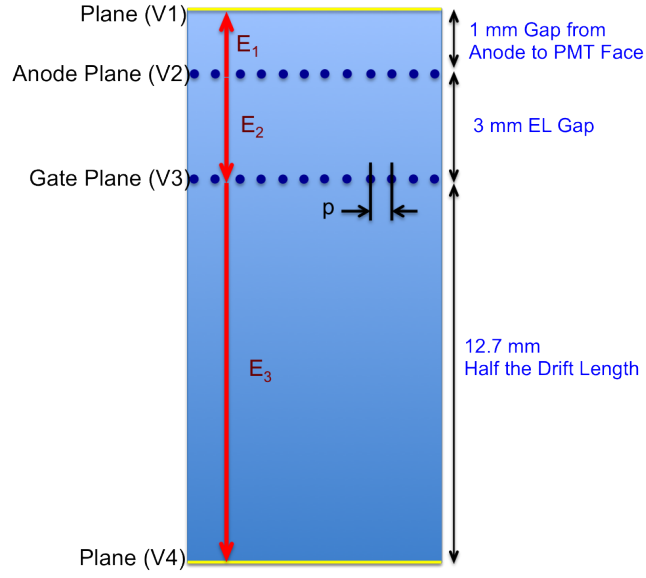


Figure 4.8: 2d geometry used in the *Garfield* simulation.

Table 4.1: Summary of parameters used in the 2d *Garfield* model. See Fig. 4.8 for corresponding geometry.

Parameter	Value	Units
$V_1$	+1272	V
$V_2$	+2808	V
$V_3$	+ 460	V
$V_4$	+ 8	V
$E_1$	13.461	kV/cm
$E_2$	6.990	kV/cm
$E_3$	0.404	kV/cm
$p$	444.5	$\mu\text{m}$
$d$	38.1	$\mu\text{m}$

models are shown in Fig. 4.9 for comparison. The two models only deviate slightly in the region within  $\lesssim 10 \mu\text{m}$  from the wire surfaces.

The xenon gas (5.95 bar at 22°C) was then added to the *Garfield* simulation and electrons were released from arbitrary points in the drift region and allowed to drift

into the EL gap. A plot of the typical electron paths is shown in Fig. 4.10. For the most part, the electrons travel along paths similar to the E-field lines shown in Fig. 4.11, commonly landing on the “side” of an anode wire. However, some electrons actually penetrated the region between the anode and the associated PMT (from now on designated the anode PMT). Out of those penetrating that region, some curved back and were captured by the anode, but some traveled all the way to the PMT face.<sup>1</sup> A plot of the final position of the electrons, after being captured by an electrode, is shown in Fig. 4.11a. The total EL gain per electron was calculated by counting the number of excitations caused by each electron in the simulation and assuming that each excitation lead to a single photon. The number of excitations above the first excitation level was negligible, so only first excitations are counted. Similarly, at these voltage settings, a negligible amount of secondary ionization occurs, so secondary electrons were not considered.<sup>2</sup> The results are plotted in Fig. 4.11b. The most prominent peak corresponds to the majority of the electrons that land on the “side” of an anode wire. The small peak to the left is from electrons with shorter paths, mostly landing on the “front” surface of the anode wire. The broad spread of gains to the right of the large peak is from electrons that penetrate significantly into the space “behind” the anode and either get captured by the anode or go on to land on the PMT face. Charge-up of the PMT face was not accounted for here. The prominent peak was fitted with a Gaussian curve with a mean of  $\sim 198$  ph/e<sup>-</sup>. A more detailed representation of the various electron hit positions and the corresponding gains is shown in Fig. 4.12.

The gain was verified using 60 keV gammas from an <sup>241</sup>Am source, in conjunction

---

<sup>1</sup>An interesting follow-on study is to map out the long term effects for the PMT face charge-up, including possible electrolysis of the quartz, but that was not done here.

<sup>2</sup>It is important to note that similar TPCs would benefit greatly from these types of studies, especially those that rely on good energy resolution, which is degraded by secondary charge.

with ionization data ( $W_{ion}=22.4$  eV/e<sup>-</sup>) from the literature [157]. The gain setting corresponded to  $\sim 21$  photoelectrons/electron.

In order to finish off the full characterization of the TPC, the gain calibration data had to be reconciled with an accurate accounting of the light collection efficiency. This is discussed in the next section.

## 4.4 Light Simulation

In order to validate the EL gain calculation and extrapolate the S2 signal to the actual number of electrons arriving at the anode, a very accurate knowledge of the light collection efficiency (LCE) was required. The close-packed nature of the components guarantees very good geometrical solid angle coverage, but the finite transparency of the electrodes, the reflectivity of the PTFE and the PMT QE all contribute to the overall LCE for both S1 and S2. All of these properties were simulated in a custom ray-tracing program and the overall LCE was calculated. In addition, the ray-tracing was used to determine the light sharing among the PMTs, which aided in event selection based on x-y position.

### 4.4.1 *Material optical properties*

All electrodes were made of Type 304 SS, with no special polishing or other surface treatment beyond the cleaning outlined in Sec. 3.1.2. A value of 4% reflectivity was assigned to all electrodes, which is a conservative rough approximation of the reflectivity of SS to xenon scintillation light. None of the Al metal was exposed to the light. The amount of light reflected by the electrodes was exceedingly small ( $\ll 1\%$  of the total light), so a photon reflecting off an electrode was allowed to simply pass through, contributing to a fractional increase in the electrode's optical transparency. The geometry and associated optical transparencies to light at normal incidence to the plane of wires is summarized in Table 3.1.

The PTFE surfaces were characterized by diffuse reflection with an overall reflectivity of 70%. If a photon reflected off a PTFE surface, then its direction was randomly re-generated at the reflection point into a  $2\pi$  solid angle outward from the surface.

The PMT faces were not given any reflective properties. When a photon reached any PMT face, it was counted as a successful hit in the corresponding PMT. It was assumed that any reflectivity or absorption in the quartz is accounted for in the QE. Thus, the QE value of 15% was applied after the successful photon hits were counted.

#### 4.4.2 S1 light collection efficiency

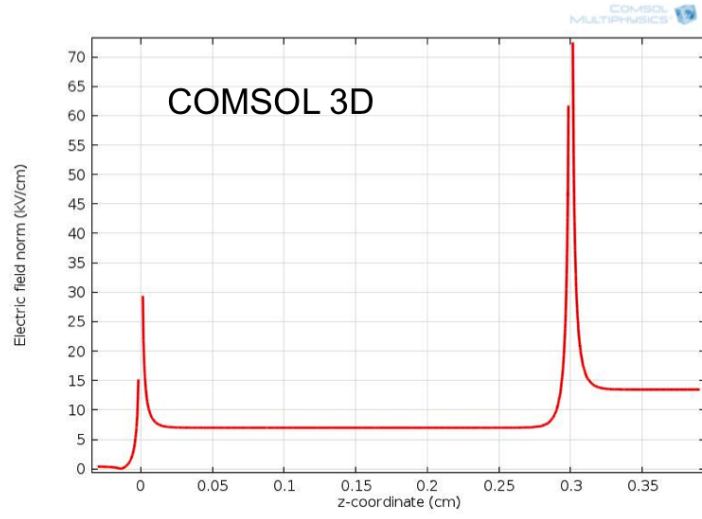
Primary scintillation photons (S1) are produced isotropically in the gas at very localized regions in the active volume of HPXe for a given energy deposition. To calculate the S1 LCE ( $\epsilon_{S1}$ ), photons were generated randomly throughout the  $1'' \times 1'' \times 1''$  volume of active xenon with randomized directions. The resulting  $\epsilon_{S1}$  is shown in Fig. 4.13 (*lower right*) after PMT QE was applied. The overall LCE was fitted by a Gaussian with mean  $\bar{\epsilon}_{S1}=0.125$  and  $\sigma=0.004$  calculated over the entire geometry.

#### 4.4.3 S2 light collection efficiency

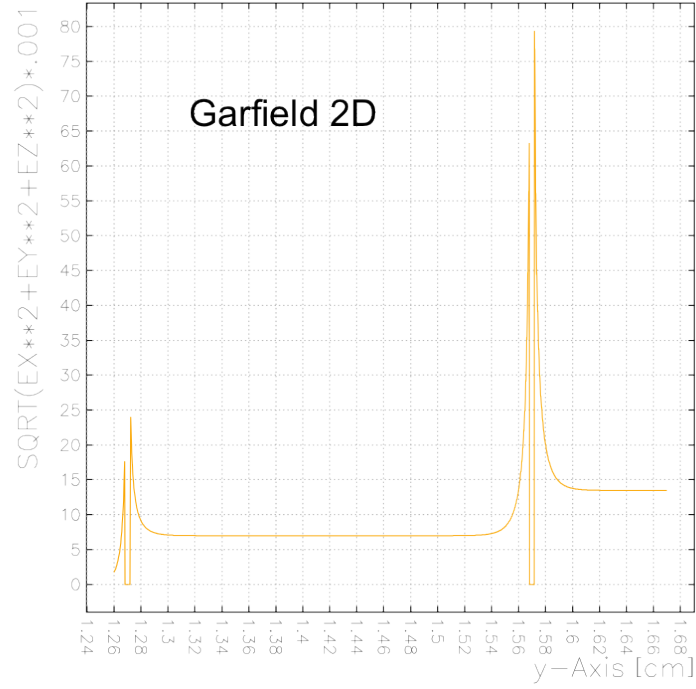
Secondary scintillation photons (S2) are produced isotropically along each electron's path as it traverses the EL gap and terminates on the anode. To calculate the S2 LCE ( $\epsilon_{S2}$ ), photons were generated randomly along straight line paths between the gate and anode at random x-y positions. For example, a 29.7 keV x-ray produces an average of 1326 electrons for  $W_{ion}=22.4$  eV/e<sup>-</sup>. If the gain is 198 ph/e<sup>-</sup>, then we expect an average of  $\sim 260,000$  ph to be produced. To simulate this, the EL gap was broken into 260,000 equal sized steps in the z-direction. A single photon was generated at each step location and tracked until absorbed or captured by a PMT face. The results are plotted in Fig. 4.14.

In order to identify the x-y position of real events in the chamber, simple light sharing was used between opposing side PMTs. Due to the compact geometry, an ambiguity arises in the reconstruction of x and y positions. The light simulation reproduced this effect and is shown in Fig. 4.15. The effect manifests itself as a sort of “folding-in” of the corners. This corner folding is understood by realizing that the anode PMT face is a circle, but the x-y plane “seen” by drifting electrons (and subsequently by the photons) is a square. Therefore, the corners of the EL region are not covered by the anode PMT face and events occurring there will produce a lower fractional light yield in the anode PMT. The problem is easily fixed by requiring a certain fraction of the total light collected to be in the anode PMT, eliminating the events from contaminating the lower energy region of interest. The resulting total  $\bar{\epsilon}_{S2}=0.104$  with  $\sigma=0.006$  from a Gaussian fit, after the anode PMT fractional light cut.





(a)



(b)

Figure 4.9: (a) and (b) show the electric fields  $|\vec{E}|$  as a function of z-position from the 3d “real” geometry from *COMSOL* and the 2d scaled model from *Garfield* respectively. The vertical axis on both plots is in kV/cm. The horizontal axes are in local model coordinates in units of cm.

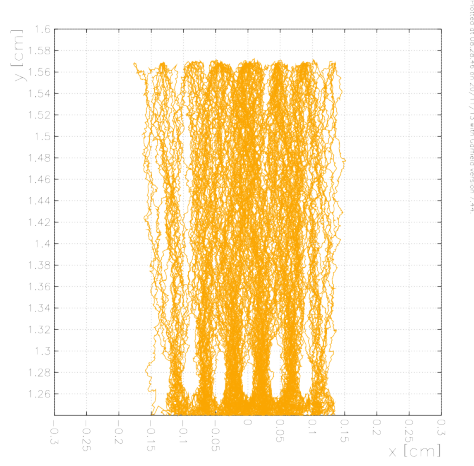


Figure 4.10: Typical electron paths from the drift region (below the plotted area) into the EL gap. The gate wire grid plane is located at  $y=1.27$  cm and the anode plane is at  $y=1.57$  cm.

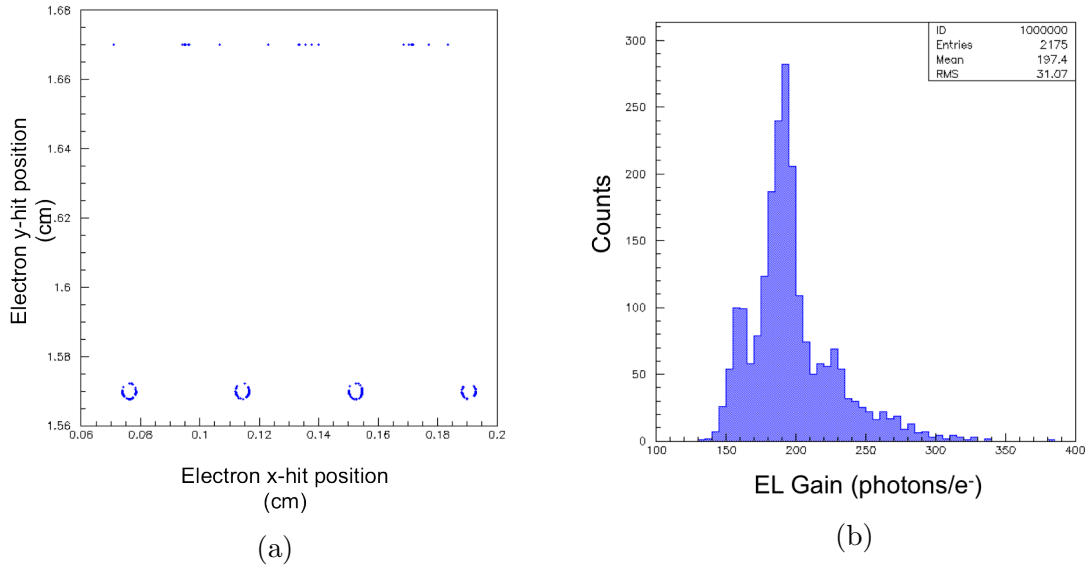


Figure 4.11: (a) shows the hit pattern of the electrons on the anode ( $y = 1.57$  cm) or PMT face ( $y = 1.67$  cm). (b) shows the EL gain per electron from the *Garfield* simulation.

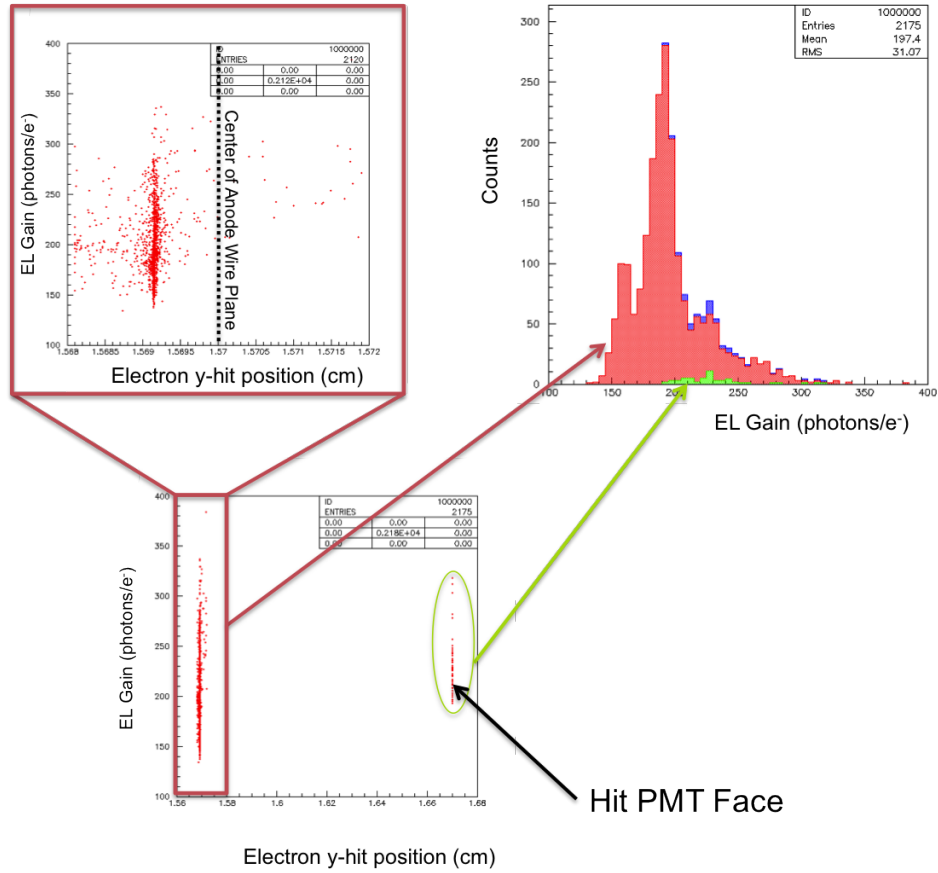


Figure 4.12: Composite showing the EL gain as a function of  $y$ -position near an anode wire (*top left*) and a similar plot, zoomed out to include the anode and PMT face (*bottom*). The remaining plot (*top right*) shows the total histogram of the EL gains, with the corresponding gains highlighted.

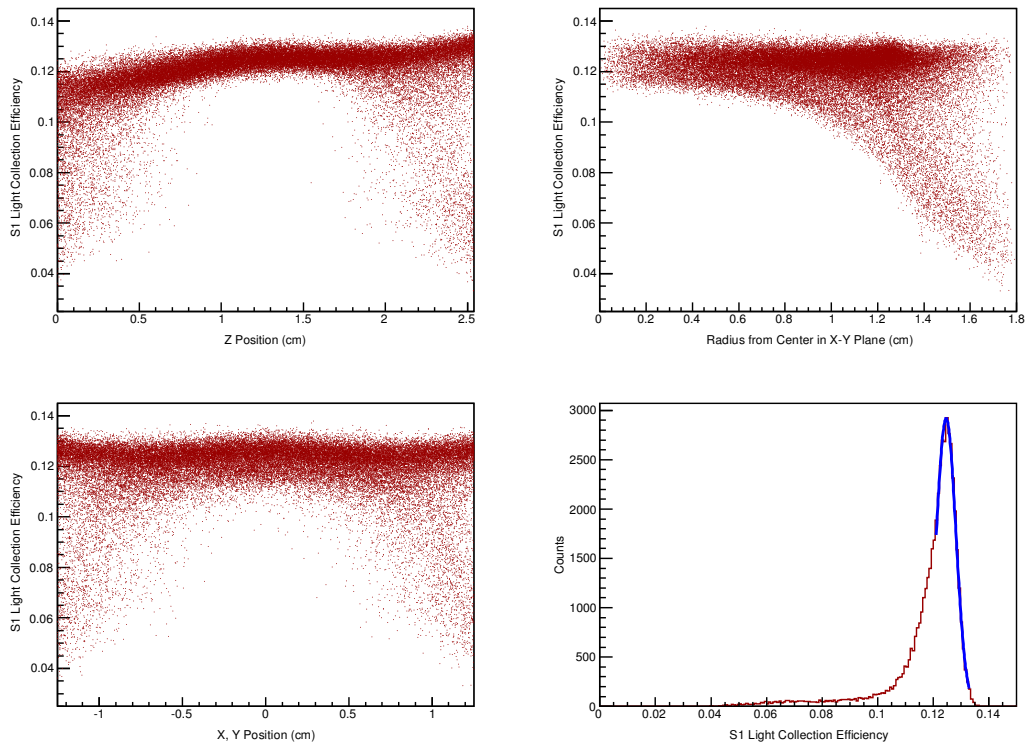


Figure 4.13: Plots showing the S1 LCE as a function of simulated z position (*upper left*), x (or y) position (*lower left*), radius from the center in the x-y plane (*upper right*) and the total LCE histogram.

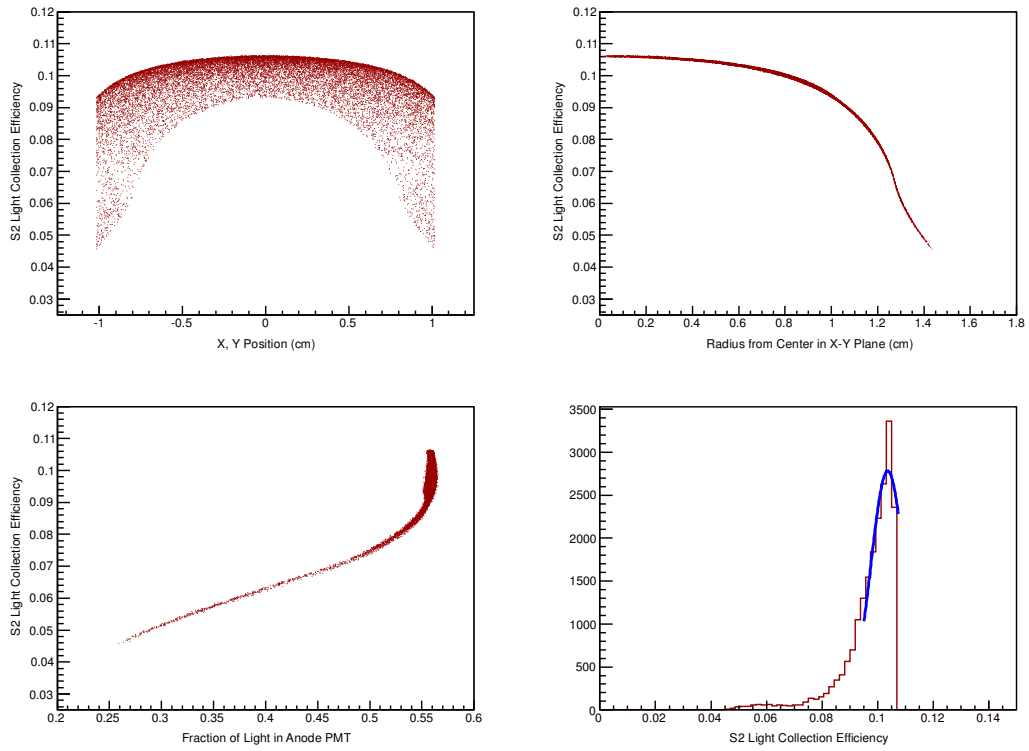


Figure 4.14: Plots showing the S2 LCE as a function of simulated x (or y) position (*upper left*), fraction of the total light captured by the anode PMT (*lower left*), simulated radius from the center in the x-y plane (*upper right*) and the total LCE histogram. The *blue curve* in the *lower left* plot is a Gaussian fit of the S2 LCE with mean  $\bar{\epsilon}_{S2} = 0.104$  and no selection cuts applied.

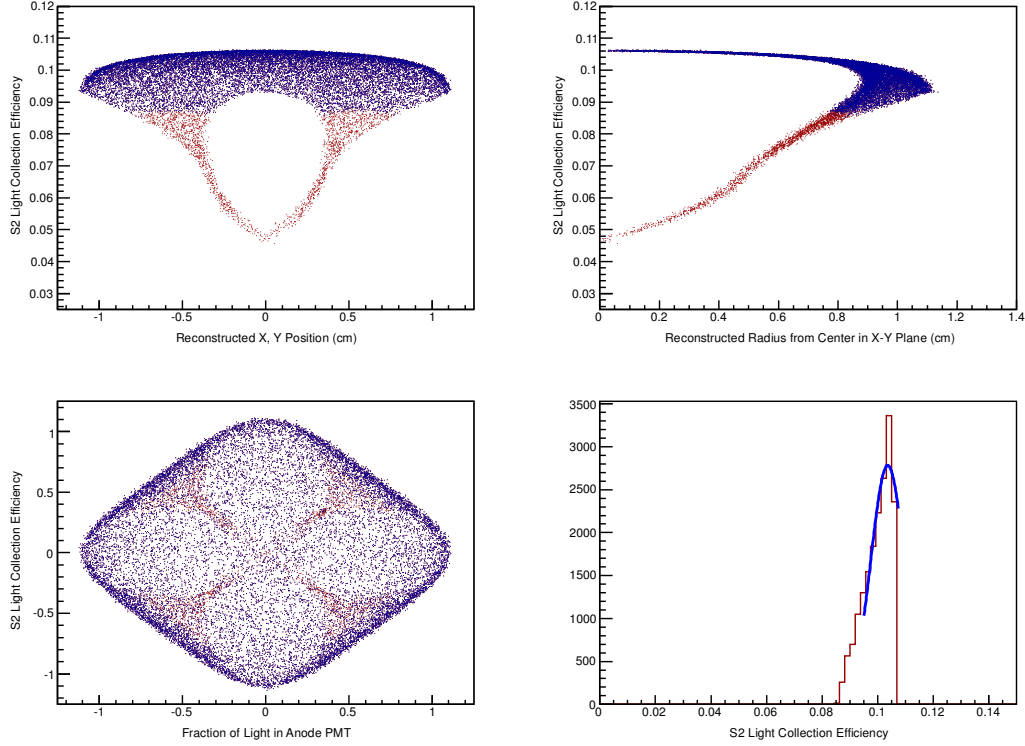


Figure 4.15: Plots showing the S2 LCE as a function of reconstructed x (or y) position (*upper left*), reconstructed x-y position (*lower left*), reconstructed radius from the center in the x-y plane (*upper right*). The *red* points show all events for all simulated positions. The *blue* points show the reconstructed points after selecting only events with a high fraction of light ( $a_{\text{anodePMT}}/a_{\text{total}} > 0.55$ ) in the anode PMT. The *blue curve* in the *lower right* plot is a Gaussian fit of the total S2 LCE with mean  $\bar{\epsilon}_{S2} = 0.104$  after the anode PMT fractional light cut.

## 5. RESULTS

Nuclear recoil data was taken in HPXe at a pressure of 5.95 bar (22 °C) for nuclear recoil energies in the range of  $1.56 \text{ keVnr} < E_r < 31.55 \text{ keVnr}$ . The goal of this research was to measure the nuclear recoil response for both S1 (light) and S2 (charge) and compare the results with electron equivalent energy (keVee) depositions. The S1 signals were too poorly resolved in the current data set to provide consistent S1+S2 combined analyses. An effort was being made to improve the data, but equipment failure in the proton beam line halted the project, limiting the current data set to the results presented below. The primary focus was shifted to measuring only the charge produced by recoiling nuclei and calculating the nuclear ionization quenching factor,  $\mathcal{Q}$ . The results and a comparison to the simulated data are presented in this chapter.

### 5.1 Event Selection

Data is normally collected in a noble gas TPC by using a hardware trigger on S1 light and recording a specified time window corresponding to a time greater than the maximum drift time of the chamber. Every attempt was made to operate in this mode for the nuclear recoil runs, but at  $E_r \lesssim 12 \text{ keVnr}$ , the S1 trigger efficiency was too low. The decision was made to switch to an S2 only trigger for all energies less than 16 keVnr to avoid systematic trigger uncertainties. The trigger and event selection is described for both S1 and S2 hardware triggers in this section.

#### 5.1.1 S1 trigger

For nuclear recoil energies  $E_r \geq 16 \text{ keVnr}$ , an S1 trigger was used for all events in a given run. A hardware coincidence of 2 photoelectrons (pes) occurring within a

gated 300 ns window was required to trigger the DAQ. The maximum drift time of the electrons from the cathode to the gate was  $\sim 25 \mu\text{s}$ , so the total event window was chosen to be  $35 \mu\text{s}$  and was split into three signal regions. The first  $4 \mu\text{s}$  of the recorded window were reserved for event-by-event background determination. The sub-window  $4 \mu\text{s} < t < 7 \mu\text{s}$  contained the S1 pulse, with the trigger located at  $5 \mu\text{s}$ . The remaining  $7 \mu\text{s} \leq t < 35 \mu\text{s}$  comprised the S2 pulse window. Some minimal “level two” software triggers were implemented to improve the chance of recording both S1 and S2 signals for each event. This level two trigger consisted of a maximum of 500 S1 pes and a minimum of 40 S2 pes summed over all PMTs. In addition, a minimum of 25% of the summed S2 light was required to be in the anode PMT. Further quality cuts were made offline during analysis. The first of these was to remove the x-y ambiguity shown in Fig. 4.15 by requiring at least 45% of the summed S2 to be in the anode PMT. The remaining cuts were made to the pulse timing and removed events near the various electrodes. To do this, the drift time ( $t_d$ ) was limited to  $4 \mu\text{s} < t_d < 24 \mu\text{s}$  and the S2 pulse widths ( $t_w$ ) were limited to  $1 \mu\text{s} < t_w < 1.9 \mu\text{s}$ . The  $t_w$  is determined by first finding the times at which 10% ( $t_{10}$ ) and 90% ( $t_{90}$ ) of the S2 pulse area has been recorded, then taking the difference between the two, where  $t_w = t_{90} - t_{10}$ . An example waveform triggered by S1 and produced by a 29.7 keV x-ray or electron is shown in Fig. 5.1a, while an example S1 triggered nuclear recoil ( $E_r \approx 28. \text{ keVnr}$ ) waveform is shown in Fig. 5.1b.

### 5.1.2 S2 trigger

For nuclear recoil energies  $E_r < 16 \text{ keVnr}$ , the hardware trigger consisted of a minimum of two pes in the anode PMT. This corresponded to triggering on raw waveforms that were 20 mV above background on the amplified ( $\times 10$ ) anode PMT signal. Although this seems low, considering one electron is expected to generate



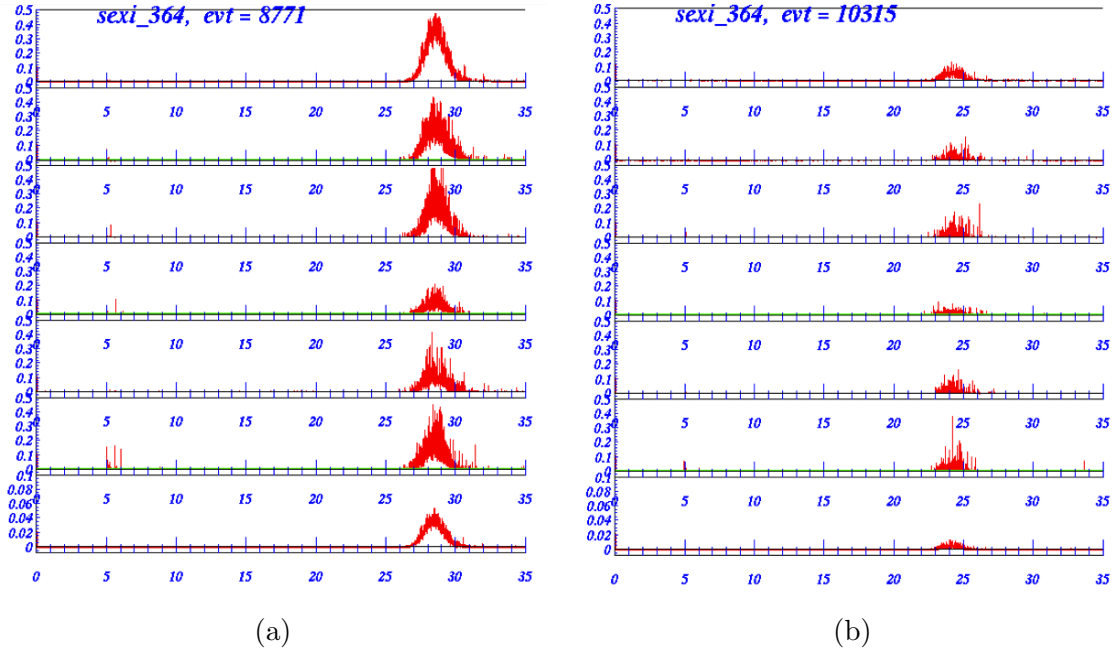


Figure 5.1: Typical PMT signal waveforms for a 29.7 keV x-ray (a) and a  $\sim 28$  keVnr nuclear recoil (b) from the S1-triggered data. The S1 is barely or not at all visible on these full scale images. A total of 7 channels are shown. The bottom channel is the un-amplified ( $\times 1$ ) anode PMT signal. The six channels above it are the amplified ( $\times 10$ ) signals from the cathode PMT (*second from bottom*), the side PMTs and the ( $\times 10$ ) anode PMT (*top*).

an average of  $\sim 21$  photoelectrons in the PMTs, it is appropriate because these low level signals often reach the PMTs as a “train” of photons. The individual peaks in a particular waveform could be separated in time, up to the full pulse width of  $1.9 \mu\text{s}$  or so.

The event timing window had to be carefully chosen for this type of trigger. The signal causing the trigger can be low enough to be caused by S1 or S2. Therefore, a longer time window was chosen, providing the option to look both forward and backward around the trigger time. The desired signal is one that triggers on a real S2 pulse with an S1 pulse simply observed at an earlier time. A  $50 \mu\text{s}$  window was chosen with the trigger occurring at  $30 \mu\text{s}$ . The level two software trigger required

at least 1 pe from any other PMT within the time sub-window of  $27 \mu\text{s} < t < 37 \mu\text{s}$ , a pulse width of  $1 \mu\text{s} < t_w < 1.9 \mu\text{s}$ , and at least 45% of the S2 light required to be in the anode PMT. Offline cuts were applied, similar to the S1 triggered data. The drift time between the triggered S2 pulse and an assumed S1 pulse occurring prior to the trigger was required to be  $5 \mu\text{s} < t_d < 24 \mu\text{s}$ . If an S1 pulse was found in multiple PMTs, then the pulses had to occur within 4 ns of each other. Otherwise, random single pes were counted as S1 signals. An example waveform triggered by S2 and produced by a 29.7 keV x-ray is shown in Fig. 5.2a, while an example S2 triggered nuclear recoil ( $E_r \approx 1.2 \text{ keVnr}$ ) waveform is shown in Fig. 5.2b.

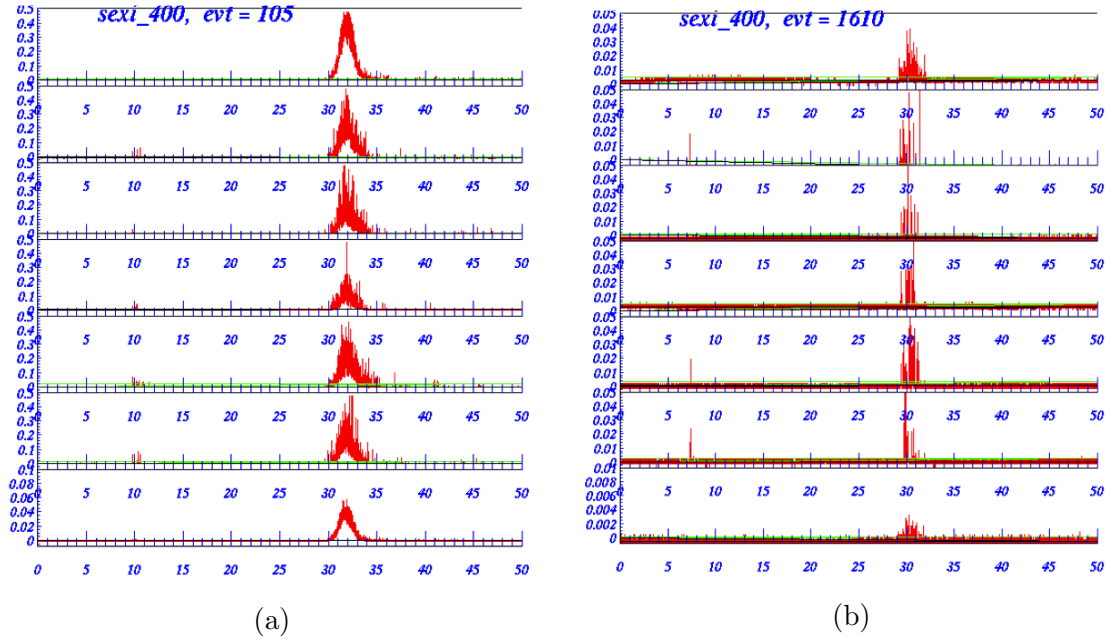


Figure 5.2: Typical PMT signal waveforms for a 29.7 keV x-ray (a) and a  $\sim 1.2 \text{ keVnr}$  nuclear recoil (b) from the S2-triggered data. The S1 is barely or not at all visible on the full scale image in (a). The S1 of 4 photoelectrons is seen on the  $\times 10$  image in (b) along with an S2 of 233 photoelectrons. A total of 7 channels are shown. The bottom channel is the un-amplified ( $\times 1$ ) anode PMT signal. The six channels above it are the amplified ( $\times 10$ ) signals from the cathode PMT (*second from bottom*), the side PMTs and the ( $\times 10$ ) anode PMT (*top*).

## 5.2 Nuclear Recoil Measurements

Several nuclear recoil data runs were taken ranging in maximum recoil energies  $1.56 \text{ keVnr} < E_r < 31.55 \text{ keVnr}$ , but only the most stable runs were used in the final analysis. If the proton beam energy started to wander, then the run was aborted. The fluctuation in the proton energy was caused by the bending magnet field value, which commonly varied  $\pm 5 \mu\text{T}$ , corresponding to  $< 0.5 \text{ keV}$  proton energy. The full data runs typically took several hours to complete, so if the bending magnet field value deviated  $\pm 10 \mu\text{T}$  from the primary energy setting for more than 5 minutes, the run was stopped and the beam was allowed to “rest”. The beam was subsequently re-calibrated using the  $\text{BF}_3$  counter upon commencing another run.

The total number of S1 and S2 pes was summed for each waveform in each data run. The raw S2 spectrum was plotted, showing a distinct x-ray escape peak at 29.7 keVee. The electron equivalent energy scale was set independently for each run by fitting the 29.7 keVee peak with a Gaussian. The number of electrons ( $\mathcal{E}$ ) was also determined from the fitted 29.7 keVee peak, using  $W_{ion}=22.4 \text{ eV/e}^-$ . Thus, the mean number of electrons at 29.7 keVee peak is  $\mathcal{E}_{cal} = 1326 \text{ e}^-$ .

In most of the spectra, the kinematic edge caused by the elastic backscattering is distinct and quite easy to pick out by eye. However, the edge selection had to be formalized in order to remove any artificial biasing in the data. This was done by calculating the average bin content ( $\mu_b$ ) over a fairly uniform region of background for each S2 spectrum. This region is usually between  $\sim 7$  to 20 keVee. Then, a search algorithm was implemented to look for the first bin ( $E_{edge}$ ) with contents greater than  $3\sigma_b$  above the computed  $\mu_b$ , where  $\sigma_b = \sqrt{\mu_b}$ . Finite energy resolution and gamma backgrounds caused this search routine to trigger on many obviously false positives at relatively high energies, particularly for stray individual bins. The algorithm was

augmented and refined by adding two subroutines. The first subroutine required that the bin to the left (lower energy) of the candidate kinematic edge bin be greater than zero. The second subroutine required the four bins to the left to be greater than  $0.45(3 \sigma_b) + \mu_b$ . This had the effect of requiring an expected accumulation of events at energies lower than the kinematic edge. The bin size chosen corresponded to  $\sim 4$  electrons/bin.

Once the kinematic edge ( $E_{edge} \rightarrow E_r$ ) was determined in the data, it was converted to an equivalent number of electrons ( $\mathcal{E}$ ) and, thus, an electron equivalent energy ( $E_{ee}$ ) using the fitted photoelectron peak at 29.7 keVee for each run. The specific charge yield ( $Q_y$ ) was then computed,  $Q_y = \mathcal{E}/E_r$ . The ionization quenching factor ( $\mathcal{Q}$ ) was determined by dividing the electron equivalent energy from the kinematic edge into the maximum recoil energy determined from the mean of the incident neutron energy distribution. (See *upper left* plots in Figs. 5.3 - 5.14.)

$$\mathcal{Q} = \frac{E_{ee}}{E_r} \quad (5.1)$$

Summary plots from the MC simulation and the nuclear recoil data are shown in Figs. 5.3 - 5.14.

The MC was scaled in two different ways in order to compare with the data. The first method was to compute the expected number of photoelectrons ( $S2_{pe}$ ), which required using the full complement of simulations in the following equation:

$$S2_{pe} = \left( \frac{E_{nr} \bar{\epsilon}_{S2} n_{el}}{W_{ion}} \right) \mathcal{Q} \quad (5.2)$$

where  $E_{nr}$  is the “true” nuclear recoil energy from the MC spectrum,  $\bar{\epsilon}_{S2} = 0.105$  is the average S2 light collection efficiency,  $n_{el} = 198$  photons/e<sup>-</sup> is the average EL gain

per electron,  $\mathcal{Q}$  is the ionization quenching factor for the corresponding data run, and  $W_{ion} = 22.4\text{eV/ion}$  is the average energy required to produce an electron/ion pair. These values were then “smeared” using a Gaussian distribution and an approximate energy resolution ( $\sigma_{MC}$ ), which was scaled from the mean ( $E_{cal}$ ) and width ( $\sigma_{cal}$ ) of the Gaussian fit of the 29.7 keV escape peak for each run according to the following equation:

$$\sigma_{MC} = \sigma_{cal} \sqrt{\frac{E_{cal}}{E_{edge}}} \quad (5.3)$$

The overall number of events in the MC spectrum was roughly matched to the number of nuclear recoil events in the data after all cuts were applied. A random background was generated and roughly normalized to the approximate number of background events occurring in each run, which varied due to exposure time, beam energy and shielding. The final simulated MC S2 photoelectron spectra were overlaid on the S2 photoelectron plot. See the *bottom left* of the summary plots. The MC spectra show an excess of events at very low energies ( $E_r \lesssim 12\text{ keVnr}$ ) when compared to the S1 triggered data. This was due to the poor S1 trigger efficiency in that energy range, as discussed above.

The second method of comparing the MC simulation to the real data consisted of converting the  $E_{nr}$  values to an equivalent number of electrons. Rather than using the simulations again, as in the case of converting to photoelectrons described above, this method is different in that it does not explicitly rely on a detailed knowledge of the light collection efficiency nor the EL gain. The number of electrons ( $\mathcal{E}_{MC}$ ) was computed by multiplying the  $E_{nr}$  values from the MC by the calculated charge quenching factor ( $\mathcal{Q}$ ) from the data, then dividing by  $W_{ion} = 22.4\text{ eV/ion}$ . The result was then smeared using a Gaussian distribution and the approximate energy resolution similar to the description above. These results were overlaid on a separate

plot of S2 electrons. See the *bottom right* of the summary plots in Figs. 5.3-5.14.

The results of the  $\mathcal{Q}$  calculations are summarized in Table 5.1. Also shown in the table are the total electron yields ( $\mathcal{E}$ ), the specific charge yield energy ( $Q_y$ ) in number of electrons per nuclear recoil energy, and the electron equivalent energies ( $E_{ee}$ ). All values are accompanied by  $1\sigma$  statistical errors, which were calculated in quadrature (see Sec. 5.3). The results are plotted in Figs. 5.15 - 5.16 with  $1\sigma$  errors indicated by vertical and horizontal bars.

Table 5.1: Summary of results for all nuclear recoil data runs. The  $1\sigma$  statistical error is given for all derived quantities. The statistical error in the recoil energies ranges from 0.03 to 0.08 keVnr.

$E_r$ (keVnr)	$\mathcal{E}$ Total Number of $e^-$	$Q_y$ Specific Charge Yield ( $e^-/\text{keVnr}$ )	Electron Equivalent Energy (keVee)	$\mathcal{Q}$ Ionization Quenching Factor
31.55	$201 \pm 14.2$	$6.37 \pm 0.45$	$4.50 \pm 0.33$	$0.143 \pm 0.011$
27.93	$159 \pm 12.6$	$5.69 \pm 0.45$	$3.56 \pm 0.29$	$0.128 \pm 0.011$
25.93	$162 \pm 12.7$	$6.25 \pm 0.49$	$3.63 \pm 0.30$	$0.140 \pm 0.011$
23.93	$144 \pm 12.0$	$6.02 \pm 0.50$	$3.23 \pm 0.28$	$0.135 \pm 0.012$
21.93	$120 \pm 11.0$	$5.47 \pm 0.50$	$2.69 \pm 0.25$	$0.123 \pm 0.012$
15.94	$82 \pm 9.1$	$5.15 \pm 0.57$	$1.84 \pm 0.21$	$0.115 \pm 0.013$
14.68	$77 \pm 8.8$	$5.25 \pm 0.60$	$1.73 \pm 0.20$	$0.118 \pm 0.014$
11.91	$56 \pm 7.5$	$4.70 \pm 0.63$	$1.25 \pm 0.17$	$0.105 \pm 0.014$
7.44	$40 \pm 6.3$	$5.38 \pm 0.85$	$0.90 \pm 0.14$	$0.120 \pm 0.019$
4.29	$34 \pm 5.8$	$7.93 \pm 1.36$	$0.76 \pm 0.13$	$0.175 \pm 0.031$
2.76	$23 \pm 4.8$	$8.34 \pm 1.75$	$0.52 \pm 0.11$	$0.187 \pm 0.039$
2.75	$25 \pm 5.0$	$9.08 \pm 1.82$	$0.56 \pm 0.11$	$0.203 \pm 0.041$
1.56	$15 \pm 3.9$	$9.59 \pm 2.52$	$0.34 \pm 0.09$	$0.215 \pm 0.057$

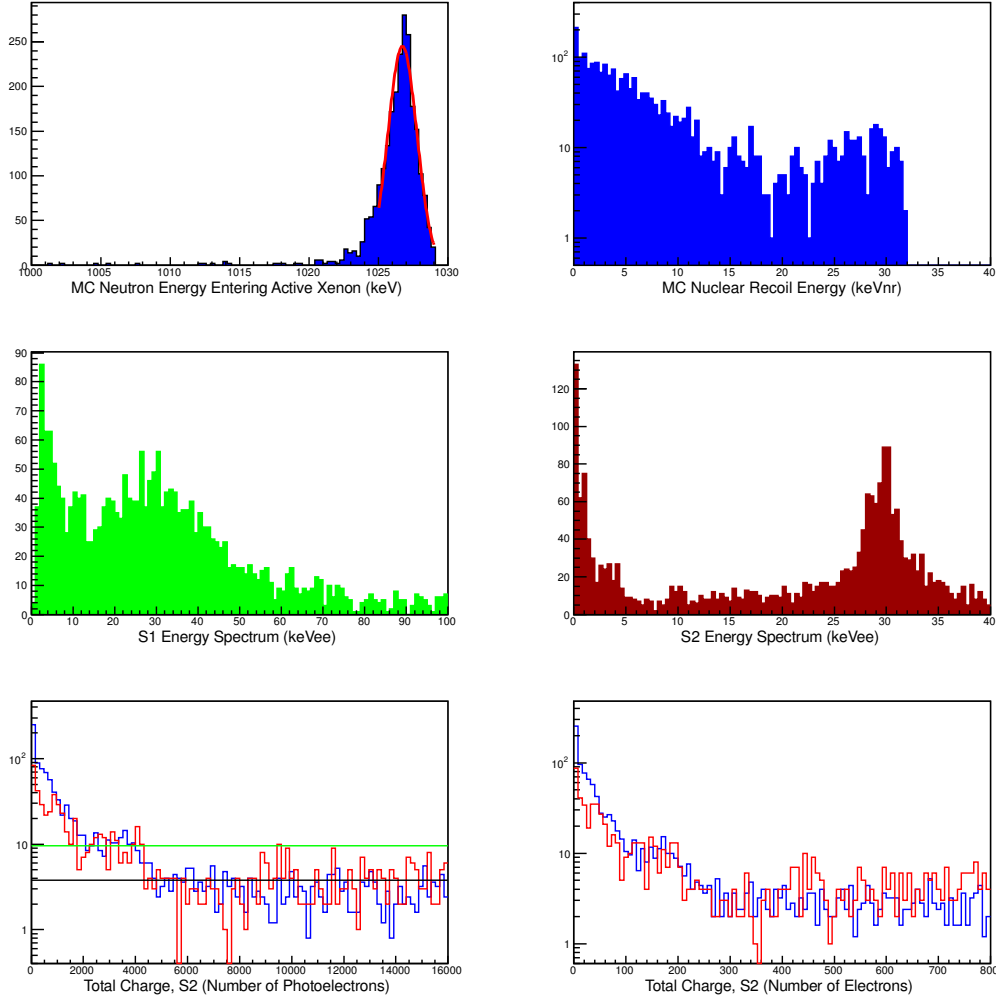


Figure 5.3: Summary plots for 31.55 keVnr. The *top left* plot shows the energy spectrum of the neutrons that enter the active xenon volume according to the MC simulation, with a Gaussian fit (*red curve*). The *top right* is the single scatter, un-smeared nuclear recoil energy (keVnr) from the MC simulation. The *middle left* plot is the energy spectrum of the data from the S1 light only, where the conversion of 2.29 pes/keV was used. The *middle right* is the raw S2 energy spectrum of the data in electron equivalent energy (keVee) after all software cuts. The *lower left* is the low energy region of the S2 pe spectrum (*red* is data, *blue* is the scaled, smeared MC) with the average background from the data indicated by the *black line* and the  $3\sigma$  level above the background indicated by the *green line*. The *lower right* shows the number of counted electrons (*red* is data, *blue* is the scaled, smeared MC).

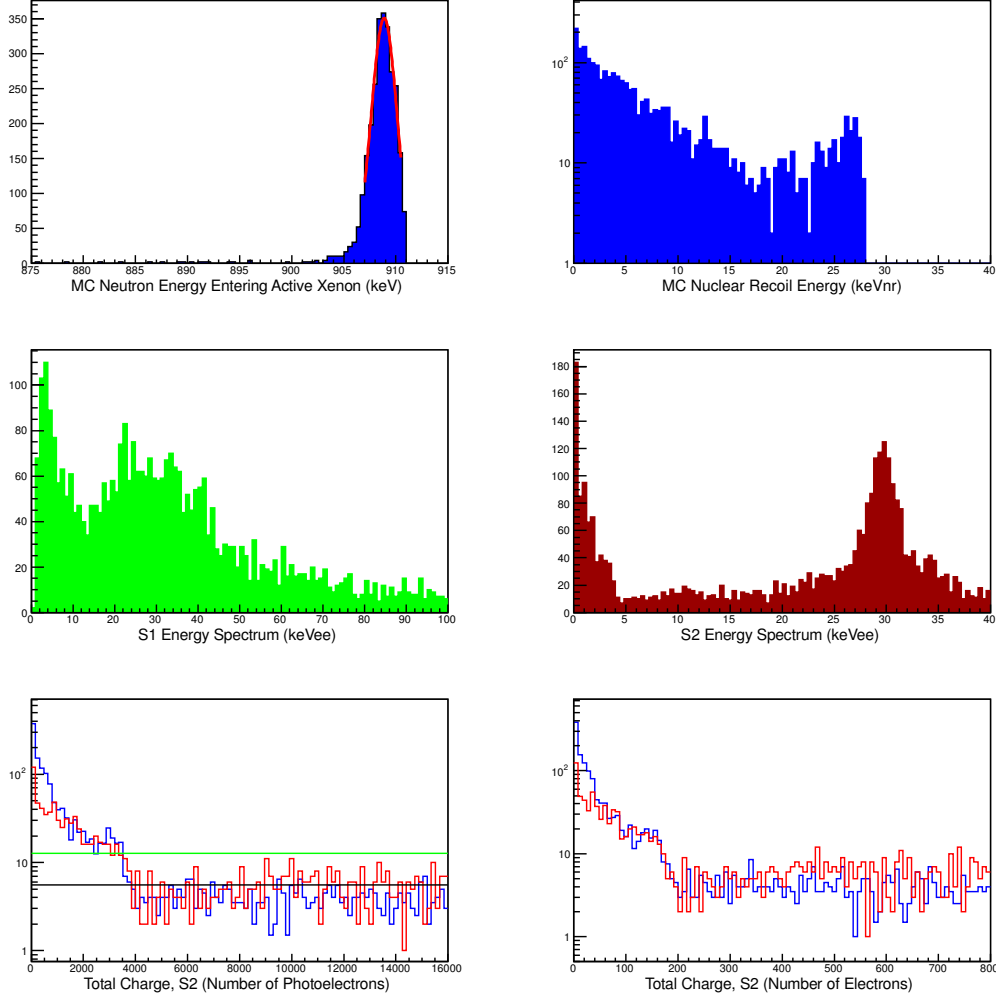


Figure 5.4: Summary plots for 27.93 keVnr. The *top left* plot shows the energy spectrum of the neutrons that enter the active xenon volume according to the MC simulation, with a Gaussian fit (*red curve*). The *top right* is the single scatter, un-smeared nuclear recoil energy (keVnr) from the MC simulation. The *middle left* plot is the energy spectrum of the data from the S1 light only, where the conversion of 2.29 pes/keV was used. The *middle right* is the raw S2 energy spectrum of the data in electron equivalent energy (keVee) after all software cuts. The *lower left* is the low energy region of the S2 pe spectrum (*red* is data, *blue* is the scaled, smeared MC) with the average background from the data indicated by the *black line* and the  $3\sigma$  level above the background indicated by the *green line*. The *lower right* shows the number of counted electrons (*red* is data, *blue* is the scaled, smeared MC).



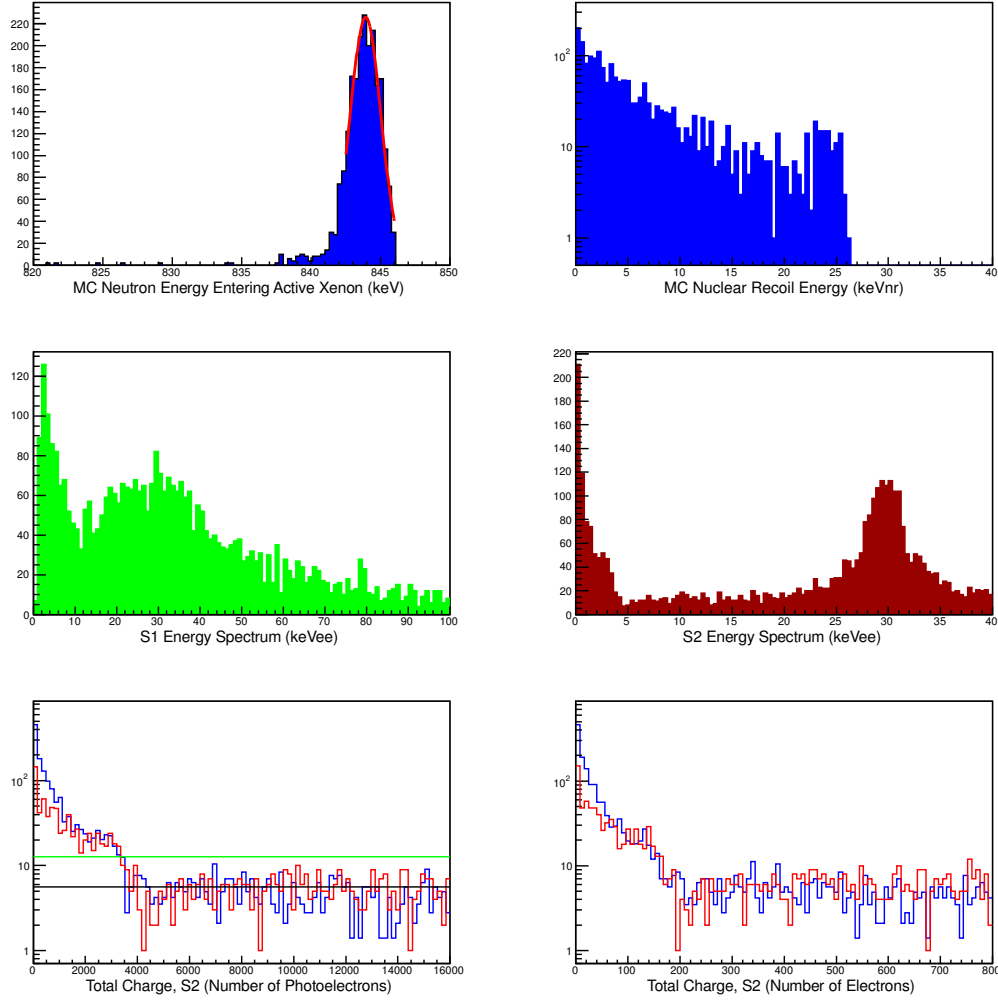


Figure 5.5: Summary plots for 25.93 keVnr. The *top left* plot shows the energy spectrum of the neutrons that enter the active xenon volume according to the MC simulation, with a Gaussian fit (*red curve*). The *top right* is the single scatter, un-smeared nuclear recoil energy (keVnr) from the MC simulation. The *middle left* plot is the energy spectrum of the data from the S1 light only, where the conversion of 2.29 pes/keV was used. The *middle right* is the raw S2 energy spectrum of the data in electron equivalent energy (keVee) after all software cuts. The *lower left* is the low energy region of the S2 pe spectrum (*red* is data, *blue* is the scaled, smeared MC) with the average background from the data indicated by the *black line* and the  $3\sigma$  level above the background indicated by the *green line*. The *lower right* shows the number of counted electrons (*red* is data, *blue* is the scaled, smeared MC).

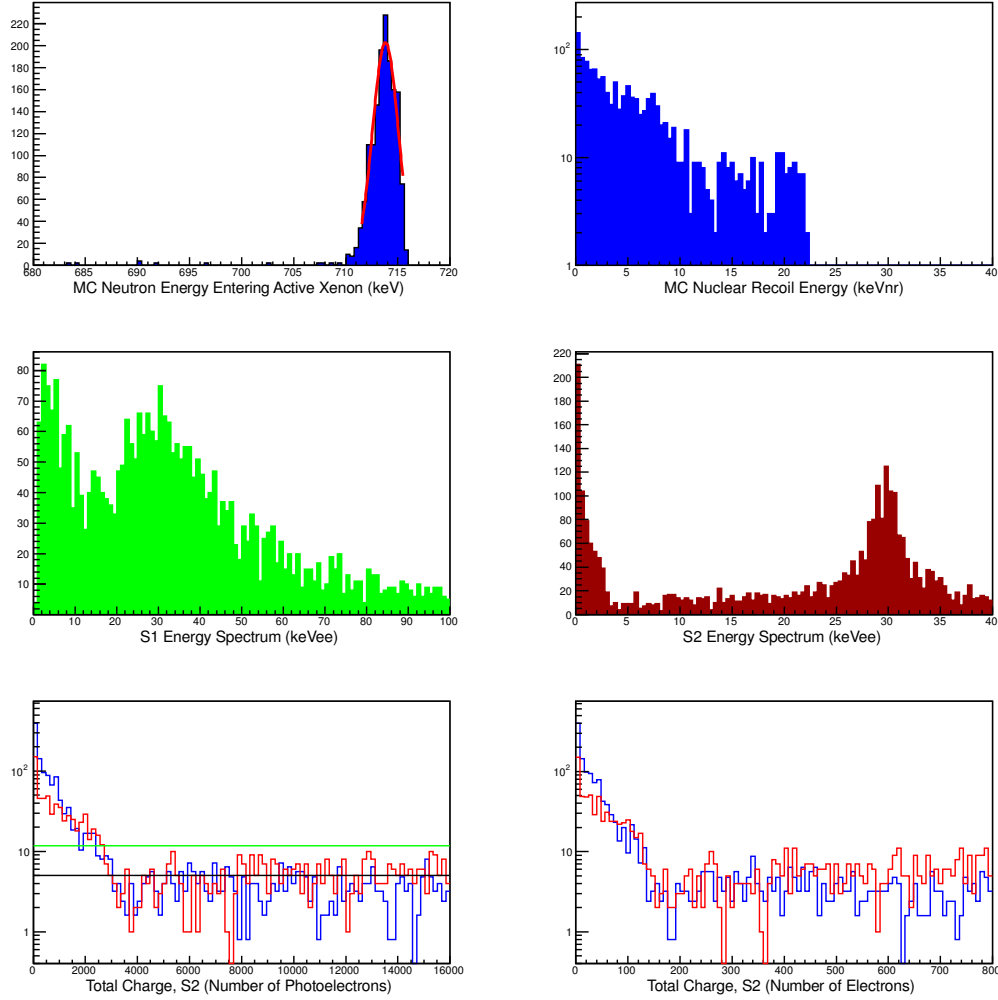


Figure 5.6: Summary plots for 21.93 keVnr. The *top left* plot shows the energy spectrum of the neutrons that enter the active xenon volume according to the MC simulation, with a Gaussian fit (*red curve*). The *top right* is the single scatter, un-smeared nuclear recoil energy (keVnr) from the MC simulation. The *middle left* plot is the energy spectrum of the data from the S1 light only, where the conversion of 2.29 pes/keV was used. The *middle right* is the raw S2 energy spectrum of the data in electron equivalent energy (keVee) after all software cuts. The *lower left* is the low energy region of the S2 pe spectrum (*red* is data, *blue* is the scaled, smeared MC) with the average background from the data indicated by the *black line* and the  $3\sigma$  level above the background indicated by the *green line*. The *lower right* shows the number of counted electrons (*red* is data, *blue* is the scaled, smeared MC).

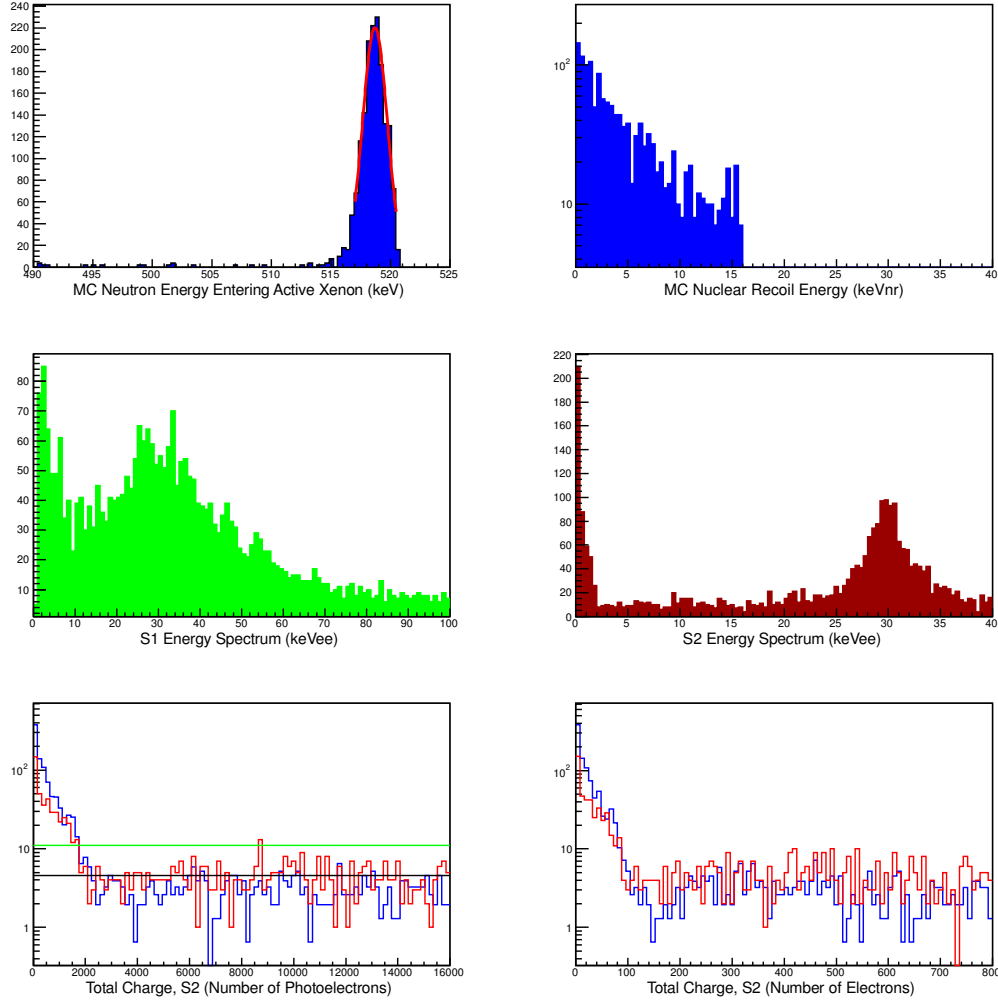


Figure 5.7: Summary plots for 15.94 keVnr. The *top left* plot shows the energy spectrum of the neutrons that enter the active xenon volume according to the MC simulation, with a Gaussian fit (*red curve*). The *top right* is the single scatter, un-smeared nuclear recoil energy (keVnr) from the MC simulation. The *middle left* plot is the energy spectrum of the data from the S1 light only, where the conversion of 2.29 pes/keV was used. The *middle right* is the raw S2 energy spectrum of the data in electron equivalent energy (keVee) after all software cuts. The *lower left* is the low energy region of the S2 pe spectrum (*red* is data, *blue* is the scaled, smeared MC) with the average background from the data indicated by the *black line* and the  $3\sigma$  level above the background indicated by the *green line*. The *lower right* shows the number of counted electrons (*red* is data, *blue* is the scaled, smeared MC).

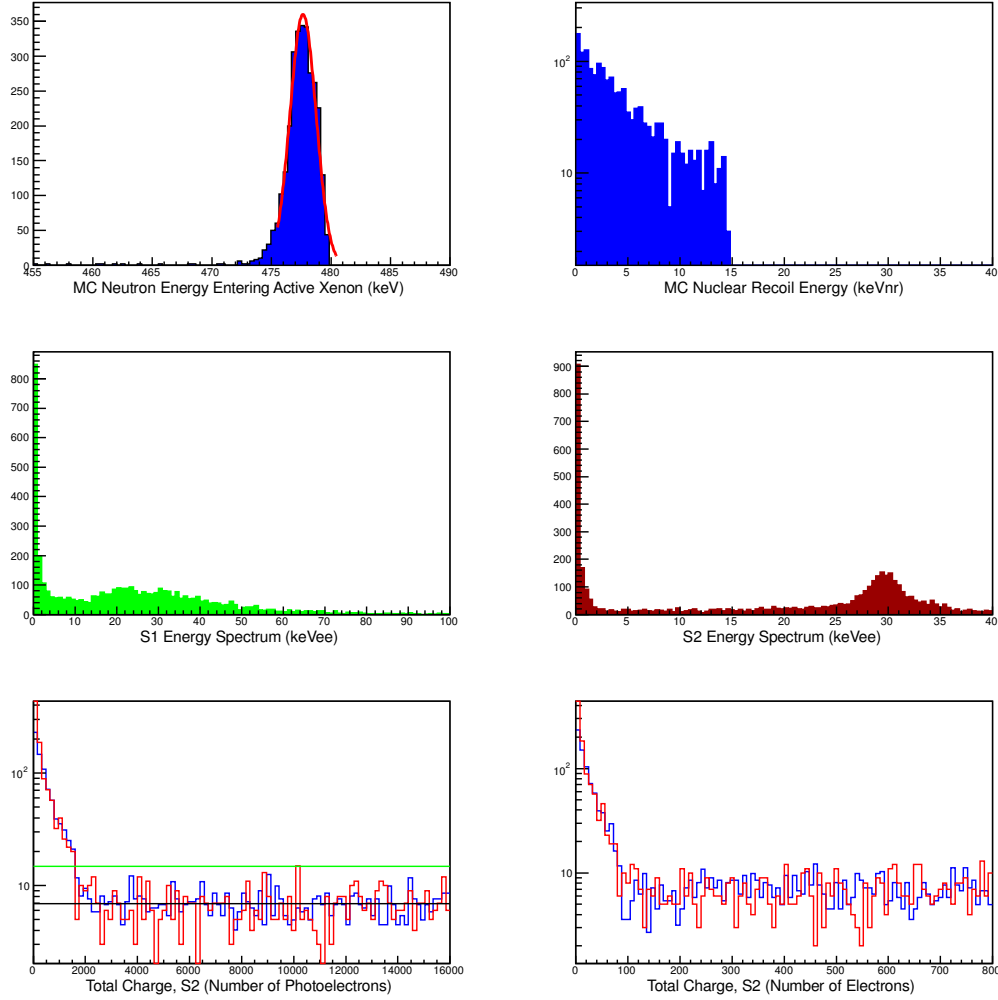


Figure 5.8: Summary plots for 14.68 keVnr. The *top left* plot shows the energy spectrum of the neutrons that enter the active xenon volume according to the MC simulation, with a Gaussian fit (*red curve*). The *top right* is the single scatter, un-smeared nuclear recoil energy (keVnr) from the MC simulation. The *middle left* plot is the energy spectrum of the data from the S1 light only, where the conversion of 2.29 pes/keV was used. The *middle right* is the raw S2 energy spectrum of the data in electron equivalent energy (keVee) after all software cuts. The *lower left* is the low energy region of the S2 pe spectrum (*red* is data, *blue* is the scaled, smeared MC) with the average background from the data indicated by the *black line* and the  $3\sigma$  level above the background indicated by the *green line*. The *lower right* shows the number of counted electrons (*red* is data, *blue* is the scaled, smeared MC).

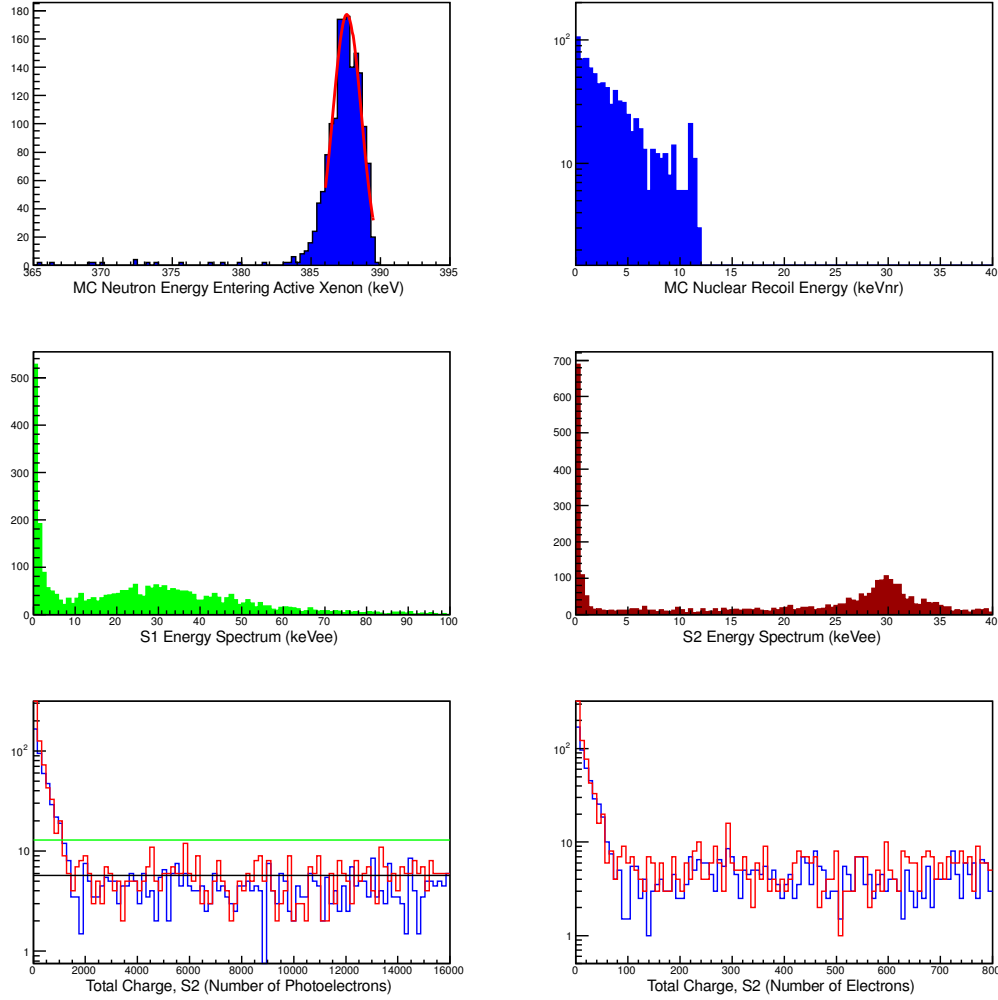


Figure 5.9: Summary plots for 11.91 keVnr. The *top left* plot shows the energy spectrum of the neutrons that enter the active xenon volume according to the MC simulation, with a Gaussian fit (*red curve*). The *top right* is the single scatter, un-smeared nuclear recoil energy (keVnr) from the MC simulation. The *middle left* plot is the energy spectrum of the data from the S1 light only, where the conversion of 2.29 pes/keV was used. The *middle right* is the raw S2 energy spectrum of the data in electron equivalent energy (keVee) after all software cuts. The *lower left* is the low energy region of the S2 pe spectrum (*red* is data, *blue* is the scaled, smeared MC) with the average background from the data indicated by the *black line* and the  $3\sigma$  level above the background indicated by the *green line*. The *lower right* shows the number of counted electrons (*red* is data, *blue* is the scaled, smeared MC).

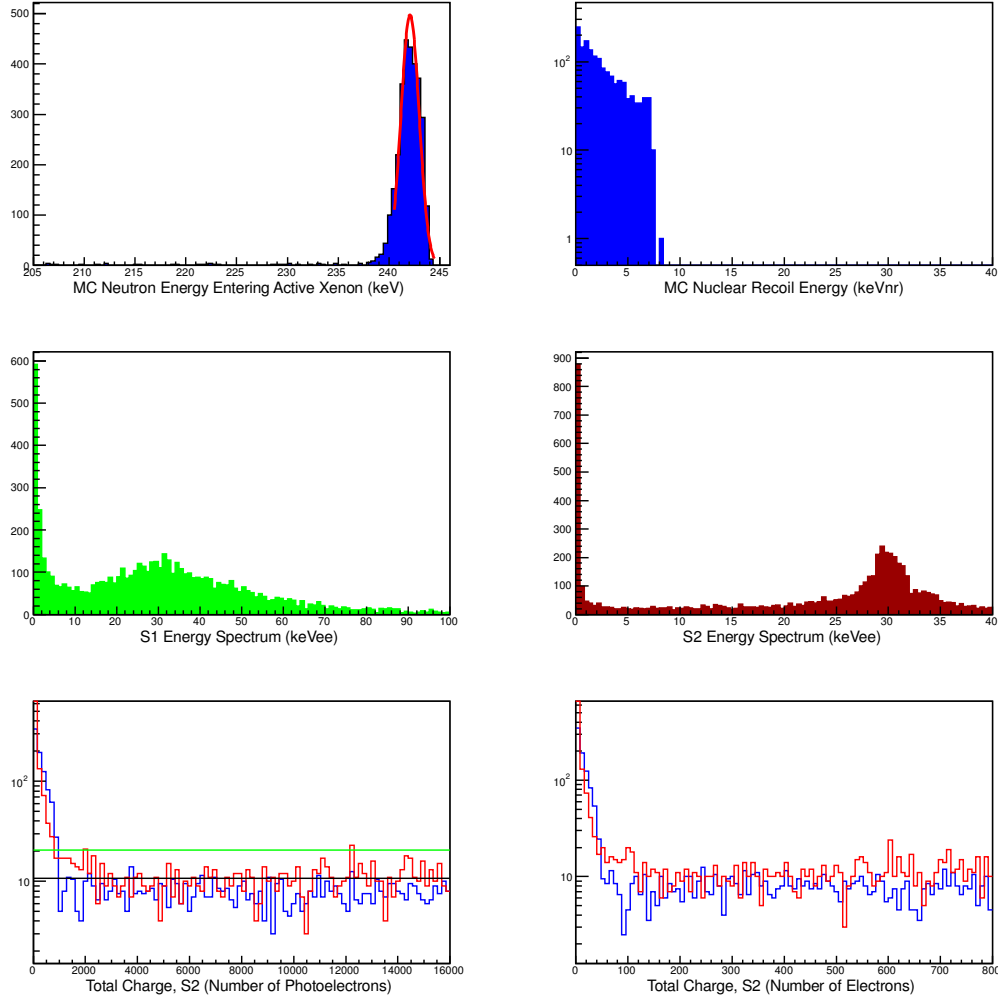


Figure 5.10: Summary plots for 7.44 keVnr. The *top left* plot shows the energy spectrum of the neutrons that enter the active xenon volume according to the MC simulation, with a Gaussian fit (*red curve*). The *top right* is the single scatter, un-smeared nuclear recoil energy (keVnr) from the MC simulation. The *middle left* plot is the energy spectrum of the data from the S1 light only, where the conversion of 2.29 pes/keV was used. The *middle right* is the raw S2 energy spectrum of the data in electron equivalent energy (keVee) after all software cuts. The *lower left* is the low energy region of the S2 pe spectrum (*red* is data, *blue* is the scaled, smeared MC) with the average background from the data indicated by the *black line* and the  $3\sigma$  level above the background indicated by the *green line*. The *lower right* shows the number of counted electrons (*red* is data, *blue* is the scaled, smeared MC).

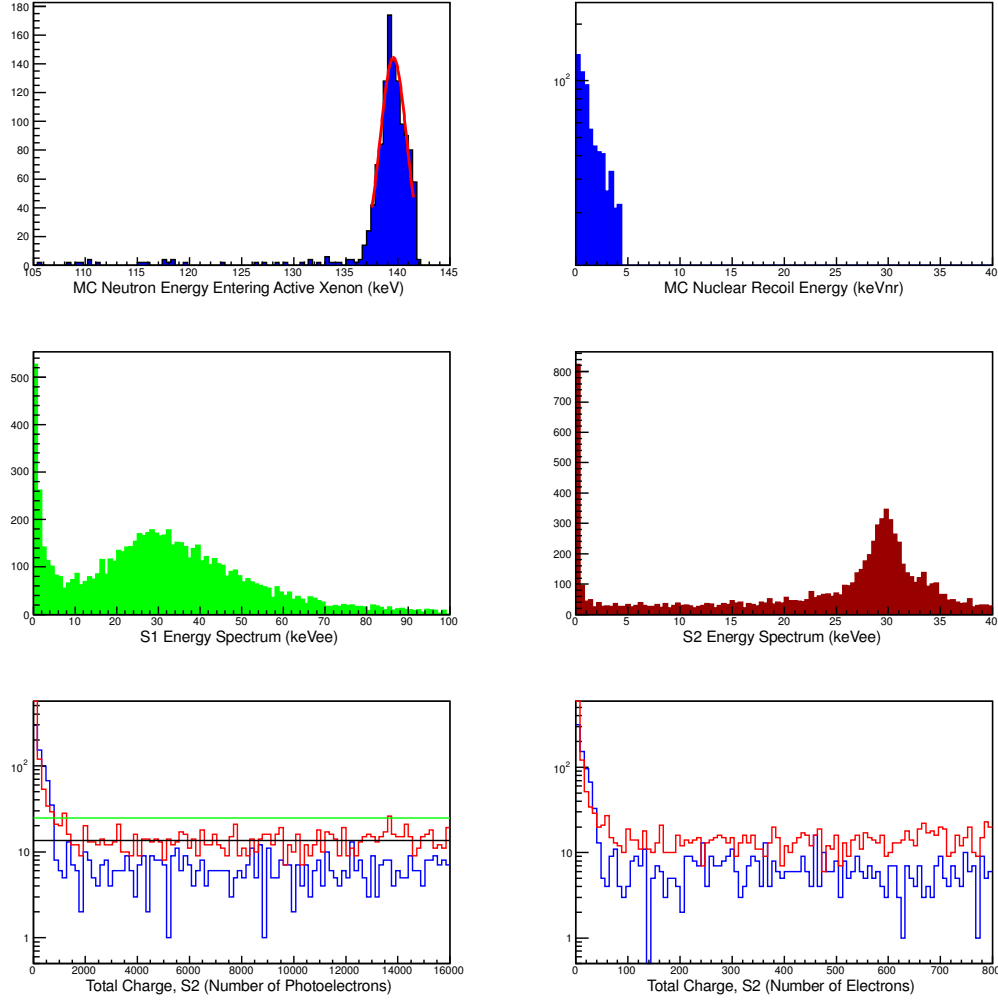


Figure 5.11: Summary plots for 4.29 keVnr. The *top left* plot shows the energy spectrum of the neutrons that enter the active xenon volume according to the MC simulation, with a Gaussian fit (*red curve*). The *top right* is the single scatter, un-smeared nuclear recoil energy (keVnr) from the MC simulation. The *middle left* plot is the energy spectrum of the data from the S1 light only, where the conversion of 2.29 pes/keV was used. The *middle right* is the raw S2 energy spectrum of the data in electron equivalent energy (keVee) after all software cuts. The *lower left* is the low energy region of the S2 pe spectrum (*red* is data, *blue* is the scaled, smeared MC) with the average background from the data indicated by the *black line* and the  $3\sigma$  level above the background indicated by the *green line*. The *lower right* shows the number of counted electrons (*red* is data, *blue* is the scaled, smeared MC).

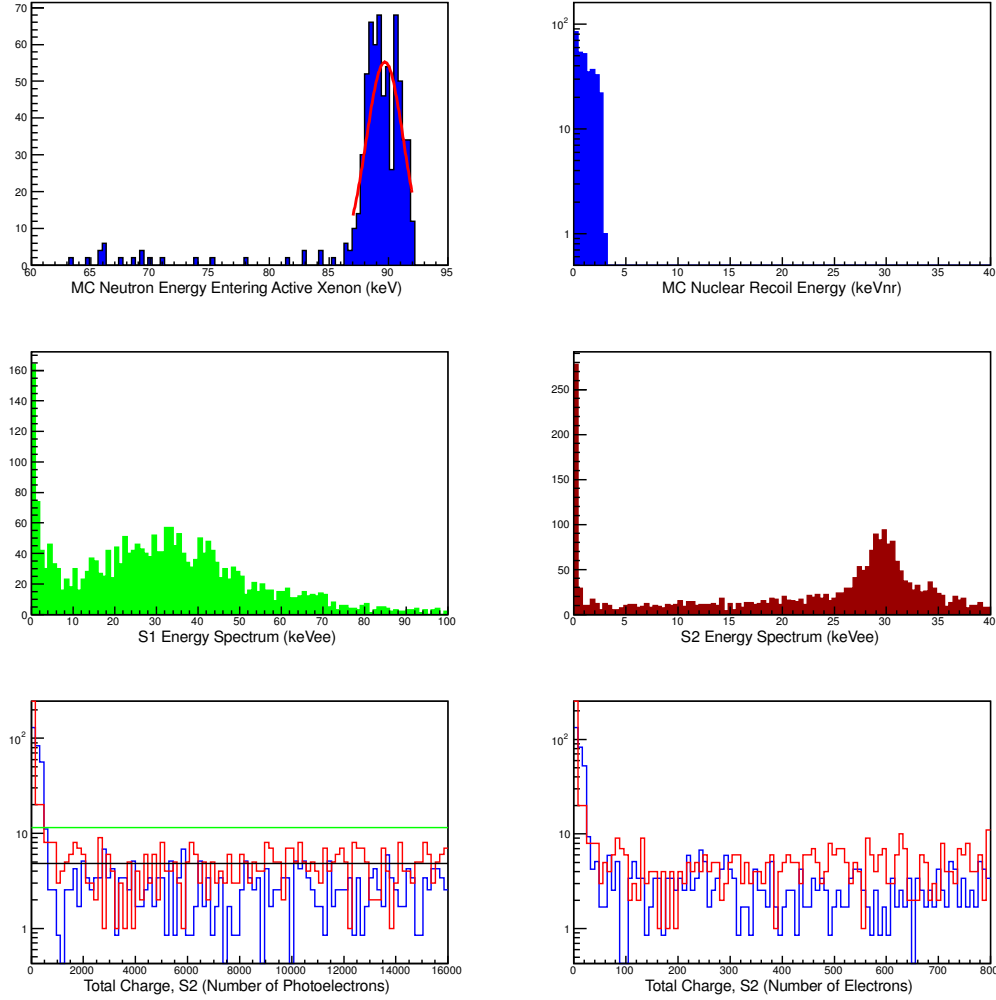


Figure 5.12: Summary plots for 2.76 keVnr. The *top left* plot shows the energy spectrum of the neutrons that enter the active xenon volume according to the MC simulation, with a Gaussian fit (*red curve*). The *top right* is the single scatter, un-smeared nuclear recoil energy (keVnr) from the MC simulation. The *middle left* plot is the energy spectrum of the data from the S1 light only, where the conversion of 2.29 pes/keV was used. The *middle right* is the raw S2 energy spectrum of the data in electron equivalent energy (keVee) after all software cuts. The *lower left* is the low energy region of the S2 pe spectrum (*red* is data, *blue* is the scaled, smeared MC) with the average background from the data indicated by the *black line* and the  $3\sigma$  level above the background indicated by the *green line*. The *lower right* shows the number of counted electrons (*red* is data, *blue* is the scaled, smeared MC).



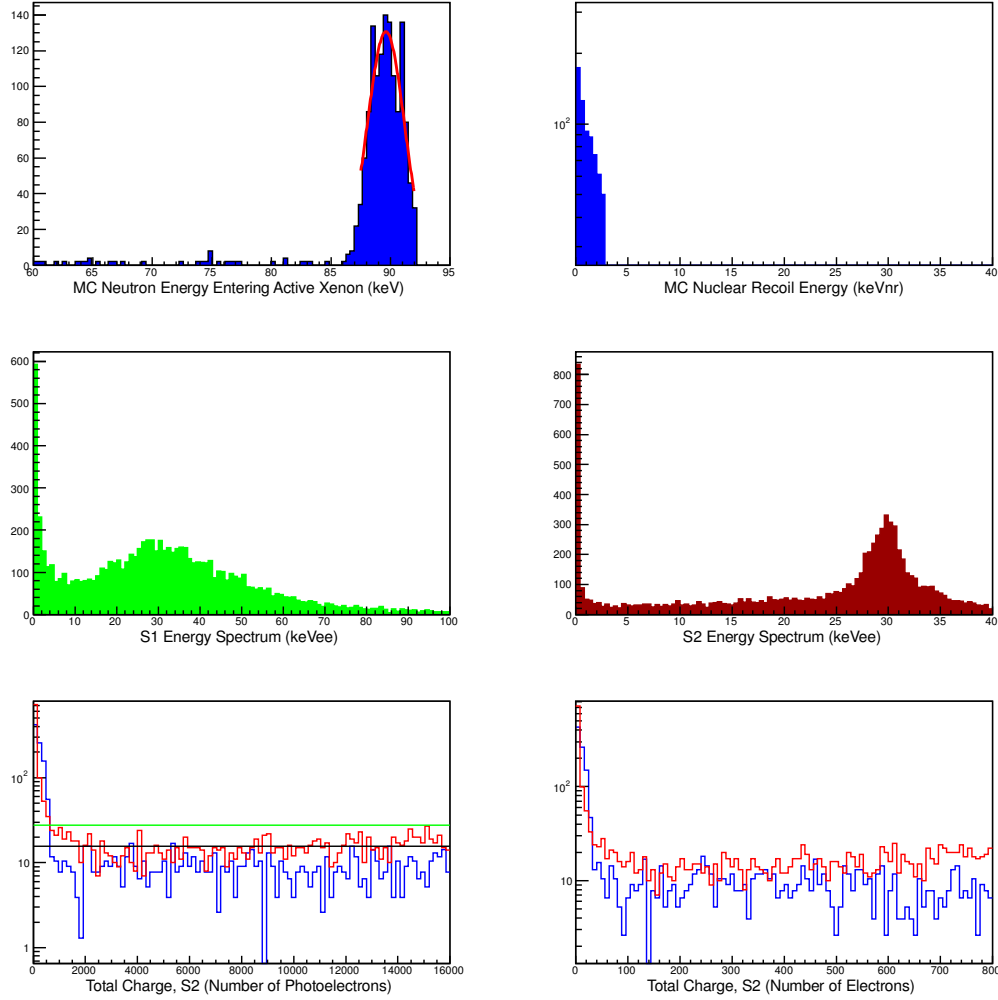


Figure 5.13: Summary plots for 2.75 keVnr. The *top left* plot shows the energy spectrum of the neutrons that enter the active xenon volume according to the MC simulation, with a Gaussian fit (*red curve*). The *top right* is the single scatter, un-smeared nuclear recoil energy (keVnr) from the MC simulation. The *middle left* plot is the energy spectrum of the data from the S1 light only, where the conversion of 2.29 pes/keV was used. The *middle right* is the raw S2 energy spectrum of the data in electron equivalent energy (keVee) after all software cuts. The *lower left* is the low energy region of the S2 pe spectrum (*red* is data, *blue* is the scaled, smeared MC) with the average background from the data indicated by the *black line* and the  $3\sigma$  level above the background indicated by the *green line*. The *lower right* shows the number of counted electrons (*red* is data, *blue* is the scaled, smeared MC).

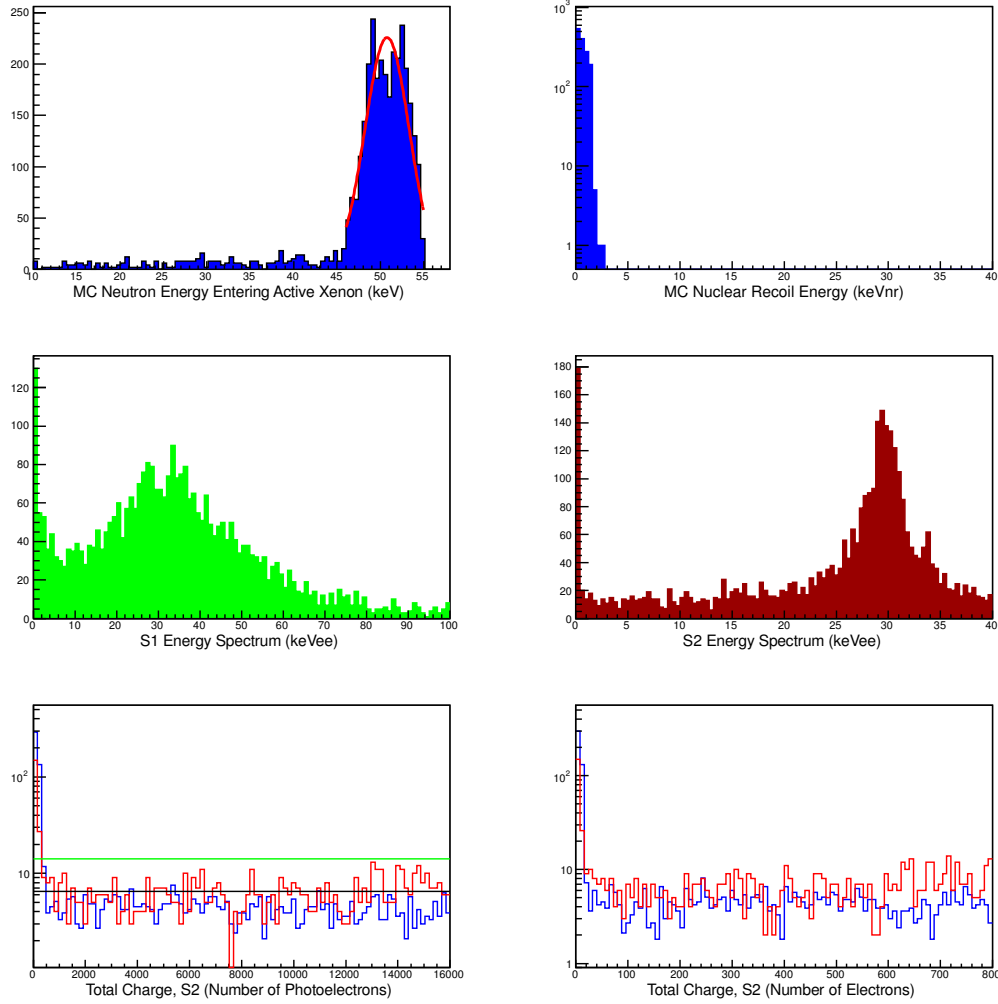


Figure 5.14: Summary plots for 1.56 keVnr. The *top left* plot shows the energy spectrum of the neutrons that enter the active xenon volume according to the MC simulation, with a Gaussian fit (*red curve*). The *top right* is the single scatter, un-smeared nuclear recoil energy (keVnr) from the MC simulation. The *middle left* plot is the energy spectrum of the data from the S1 light only, where the conversion of 2.29 pes/keV was used. The *middle right* is the raw S2 energy spectrum of the data in electron equivalent energy (keVee) after all software cuts. The *lower left* is the low energy region of the S2 pe spectrum (*red* is data, *blue* is the scaled, smeared MC) with the average background from the data indicated by the *black line* and the  $3\sigma$  level above the background indicated by the *green line*. The *lower right* shows the number of counted electrons (*red* is data, *blue* is the scaled, smeared MC).

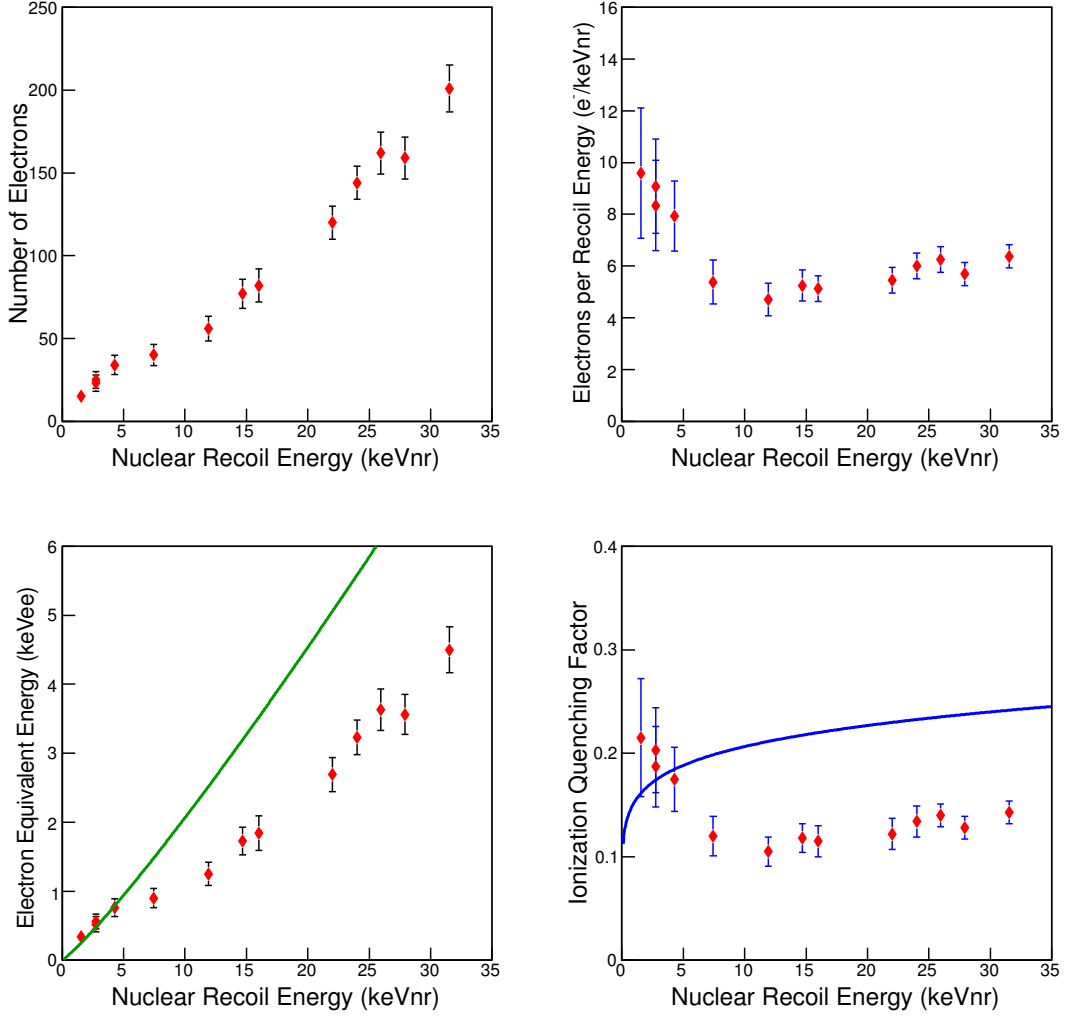


Figure 5.15: Results from all nuclear recoil data runs plotted as a function of  $E_r$  at a drift field of  $E_{drift} = 400$  V/cm. Error bars correspond to  $\pm 1\sigma$ . The statistical error in  $E_r$  is smaller than the width of the dots. The *top left* shows the total number of electrons, the *top right* shows the specific charge yield, the *bottom left* shows the electron equivalent energy and the *bottom right* shows the nuclear ionization quenching factor. The *green curve* indicates the expected electron equivalent energy (total energy given to electrons,  $\eta$ ) using the Lindhard nuclear quenching. The *blue curve* indicates the total nuclear quenching ( $f_n = kg/[1 + kg]$ ) from Lindhard.

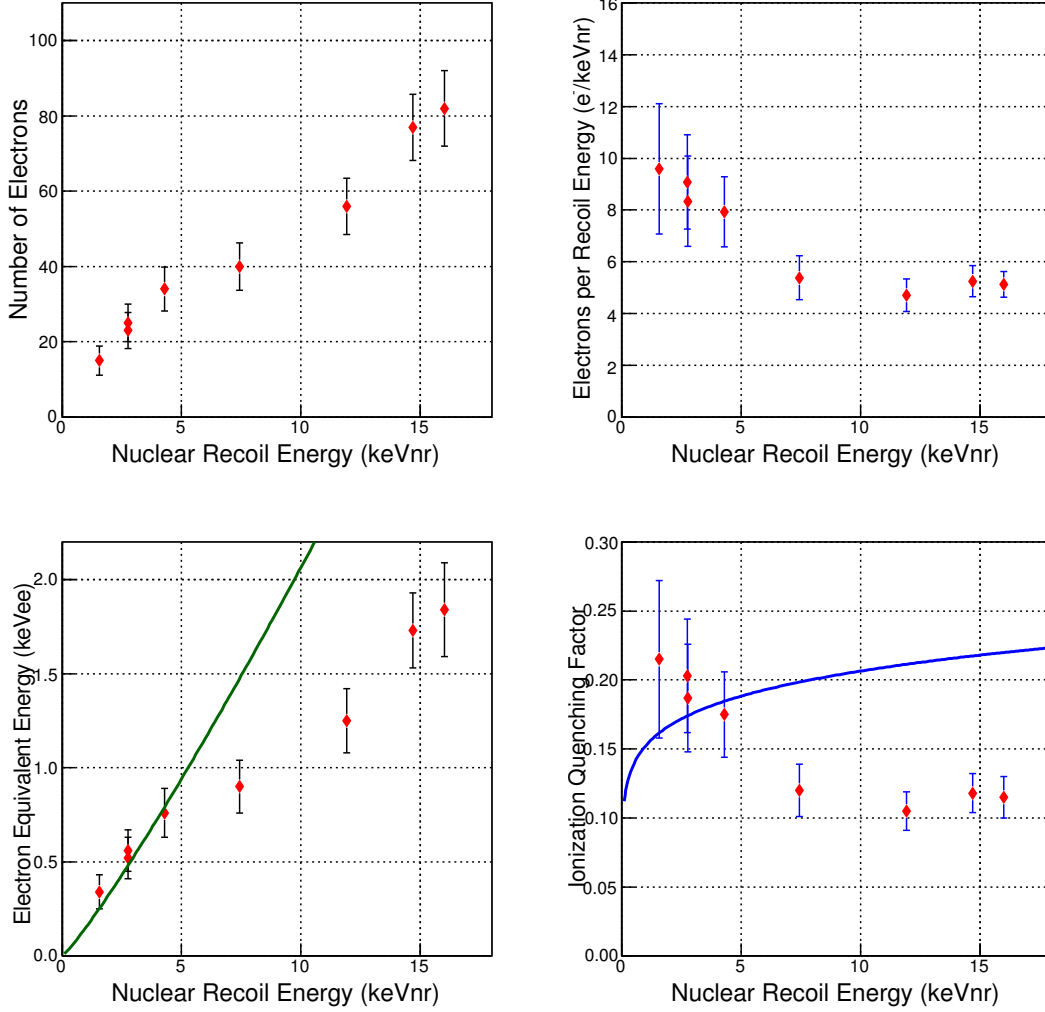


Figure 5.16: Results from the only S2-triggered nuclear recoil data runs plotted as a function of  $E_r$  at a drift field of  $E_{drift} = 400$  V/cm. Error bars correspond to  $\pm 1\sigma$ . The statistical error in  $E_r$  is smaller than the width of the dots. The *top left* shows the total number of electrons, the *top right* shows the specific charge yield, the *bottom left* shows the electron equivalent energy and the *bottom right* shows the nuclear ionization quenching factor. The *green curve* indicates the expected electron equivalent energy (total energy given to electrons,  $\eta$ ) using the Lindhard nuclear quenching. The *blue curve* indicates the total nuclear quenching ( $f_n = kg/[1 + kg]$ ) from Lindhard.

### 5.3 Error Propagation

The statistical errors were calculated in the standard way. For example, the statistical error in  $\mathcal{Q} = E_{ee}/E_r$  is:

$$\sigma_{\mathcal{Q}}^2 = \left( \frac{\partial \mathcal{Q}}{\partial E_{ee}} \right)^2 \sigma_{E_{ee}}^2 + \left( \frac{\partial \mathcal{Q}}{\partial E_{nr}} \right)^2 \sigma_{E_{nr}}^2 \quad (5.4)$$

After a simple substitution ( $\mathcal{Q}^2 = E_{ee}^2/E_r^2$ ), Eq. 5.4 is then written as:

$$\left( \frac{\sigma_{\mathcal{Q}}}{\mathcal{Q}} \right)^2 = \left( \frac{\sigma_{E_{ee}}}{E_{ee}} \right)^2 + \left( \frac{\sigma_{E_{nr}}}{E_{nr}} \right)^2 \quad (5.5)$$

The values for  $\sigma_{E_{nr}}$  were obtained from the Gaussian fit of the MC neutron spectrum. The  $\sigma_{E_{ee}}$  values were calculated in quadrature from the parameters in  $E_{ee} = \mathcal{E} W_{ion}$ :

$$\left( \frac{\sigma_{E_{ee}}}{E_{ee}} \right)^2 = \left( \frac{\sigma_{\mathcal{E}}}{\mathcal{E}} \right)^2 + \left( \frac{\sigma_{W_{ion}}}{W_{ion}} \right)^2 \quad (5.6)$$

where  $\sigma_{W_{ion}} = 0.5$  eV/ion and  $\sigma_{\mathcal{E}} = \sqrt{\mathcal{E}}$ , since Poisson fluctuations were assumed.

Systematic errors were minimized by careful choice of an ultra-thin LiF target, narrow beam slits, periodic beam calibration, etc. There still exists the possibility of sizable errors, especially from unknown target properties and in the algorithm used to select the kinematic edge. A follow-on study is required to understand these errors in detail. For example, a dedicated MC study needs to be done with the kinematic edge search routine iterated over many gamma background scenarios. Also, these measurements need to be repeated using different target substrates (*e.g.* brass, SS, copper or solid LiF crystal with no substrate). Lastly, the  $W_{ion}$  value used for this work was chosen because it most closely matches the calibration energy used here. There is a possibility that the value does not apply to electron/x-ray energies  $\lesssim 4$

keVee. It may be totally wrong for nuclear recoil energy depositions. This further stresses the need to simply count electrons at these low nuclear recoil energies and not rely on a conversion from a gamma/x-ray line.

## 6. CONCLUSIONS

### 6.1 Low Energy Nuclear Recoils in HPXe

Nuclear recoil measurements were made in a HPXe TPC using a nearly mono-energetic neutron source. The recoil energy range presented here is 1.56 - 31.55 keV<sub>nr</sub>. The neutrons were produced by an accelerated beam of protons incident on a very thin layer of LiF via the  ${}^7\text{Li}(p,n){}^7\text{Be}$  reaction. Precise calibration of the proton beam to the neutron production threshold, coupled with extremely stable operating conditions, lead to neutrons entering the active xenon volume with  $\lesssim 5$  keV spread in kinetic energy, corresponding to  $\lesssim 10\%$  spread in each measured nuclear recoil energy. The nuclear recoil energies were selected for analysis by plotting the resulting S2 energy spectrum and searching for the kinematic cutoff energy caused by  $180^\circ$  elastic backscatters. This represents the most precise nuclear recoil measurements in xenon to date, and the only one of its kind in the gas phase.

If dark matter is indeed made up of low mass WIMPs ( $\lesssim 30$  GeV/ $c^2$ ), then the possibility exists for employing HPXe as a detector medium. The integrated event rate is shown in Fig. 6.1 for 5 - 15 GeV/ $c^2$  WIMP masses. The plot shows that WIMP masses as low as  $\sim 7$  GeV/ $c^2$  are accessible with the current nuclear recoil results, possibly even as low as 5 GeV/ $c^2$  or less with future improvements. Using a HPXe TPC represents a significantly smaller technical challenge in terms of both design and operation over similar cryogenic systems.

### 6.2 Electron Fraction

The goal of the experiment was to measure both the S1 and S2 signals simultaneously in order to test Lindhard's theory of nuclear quenching, especially at low recoil energies in xenon ( $E_{nr} \lesssim 3$  keV<sub>nr</sub>). The simultaneous measurement of S1 and

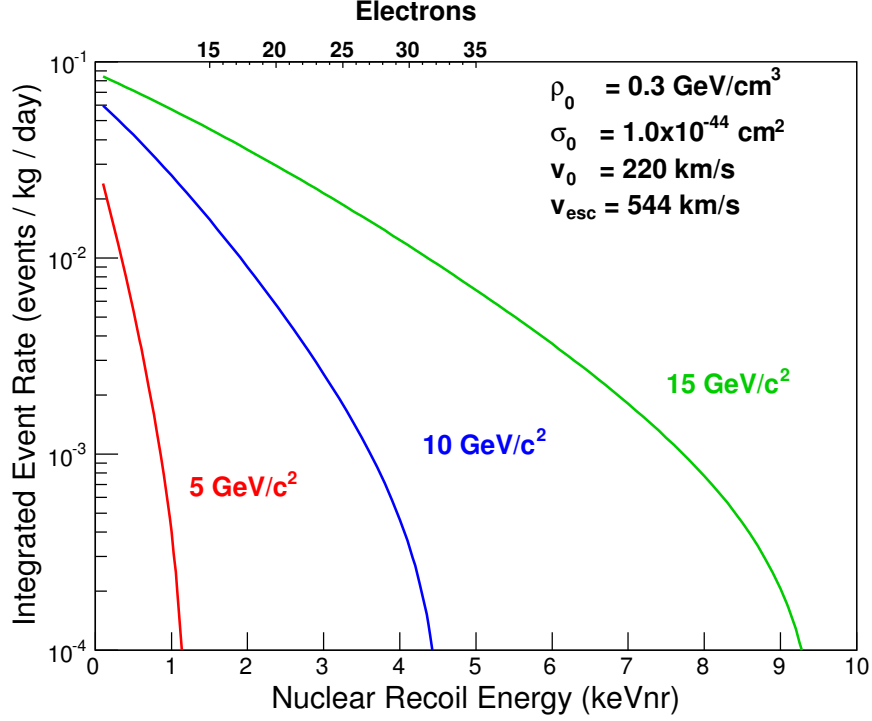


Figure 6.1: Integrated event rates for spin-independent WIMP-nucleus elastic scattering in xenon for a common set of cosmological parameters. The bottom horizontal scale is the nuclear recoil energy (keVnr) and the partial scale shown on top is the  $\sim$ linear electron response region measured in this work.

S2 is the only direct probe of nuclear quenching in a TPC. The S2 energy spectrum was very well resolved with easily manageable background rejection. However, the S1 energy spectrum was too poorly resolved to employ a similar kinematic edge finding routine. The edge could be seen by eye in the S1 data, but a non-biased method could not be developed on the current data set. Also, the variation in the S1 signal with the corresponding S2 edge events was very large. This is unlike the well-behaved S1/S2 anti-correlation of the higher density LXe. Dedicated Monte Carlo studies are required to study the S1 response at energies  $\lesssim 10$  keVnr and correlate it to an expected S2. As a result, the focus of this work was on measuring only the



charge yield at very low recoil energies. The results show that at a very high EL gain ( $\sim 200$  photons/ $e^-$ ), a moderate drift field ( $E_{drift} = 400$  V/cm) and very high light collection efficiency ( $\sim 21$  photoelectrons/ $e^-$ ), it is possible to both trigger on and count single electrons to provide the necessary calorimetry at very low energies in HPXe.

There is still some qualitative theoretical insight gained in the measurement of only the charge. For  $E_r \gtrsim 10$  keVnr, the overall trend in the energy given to electrons ( $\eta$ ) follows a shape similar to the one predicted by Lindhard's theory. The fact that the nuclear ionization quenching factor ( $\mathcal{Q}$ ) is about half the total Lindhard quenching suggests that there is roughly equal sharing of a nuclear recoil's energy dissipation between primary scintillation photons and liberated charge. As  $E_r$  goes down, the fraction of the recoil energy shared between photons and electrons shifts, with the electrons seemingly receiving more than half of  $\eta$ . This continues until  $\mathcal{Q} \approx f_n$ , where nearly all of  $\eta$  is given to ionization with little to no recombination of the charge. This is roughly consistent with measurements in LXe discussed above. (See [139] and references therein.) This makes sense from the standpoint of overall charge density. At lower energies, the density of electron/ion pairs is lower, but the electric drift field remains the same. Thus, the probability of an electron escaping the interaction site, via the external electric field, is higher.

On the one hand, the Lindhard curve (green line in the lower left plot of Fig. 5.16) goes through the  $1\sigma$  error bars of the data, suggesting that the theory is well-matched to the data based on charge alone. On the other hand, the trend of the mean values of  $\mathcal{Q}$  and  $f_n$  are anti-correlated at  $E_r \lesssim 5$  keVnr. This could mean that the recoiling atom does not have sufficient energy to overcome the Coulomb repulsion of the respective atomic electron clouds to allow for nucleus-nucleus interactions (*i.e.* transfer of heat). Therefore, it is possible that the nuclear stopping power is going

down faster than predicted. Where, and how fast, this occurs will be the subject of future investigations.

### 6.3 Future Prospects for HPXe in Other Rare Event Searches

The added advantage of a HPXe TPC is the possibility of operating in two modes of rare event search: the search for dark matter and the detection of neutrinoless double beta decay ( $0\nu\beta\beta$ ) [160]. The dynamic range required for dual-mode operation is very large since the region of interest (ROI) for dark matter is in the few keV range and the  $Q_{\beta\beta}=2.458$  MeV for  $0\nu\beta\beta$ . However, operational settings (*e.g.* drift field and high EL gain), gas purity and material radiopurity requirements are nearly identical. The major difference between the two modes is in event tracking. To remain competitive in  $0\nu\beta\beta$  decay detection, a HPXe TPC must retain the superior background rejection advantage of extremely precise 3d event track reconstruction. To accomplish this, Silicon Photomultipliers (SiPMs) are used. These tiny (*e.g.* 1 mm  $\times$  1 mm square) sensors are usually densely spaced at the EL plane in place of traditional PMTs. The amount of S1 and S2 light generated at the  $Q_{\beta\beta}$  is enormous compared to the low mass WIMP search ROI, so the light lost in using the SiPMs is acceptable. PMTs are still used for calorimetry at the “cathode end” of an asymmetric TPC. The low mass WIMP search, on the other hand, requires the collection of every available photon. Thus, the only means of operating in both modes simultaneously is to design a hybrid light collection scenario. The best scenario, in the author’s opinion, is a symmetric TPC, with the cathode in the middle (z-position) of the chamber and a drift region on both sides. The EL planes on both ends would have to be instrumented with both PMTs and SiPMs in a hybrid configuration to what has been proposed in the past, offering large solid angle coverage by the PMTs and sufficient “pixelation” by the SiPMs in each plane. One example configuration

would be to mount the SiPMs on a clear substrate (*e.g.* synthetic fused silica or acrylic) coated with a wavelength shifter (*e.g.* tetraphenyl butadiene) placed very close to each anode grid plane. The PMTs could then be placed directly behind the clear SiPM mounting fixtures, even directly coupled to them optically. Further, the sparsified sensors may require more S2 light than the current demonstrated gains can offer; limited by electrostatics. The addition of a dielectric between each positively biased anode and the photosensors (similar to that shown in Ch. 4 above) may offer the necessary boost in S2 light. As a result, both the sub-cm tracking and the nearly intrinsic energy resolution required for  $0\nu\beta\beta$  decay, as well as the electron counting ability required for low mass WIMP search can be realized simultaneously.

Future work in our group includes the further investigation of HPXe for both low energy nuclear recoils and  $0\nu\beta\beta$  decay. Additionally, we plan to use the unique proton beam/LiF target setup to study low energy nuclear recoils in a previously studied NaI(Tl) crystal [161] and expand the measurements to include LXe and other high pressure noble gases and liquids.

## BIBLIOGRAPHY

- [1] E. Hubble and M. L. Humason, *Ap. J.* **74**, 43 (1931).
- [2] F. Zwicky, *Helv. Phys. Acta.* **6**, 208 (1933).
- [3] J. C. Kapteyn, *Ap. J.* **55**, 302 (1922).
- [4] V. Rubin and W. K. Ford, *Ap. J.* **159**, 379 (1970).
- [5] M. S. Roberts and A. H. Rots, *Astron. Astrophys.* **26**, 483 (1973).
- [6] Y. Sofue and V. Rubin, *Annu. Rev. Astron. Astrophys.* **39**, 137 (2001).
- [7] P. Salucci and M. Persic, *ASP Conf. Ser.* **117**, 1 (1997).
- [8] S. M. Faber and J. S. Gallagher, *Annu. Rev. Astron. Astrophys.* **17**, 135 (1979).
- [9] I. R. King, *Ap. J. Lett.* **174**, L123 (1972).
- [10] F. D. A. Hartwick and W. L. W. Sargent, *Ap. J.* **221**, 512 (1978).
- [11] R. Bacon et al., *MNRAS* **326**, 23 (2001).
- [12] V. C. Rubin, W. K. Ford Jr., and N. Thonnard, *Ap. J. Lett.* **225**, L107 (1978).
- [13] K. C. Freeman, *Ap. J.* **160**, 811 (1970).
- [14] T. S. van Albada, J. N. Bahcall, K. Begeman, and S. R., *Ap. J.* **295**, 305 (1985).
- [15] J. Einasto (2010), [arXiv:0901.0632v2](https://arxiv.org/abs/0901.0632v2).
- [16] J. F. Navarro, S. D. Frenk, and S. D. White, *Ap. J.* **462**, 563 (1996).

- [17] B. Willman, M. R. Blanton, A. A. West, J. J. Dalcanton, D. W. Hogg, D. P. Schneider, N. Wherry, B. Yanny, and J. Brinkmann, *Ap. J.* **129**, 2692 (2005).
- [18] D. H. Jones et al., *MNRAS* **399**, 683 (2009).
- [19] H. Jerjen, *Adv. Astron.* **2010**, 434390 (2010).
- [20] M. G. Walker, M. Mateo, E. W. Olszeski, O. Y. Gnedin, X. Wang, B. Sen, and M. Woodroffe, *Ap. J. Lett.* **667**, L53 (2007).
- [21] J. D. Simon and M. Geha, *Ap. J.* **670**, 313 (2007).
- [22] J. Bullock, M. Kaplinghat, and L. Strigari, in *Particle Dark Matter: Observations, Models and Searches*, edited by G. Bertone (Cambridge University Press, Cambridge, UK, 2010), chap. 3, pp. 38–55.
- [23] L. E. Strigari, J. S. Bullock, M. Kaplinghat, J. D. Simon, M. Geha, B. Willman, and M. G. Walker, *Nature* **454**, 1096 (2008).
- [24] M. Mateo, E. W. Olszewski, C. Pryor, D. L. Welch, and P. Fischer, *Ap. J.* **105**, 510 (1993).
- [25] M. Cappellari and E. Emsellem, *PASP* **116**, 138 (2004).
- [26] M. Sarzi et al., *MNRAS* **366**, 1151 (2006).
- [27] J. J. Bochanski, A. Munn, Jeffrey, S. L. Hawley, A. A. West, K. R. Covey, and D. P. Schneider, *Ap. J.* **134**, 2418 (2007).
- [28] D. Thomas et al., *MNRAS* **431**, 1383 (2013).
- [29] M. A. C. Perryman, K. S. de Boer, G. Gilmore, E. Høg, M. G. Lattanzi, L. Lindegren, X. Luri, F. Mignard, O. Pace, and P. T. de Zeeuw, *Astron. Astrophys.* **369**, 339 (2001).

- [30] C. J. Conselice, in *Near-Field Cosmology with Dwarf Elliptical Galaxies* (IAU Colloquium, Les Diablerets, Switzerland, 2005).
- [31] J. S. Gallagher, C. J. Conselice, and R. F. G. Wyse (2001), [arXiv:astro-ph/0108007v1](#).
- [32] Submitted to A & A **Planck Collaboration XVI** (2013).
- [33] A. G. Riess et al. (2011), [arXiv:1103.2976v1\[astro-ph.CO\]](#).
- [34] E. Komatsu et al., *Ap. J. S.* **192**, 18 (2011).
- [35] M. Milgrom, *Ap. J.* **270**, 365 (1983).
- [36] J. D. Bekenstein, *Phys. Rev. D* **70**, 083509 (2004).
- [37] J. Richard, J.-P. Kneib, M. Limousin, A. Edge, and E. Jullo, *MNRAS* **402**, L44 (2010).
- [38] Y. Mellier, in *Particle Dark Matter: Observations, Models and Searches*, edited by G. Bertone (Cambridge University Press, Cambridge, UK, 2010), chap. 4, pp. 56–82.
- [39] R. Massey, T. Kitching, and J. Richard (2010), [arXiv:1001.1739v2\[astro-ph.CO\]](#).
- [40] P. Magain and V. Chantry (2013), [arXiv:1303.6896v1\[astro-ph.CO\]](#).
- [41] A. Taylor et al., *MNRAS* **353**, 1176 (2004).
- [42] M. Markevitch et al., *Bullet cluster composite image*, <http://chandra.harvard.edu/photo/2006/1e0657/> (Accessed January 2014).

- [43] D. Clowe, M. Bradac, A. H. Gonzalez, M. Markevitch, S. W. Randall, C. Jones, and D. Zaritsky, *Ap. J. Lett.* **648**, L109 (2006).
- [44] W. Dawson et al., *Musket Ball cluster composite image*, <http://chandra.harvard.edu/photo/2012/musketball/> (Accessed January 2014).
- [45] M. Bradac et al., *MACS J0025 cluster composite image*, <http://chandra.harvard.edu/photo/2008/macs/> (Accessed January 2014).
- [46] A. Mahdavi, H. Hoekstra, A. Babul, D. D. Balam, and P. L. Capak, *Ap. J.* **668**, 806 (2007).
- [47] Sloan Digital Sky Survey, *Distribution of local galaxies from the SDSS*, <http://www.sdss3.org/science/> (Accessed January 2014).
- [48] Planck Collaboration, *Planck CMB full sky map*, [http://www.esa.int/spaceinimages/Images/2013/03/Planck\\_CMB](http://www.esa.int/spaceinimages/Images/2013/03/Planck_CMB) (Accessed January 2014).
- [49] WMAP Collaboration, *WMAP CMB full sky map*, <http://map.gsfc.nasa.gov/media/121238/index.html> (Accessed January 2014).
- [50] G. Bertone, D. Hooper, and J. Silk, *Phys. Rep.* **405**, 279 (2005).
- [51] Submitted to *A & A Planck Collaboration XV* (2013).
- [52] M. Bridges, *Artistic evolution of the universe*, <http://www.maths.tcd.ie/~mbridges/news.html> (Accessed January 2014).
- [53] J. Beringer and others (Particle Data Group), *Phys. Rev. D* **86**, 010001 (2012).
- [54] F. Hoyle and R. J. Tayler, *Nature* **203**, 1108 (1964).
- [55] P. J. E. Peebles, *Phys. Rev. Lett.* **16**, 410 (1966).

- [56] R. V. Wagoner, W. A. Fowler, and F. Hoyle, *Ap. J.* **148**, 3 (1967).
- [57] K. Jedamzik and M. Pospelov, in *Particle Dark Matter: Observations, Models and Searches*, edited by G. Bertone (Cambridge University Press, Cambridge, UK, 2010), chap. 28, pp. 565–585.
- [58] M. Kowalski et al., *Ap. J.* **686**, 749 (2008).
- [59] K. A. Olive (2003), [arXiv:astro-ph/0301505v2](#).
- [60] P. Gondolo (2004), [arXiv:astro-ph/0403064v1](#).
- [61] J. H. Applegate, C. J. Hogan, and R. J. Scherrer, *Phys. Rev. D* **35**, 1151 (1987).
- [62] K. Olive (2003), [astro-ph/0301505](#).
- [63] B. E. Wood, H. Muller, G. P. Zank, and J. L. Linsky, *Ap. J.* **574**, 412 (2002).
- [64] C. Alcock et al. (2000), [arXiv:astro-ph/0011506v1](#).
- [65] P. Tisserand et al. (2011), [arXiv:astro-ph/0607207v2](#).
- [66] T. Nakamura, M. Sasaki, T. Tanaka, and K. S. Thorne, *Ap. J. Lett.* **487**, L139 (1997).
- [67] C. Alcock et al., *Ap. J.* **542**, 281 (2000).
- [68] Y. Fukuda and others (Super-Kamiokande Collaboration), *Phys. Rev. Lett.* **81**, 1562 (1998).
- [69] Q. R. Ahmad and others (SNO Collaboration), *Phys. Rev. Lett.* **89**, 011301 (2002).
- [70] V. Lobashev et al., *Nucl. Phys. A* **719**, 153c (2003).



- [71] K. Assamagan et al., Phys. Rev. D **53**, 6065 (1996).
- [72] V. N. Aseev et al., Phys. Rev. D **84**, 112003 (2011).
- [73] Eitel et al., Nucl. Phys. (Proc. Supp.) B **143**, 197 (2005).
- [74] L. Passalacqua et al., Nucl. Phys. Proc. Suppl. **55C**, 435 (1997).
- [75] D. Buskulic and others (ALEPH Collaboration), Phys. Lett. B **349**, 585 (1995).
- [76] MissMJ, *Standard model chart*, [http://en.wikipedia.org/wiki/File:Standard\\_Model\\_of\\_Elementary\\_Particles.svg](http://en.wikipedia.org/wiki/File:Standard_Model_of_Elementary_Particles.svg) (Accessed January 2014).
- [77] S. Dodelson and L. M. Widrow, Phys. Rev. Lett. **72**, 17 (1994).
- [78] P. B. Pal and L. Wolfenstein, Phys. Rev. D **25**, 766 (1982).
- [79] J. L. Feng, Annu. Rev. Astron. Astrophys. **48**, 495 (2010).
- [80] S. S. McGaugh, M. K. Barker, and W. J. G. de Blok (2002), [arXiv:astro-ph/0210641v1](#).
- [81] A. Kusenko, Phys. Rep. **481**, 1 (2009).
- [82] K. N. Abazajian (2009), [arXiv:0903.2040\[astro-ph.CO\]](#).
- [83] P. Di Bari, S. F. King, and A. Merle (2013), [arXiv:1303.6267v3\[hep-ph\]](#).
- [84] M. R. S. Hawkins (2011), [arXiv:1106.3875v1\[astro-ph.CO\]](#).
- [85] P. H. Frampton, M. Kawasaki, F. Takahashi, and T. T. Yanagida (2010), [arXiv:1001.2308v2\[hep-ph\]](#).
- [86] S. Hawking, Nature **248**, 30 (1974).

- [87] F. Capela, M. Pshirkov, and P. Tinyakov (2013), `arXiv:1301.4984v3[astro-ph.CO]`.
- [88] R. D. Peccei and H. R. Quinn, *Phys. Rev. Lett.* **38**, 1440 (1977).
- [89] F. Wilczek, *Phys. Rev. Lett.* **40**, 279 (1978).
- [90] S. Weinberg, *Phys. Rev. Lett.* **40**, 223 (1978).
- [91] G. G. Raffelt, *Lect. Notes Phys.* **741**, 51 (2008).
- [92] S. Moriyama et al., *Phys. Lett. B* **434**, 147 (1998).
- [93] Y. Inoue et al., *Phys. Lett. B* **536**, 18 (2002).
- [94] Y. Inoue et al., *Phys. Lett. B* **668**, 93 (2008).
- [95] K. Baker et al., *Ann. der Phys.* **6**, A93 (2013).
- [96] G. Carosi et al. (2013), `arXiv:1309.7035v1[hep-ph]`.
- [97] J. Redondo and A. Ringwald, *Contemp. Phys.* **52**, 211 (2011).
- [98] E. Armengaud et al. (2014), `arXiv:1401.3233v1[physics.ins-det]`.
- [99] H. Miyazawa, *Prog. Theor. Phys.* **36**, 1266 (1966).
- [100] J. L. Gervais and B. Sakita, *Nucl. Phys. B* **34**, 632 (1971).
- [101] J. Wess and B. Zumino, *Nucl. Phys. B* **70**, 39 (1974).
- [102] G. Gelmini and P. Gondolo, in *Particle Dark Matter: Observations, Models and Searches*, edited by G. Bertone (Cambridge University Press, Cambridge, UK, 2010), chap. 7, pp. 121–141.

- [103] G. Jungman, M. Kamionkowski, and K. Griest, Phys. Rep. **267**, 195 (1996).
- [104] R. L. Goldstone, M. E. Roberts, and T. M. Gureckis, Curr. Dir. Psy. Sci. **17**, 10 (2008).
- [105] H. Arrow, J. E. McGrath, and J. L. Berdahl, *Small groups as complex systems: Formation, coordination, development, and adaptation* (Sage, Newbury Park, CA, 2000).
- [106] X. L. Qi, T. L. Hughes, S. Raghu, and S. C. Zhang, Phys. Rev. Lett. **102**, 187001 (2009).
- [107] T. Grover, D. N. Sheng, and A. Vishwanath (2013), `arXiv:1301.7449v2[cond-mat.str-el]`.
- [108] M. S. Turner and F. Wilczek, Phys. Rev. D **42**, 1001 (1990).
- [109] J. Silk and S. Mark, Phys. Rev. Lett. **53**, 624 (1984).
- [110] P. Salati, F. Donato, and N. Fornengo, in *Particle Dark Matter: Observations, Models and Searches*, edited by G. Bertone (Cambridge University Press, Cambridge, UK, 2010), chap. 26, pp. 521–546.
- [111] R. J. Protheroe, Ap. J. **254**, 391 (1982).
- [112] O. Adriana and others (PAMELA Collaboration), Phys. Rev. Lett. **105**, 121101 (2010).
- [113] M. Ackermann and others (FermiLAT Collaboration), Phys. Rev. Lett. **108**, 011103 (2012).
- [114] M. Aguilar and others (AMS Collaboration), Phys. Rev. Lett. **110**, 141102 (2013).

- [115] J. D. Lewin and P. F. Smith, *Astropart. Phys.* **6**, 87 (1996).
- [116] D. G. Cerdeño and A. M. Green, in *Particle Dark Matter: Observations, Models and Searches*, edited by G. Bertone (Cambridge University Press, Cambridge, UK, 2010), chap. 17, pp. 347–369.
- [117] D. R. Tovey, R. J. Gaitskell, P. Gondolo, Y. Ramachers, and L. Roszkowski, *Phys. Lett. B* **488**, 17 (2000).
- [118] F. Donato, N. Fornengo, and S. Scopel, *Astropart. Phys.* **9**, 247 (1998).
- [119] Y. Ramachers, *Astropart. Phys.* **19**, 419 (2003).
- [120] D. S. Akerib and others (LUX Collaboration) (2013), [arXiv:1310.8214v1\[astro-ph.CO\]](#).
- [121] P. F. Smith and J. D. Lewin, *Phys. Rep.* **187**, 203 (1990).
- [122] R. Bernabei et al., *Eur. Phys. J. C* **56**, 333 (2008).
- [123] R. Bernabei et al., *Nucl. Instr. Meth. Phys. Res. A* **592**, 297 (2008).
- [124] R. Bernabei et al., *Eur. Phys. J. C* **67**, 39 (2010).
- [125] C. E. Aalseth and others (CoGeNT Collaboration), *Phys. Rev. Lett.* **101**, 251301 (2008).
- [126] C. E. Aalseth and others (CoGeNT Collaboration), *Phys. Rev. Lett.* **106**, 131301 (2011).
- [127] P. Adamson and others (MINOS Collaboration), *Phys. Rev. D* **87**, 032005 (2013).

- [128] G. Angloher and others (CRESST Collaboration), Eur. Phys. J. C **72**, 1971 (2012).
- [129] R. Angese and others (CDMS Collaboration), Phys. Rev. D **88**, 031104 (2013).
- [130] R. Agnese and others (CDMS Collaboration) (2013), [arXiv:1304.4279v1\[hep-ex\]](#).
- [131] Z. Ahmed and others (CDMS Collaboration), Science **327**, 1619 (2010).
- [132] E. Aprile and others (XENON100 Collaboration) (2013), [arXiv:1207.5988v2\[astro-ph.CO\]](#).
- [133] J. Lindhard and M. Scharff, Phys. Rev. **124**, 128 (1961).
- [134] J. Lindhard, V. Nielsen, M. Scharff, and P. V. Thomsen, Dan. Vidensk. Selsk. Mat. Fys. Medd. **33**, 10 (1963).
- [135] J. Lindhard, M. Scharff, and H. E. Schiott, Dan. Vidensk. Selsk. Mat. Fys. Medd. **33**, 14 (1963).
- [136] K. S. Singwi and A. Sjölander, Phys. Rev. **120**, 1093 (1960).
- [137] A. Hitachi, Astropart. Phys. **24**, 247 (2005).
- [138] T. Shutt et al., Nuc. Instrum. Meth. Phys. Res. A **579**, 451 (2007).
- [139] P. Sorensen and C. E. Dahl, Phys. Rev. D **83**, 063501 (2011).
- [140] A. Manzur et al., Phys. Rev. C **81**, 025808 (2010).
- [141] P. Sorensen, J. Cosmol. Astropart. Phys. **09**, 033 (2010).
- [142] E. Aprile et al., Phys. Rev. C **79**, 045807 (2009).

- [143] K. Abe et al. (2013), [arXiv:1301.2815v1](#).
- [144] D. M. Mei, Z. B. Yin, L. C. Stonehill, and A. Hime, *Astropart. Phys.* **30**, 12 (2008).
- [145] Vishay Dale, *Metal oxide resistor data sheet*, <http://www.alliedelec.com/images/products/datasheets/bm/DALE/70201546.pdf> (Accessed January 2014).
- [146] TWP Inc., *T316 SS high transparency wire mesh data sheet*, [http://www.twpinc.com/wire-mesh/TWPCAT\\_12/p\\_050X050T0012W48](http://www.twpinc.com/wire-mesh/TWPCAT_12/p_050X050T0012W48) (Accessed January 2014).
- [147] Hamamatsu Photonics K. K., *Photomultiplier tubes: Basics and applications*, [http://psec.uchicago.edu/links/pmt\\_handbook\\_complete.pdf](http://psec.uchicago.edu/links/pmt_handbook_complete.pdf) (Accessed January 2014).
- [148] K. H. Beckurts and K. Wirtz, *Neutron Physics* (Springer-Verlag, Berlin, 1964).
- [149] C. L. Lee and X. L. Zhou, *Nuc. Instrum. Meth. B* **152**, 1 (1999).
- [150] S. Agostinelli et al., *Nuc. Instrum. Meth. A* **506**, 250 (2003).
- [151] J. Allison et al., *IEEE Trans. Nuc. Sci.* **53**, 270 (2006).
- [152] R. Veenhof, *Garfield simulation toolkit*, <http://garfield.web.cern.ch/garfield> (Accessed October 2013).
- [153] S. Biagi, *Magboltz simulation toolkit*, <http://magboltz.web.cern.ch/magboltz> (Accessed October 2013).
- [154] I. Smirnov, *Heed simulation toolkit*, <http://heed.web.cern.ch/heed> (Accessed October 2013).

- [155] COMSOL Inc., *COMSOL Multiphysics*, <http://www.comsol.com/comsol-multiphysics> (Accessed July 2013).
- [156] National Institute of Standards and Technology, *PSTAR Database*, <http://physics.nist.gov/PhysRefData/Star/Text/PSTAR.html> (Accessed July 2013).
- [157] C. M. B. Monteiro et al., J. Inst. **2**, P05001 (2007).
- [158] V. Álvarez and others (NEXT Collaboration), J. Inst. **8**, P04002 (2013).
- [159] C. E. Dahl, Ph.D. thesis, Princeton University (2009).
- [160] V. Álvarez and others (NEXT Collaboration), J. Inst. **7**, T06001 (2012).
- [161] T. M. Stiegler, Ph.D. thesis, Texas A&M University (2013).